2019

The use of Fluid Haemodynamics in the Diagnosis of Cardiovascular Disease

Andrew Malone
Technological University Dublin

The use of fluid haemodynamics in the diagnosis of cardiovascular disease

Andrew Malone
M.Sc. B.Sc.

A thesis submitted to Technological University Dublin for the degree of Doctor of Philosophy

School of Physics & Clinical & Optometric Sciences

Technological University Dublin

Kevin Street, Dublin 8, Ireland

Supervisors: Prof. Jacinta E Browne, Dr. Seán Cournane, Prof. Izabela Naydenova, Prof. Andrew J Fagan

October 2019

Abstract

Currently the diagnostic methods used to detect cardiovascular disease largely rely on the inference of the presence of arterial stenosis. There is a clinical interest in the development of a diagnostic screening technique which can indicate the risk of developing cardiovascular disease at an early stage so that non-surgical treatments can be applied.

The goal of this work was to develop and validate a diagnostic screening technique for cardiovascular disease using the mechanical biomarker wall shear stress. Improvements in wall shear stress measurements were made by using a 2D Fourier transform to extract additional spectral information from the ultrasound pulse and decrease the spectral variance by integrating across the bandwidth of transmitted frequencies. This technique was validated for a series of anatomically realistic flow phantoms which precisely mimicked the progression of wall stiffening that characterises cardiovascular disease.

The newly developed spectral analysis technique demonstrated a higher diagnostic performance than the other techniques tested, both in terms of a greater degree of significance in detecting differences in vessel wall stiffness and in terms of the sensitivity and specificity of the technique. The technique could not be tested in pulsatile flow due to hardware limitations, but preliminary testing indicated that the increased performance of the technique would likely transfer to a physiological flow regime.

The results of this work indicated that the algorithm had the potential to rival the diagnostic power of the current gold standard while being applicable at an earlier stage of cardiovascular disease.

I certify that this thesis which I now submit for examination for the award of Doctor of Philosophy, is entirely my own work and has not been taken from the work of others, save and to the extent that such work has been cited and acknowledged within the text of my work. This thesis was prepared according to the regulations for graduate study by research of the Technological University Dublin and has not been submitted in whole or in part for another award in any other third level institution. The work reported on in this thesis conforms to the principles and requirements of the TU Dublin's guidelines for ethics in research. TU Dublin has permission to keep, lend or copy this thesis in whole or in part, on condition that any such use of the material of the thesis be duly acknowledged.

Signature _____ Date _____

Andrew Malone

Acknowledgments

First and foremost, I would like to extend my sincere gratitude to my supervisors: Dr. Seán Cournane, Prof. Izabela Naydenova, Prof. Andrew Fagan, and especially Prof. Jacinta Browne for their support, patience, kindness, and encouragement throughout my project. The wealth of knowledge you have to share has made me a stronger, more capable researcher and I owe you each a tremendous debt of gratitude for helping me get this far.

A Fiosraigh Dean of Graduate Students Scholarship from TU Dublin is gratefully acknowledged. Additional funding support from the Irish Association of Physicists (IAPM) in Medicine in the form of the Young Investigator grant is also appreciated.

I have had the privilege of working with some amazing people throughout this project. I would like to acknowledge support and access to the Aixplorer ultrasound scanner from Dr. James Meaney and the staff at the Centre for Advanced Medical Imaging (CAMI) at St. James' Hospital. I would also like to thank Mr. Neil Branigan at TU Dublin for his technical support and access to the Lloyd instruments material tester. And I would like to thank the staff and my colleagues at FOCAS who provided help and guidance at every turn.

To my colleagues, Dr. Andrea Doyle, Dr. Aoife Ivory, and Dr. Silvin Knight, thank you for your help and for our mutual commiserations. I wish you all every success in your careers.

To my parents, Eileen and Declan, there is not enough space to fully express how grateful I am to you. Without your support, your care, and your words of encouragement I never would have made it this far. Thank you for inspiring me and teaching me, thank you for instilling in me from a young age a love of science. To my brothers, Peter and Shane, thank you for the laughs, the drinks, and the good times and good company. You were

always there for a spirited discussion or a funny story and you always managed to put a smile on my face.

Lastly, I would like to thank my partner, Sarah, without whom I would be completely lost. We have been through so much together in such a short time and you inspire me every single day. I would not be writing this right now if not for you, you were the cheerleader I needed to get this project over the line.

List of abbreviations

AIUM	American Institute of Ultrasound in Medicine
ANOVA	Analysis of variance
BMF	Blood mimicking fluid
CTA	Computed tomography angiography
CVD	Cardiovascular disease
DAC	Digital-to-analogue converter
DR	Dynamic Range
DDR	Doppler dynamic range
DSA	Digital subtraction angiography
FWHM	Full width at half maximum
GSB	Geometric spectral broadening
HDPE	High density polyethylene
IEC	International electrotechnical commission
IPEM	Institute of Physics and Engineering in Medicine
IQ	In-phase quadrature
ISB	Intrinsic spectral broadening
ISO	International organisation for standardisation
LMA	Low melting alloy
MFUDSA	Multifrequency *UltraFast* Doppler spectral analysis
MI	Mechanical index
MRA	Magnetic resonance angiography
PC-MRI	Phase contrast magnetic resonance imaging
PIV	Particle image velocimetry

PRF	Pulse repetition frequency
PVA	Polyvinyl alcohol
PVA-c	Polyvinyl alcohol cryogel
PW	Pulsed wave
SAM	Scanning acoustic macroscope
SA:V	Surface area to volume ratio
SNR	Signal-to-Noise ratio
TI	Thermal index
TMM	Tissue mimicking material
TTB	Transit time broadening
µPIV	Micro particle image velocimetry
VMM	Vessel mimicking material
WSS	Wall shear stress

Table of Figures

control the degree of stenosis in the LMA inverse mould. (b) Rapid prototyped model of the renal artery based on CT data from a healthy volunteer. This model was not altered from the CT data. (c) LMA inverse mould produced using the silicone master mould. This model did not feature a stenosis.

- Figure 4.2: (a) Rapid prototyped model of renal artery from CT data of a healthy volunteer. (b) Silicone master mould produced using renal artery model. (c) Low melting alloy inverse mould of renal artery produced from silicone master mould. (d) Vessel mould with inverse mould in place. The vessel mould has an internal diameter 3mm greater than the inverse mould, giving a vessel wall thickness of 1.5 mm.
- Figure 4.3: Lumen moulds made of low melting alloy. The vessel mimicking material was moulded around these inserts to produce an anatomically realistic vessel lumen. The low melting alloy could be removed later by placing the phantom in a water bath at 60°C.
- Figure 4.4: The apparatus of the scanning acoustic macroscope (SAM) system. A glass plate is submerged in a tank of deionised water which reflects the ultrasound pulse. By comparing the returning signals when passing through a material sample with a reference signal, acoustic properties can be measured.
- Figure 4.5: An example B-mode image (left) of the phantom lumen and the line profile (right) extracted from it. The diameter of the vessel was calculated by multiplying the number of pixels across the lumen with the pixel spacing of the ultrasound scanner.
- Figure 4.6: The effect of increasing freeze thaw cycles on speed of sound measurements for PVA-c. The error bars correspond to one standard deviation. The dashed black line indicates the in vivo value for arterial speed of sound [4].

- Figure 5.6: A comparison between 8 Doppler spectra computed using (a) 1D Fourier analysis with no additional processing, (b) 1D Fourier analysis incorporating Welch's method, and (c) 2D Fourier analysis incorporating multifrequency Doppler – adapted from Loupas & Gill [7].
- Figure 5.7: A block diagram of the steps in the MFUDSA algorithm. The diagram is colour coded to correspond to the different stages in the cycle: blue items are processing operations taken on the data in the time domain; green items are processing steps taken in the frequency domain; yellow items are signal filtering; and purple corresponds to the output information sent to the user.
- Figure 5.8: A representation of the combined IQ data form exported from the scanner in the form cos(S) + i*sin(S) where S is the original received signal and i is the imaginary number. This data was then analysed using in-house developed MATLAB code.
- Figure 5.9: The segmentation process for the IQ data matrix. Considerable memory savings were made by discarding irrelevant data corresponding to areas of the imaging region outside the vessel lumen. This sectioning was also used to extract individual "pulse lines" for processing.
- Figure 5.10: An example of a simple time domain windowing process. This procedure truncates the signal and reduces the effect of sidelobe artefacts in the frequency space.
- Figure 5.11: A typical Doppler spectrum produced by a 2D discrete Fourier transform after low pass filtering was used to remove the PRF.
- Figure 5.12: Validation steps of the MFUDSA algorithm
- Figure 5.13: MFUDSA algorithm SNR with respect to transmit frequency
- Figure 5.14: The windows used in this analysis

- Figure 6.7: Example WSS curve using an UltraFast velocity map in diagnostic imaging mode
- Figure 6.8: Example WSS curve using an MFUDSA velocity map in research imaging mode
- Figure 6.9: Boxplots of WSS values for a range of vessel stiffnesses in the steady flow regime grouped by estimation technique.
- Figure 6.10: Boxplots of WSS values for a range of vessel stiffnesses in the pulsatile flow regime grouped by estimation technique.

Table of Tables

Contents

Chapter 1: Introduction

1.1. Context and Motivation

Cardiovascular disease (CVD) is currently the leading cause of preventable death in the world, accounting for 31% of deaths globally [10,11]. Despite this, CVD prevalence can be reduced by addressing behavioural risk factors that aggravate the disease such as tobacco use, unhealthy diet and obesity, physical inactivity, and excessive alcohol consumption [11]. However, the diagnosis of CVDs is largely based on detecting or inferring the presence of indicators associated with late stage CVD such as the formation of atherosclerotic plaque in the arteries. Given that CVD is currently only diagnosed in this manner, this can limit the treatment options for patients to surgical options which carry an inherent risk for the patient. There exists, therefore, a clinical interest in developing a non-invasive diagnostic screening technique which can be applied early in the progression of CVD so that patients can be treated pharmacologically or through a change in lifestyle.

An early part of the development of CVD manifests as damage to the endothelium resulting in an increase in vessel stiffness [12]. An indicator of this damage is the mechanical biomarker wall shear stress (WSS) which is defined as the product of the dynamic viscosity and the gradient of the blood velocity flow profile evaluated as close to the vessel wall as possible. The link between WSS and vessel stiffness can be understood in the form of elasticity of vessel walls acting as a damping force of the blood velocity, with decreased elasticity resulting in less friction on the outermost blood fraction. As blood can be thought of as a series of concentric annuli each imposing a frictional force on one another, a decrease in vessel elasticity will lead to a decrease in frictional damping on the outermost blood fraction, which in turn will lead to a flattening

on the blood velocity flow profile, which will manifest as a decrease in measured wall shear stress. There are a number of techniques which can be utilised for the precise measurement of the blood velocity profile required for calculation of WSS, such as phase contrast MRI, particle image velocimetry, and Doppler ultrasound [13]. Each technique has certain advantages and disadvantages, but ultrasound represents a strong diagnostic basis for the evaluation of WSS due to its low cost, fast scan times, and high degree of velocity precision. There are three considerations which need to be taken into account when making a WSS measurement, which include the signal-to-noise ratio (SNR), the velocity resolution, and the temporal resolution [13]. These values can each significantly affect the accuracy of a WSS measurement because it depends so highly on the precise measurement of blood velocities close to the vessel wall which are typically both very slow moving and exhibit a weak Doppler signal.

Commented [AM1]: Added based on Kumar's comment

Modern techniques have been developed which can provide a significant improvement to the temporal resolution such as *UltraFast* Doppler ultrasound, a technique available on the Aixplorer scanner (Supersonic Imagine, France). This work aims to combine the high temporal resolution of the *UltraFast* imaging mode with custom post-processing code to decrease the spectral variance and achieve an increase in the SNR and velocity. This novel method of constructing velocity data builds on a theoretical framework first proposed by Loupas & Gill [7] to develop a multifrequency *UltraFast* Doppler spectral analysis (MFUDSA) algorithm for use in quantification of WSS for the early diagnosis of CVD.

1.2. Aims and Objectives

The aim of this work was to design an algorithm that utilised raw *UltraFast* Doppler in-phase quadrature (IQ) data acquired using an Aixplorer scanner, the accuracy of which

would be investigated by scanning a series of anatomically realistic flow phantoms constructed to mimic different stages in the progression of CVD.

The main objectives and goals of this thesis are summarised below:

1. Characterisation of the system and measurement protocol, which involved the following:
    a. Measurement of the transmission characteristics of the Aixplorer system
    b. Measurement of the display capabilities and inaccuracies in the system, including a quantification and cancellation of the intrinsic spectral broadening and measurement of the dynamic range
    c. Determining the best protocol for transducer alignment
2. Production of a novel phantom testbed which was capable of precisely mimicking different stages of CVD, which included:
    a. Manufacturing of:
        i. A vessel mimicking material with a variable stiffness and the mechanical characterisation thereof, producing a novel mimic of the progression of arterial disease
        ii. A tissue mimicking material for the surrounding material of the phantom
        iii. A blood mimicking fluid for the flow system
    b. Verification of the geometric accuracy of the vessels produced as compared to the renal artery model they are based on
    c. The acoustic characterisation of the constituent phantom materials
    d. Deploying of custom LabVIEW (National Instruments, USA) code to drive the flow system
3. Development of the novel MFUDSA algorithm, including:

a. Writing of custom code to perform the required 2D Fourier analysis and frequency integration
b. Generation of simulated data for validation and optimisation of the code
c. Writing of custom code to use velocity data in the formation of a sonogram
d. Extraction and importation of raw IQ data from the Aixplorer system for use in the MFUDSA algorithm

4. Comprehensive flow experimentation, which involved:
    a. Determining the required inlet length for the pump network to minimise turbulence in flow
    b. Data collection and analysis with a variety of WSS estimation techniques, including the novel MFUDSA algorithm
    c. Analysis of the effectiveness of the examined techniques at diagnosing CVD based on WSS values using a novel, anatomically realistic phantom testbed representing the different stages of arterial disease through variable vessel stiffness matching values reported *in vivo* for patients diagnosed with CVD.

1.3. Thesis Overview

The thesis is divided into seven main chapters, detailing the development and optimisation of the MFUDSA algorithm as well as the production and characterisation steps taken to ensure the reliable and reproducible standard of the results.

Chapter 2: Theory and Background

The background literature required for all subsequent chapters is provided in Chapter 2 in addition to a review of the current diagnostic methods used for assessing CVD. The chapter begins with an outline of the current diagnostic approaches in the diagnosis of

CVD, which is followed by a review of the methods which can be used to calculate WSS. A review of methods to produce an anatomically realistic arterial flow phantom follows including discussion of the vessel mimicking material polyvinyl alcohol cryogel (PVA-c). PVA-c provides a useful material for vessel construction as it has a precisely tuneable Young's modulus value which can be used to mimic the different stages of progression of atherosclerosis. The chapter concludes with a discussion of the mechanical properties of tissue and a review of the literature to determine the vessel wall stiffness values associated with the progression of CVD.

Chapter 3: Ultrasound scanning system Calibration

The system used for the majority of this work was the Aixplorer (Version 11.2, Supersonic Imagine, France) ultrasound scanner. This chapter begins with a discussion of the effects of ultrasound on tissue *in vivo* and the importance of ensuring the ultrasound system remains within the safety limits. The pulse parameters of the Aixplorer were measured, including the central transmission frequency, the frequency bandwidth of the pulse, and the acoustic pressure of the pulse. The chapter also includes the measurement of the Doppler dynamic range of the transducer used in this work, a quantity which is underreported in the literature, and the measurement of the intrinsic spectral broadening. The chapter also analyses a new method of intrinsic spectral broadening cancellation which is only possible when using *UltraFast* imaging modes. Finally, the chapter outlines and tests a protocol for the positioning of the transducer prior to acquiring velocity data to ensure the highest rate of reproducibility in results.

Chapter 4: Phantom production

This chapter provides a methodology for the entirety of the production process of the novel arterial flow phantoms. The chapter first discusses the PVA-c vessel mimicking material and how it has been used in previous studies throughout the literature as well as

its typically reported mechanical properties. A point is made that mechanical characterisation may not be reliable when using test objects with sufficiently different area to volume ratios (SA:Vs). The protocol is included for the production of the vessel mimicking material, the tissue mimicking material, and the blood mimicking fluid are outlined as well as the geometric fabrication of the moulds used to create the anatomically realistic vessels. The chapter then discusses characterisation of the constituent phantom materials and measuring the accuracy of the geometric production of the vessels as compared to the renal artery model they are based on.

Chapter 5: Development of the multifrequency UltraFast Doppler spectral analysis (MFUDSA) algorithm

This chapter outlines the procedure used to produce the custom code for the novel MFUDSA algorithm. The chapter begins with a discussion of 2D Fourier analysis and methods which have been used previously to improve the Doppler signal. The methodology outlines the procedure of extracting data and applying the algorithm to the data in order to output a velocity spectrum. Detail is given on how the algorithm achieves each step in the process. The next section details the procedure for generating simulated data and the measurement parameters for the experimental data. An outline of the methods used for optimisation of the algorithm is presented, describing the effect of changing the pulse transmission parameters and using time domain windowing functions to reduce the influence of sidelobes in the frequency space. Finally, a procedure for the generation of a Doppler sonogram is outlined using custom code which can interface with the MFUDSA algorithm.

Chapter 6: Comprehensive flow experimentation

Chapter 6 begins with a discussion of the phantoms used in the flow experiments, particularly the stiffness of the vessels used, and the details of the pump network including the optimum inlet length. The next section outlines the experimental data collected and

the WSS estimation methods used on the data. The details of the analysis follow, including discussion of the sensitivity and specificity of the techniques in addition to the analysis of significance of results. The chapter also includes a number of example images produced of the velocity flow profiles and the WSS along the length of the vessel using different techniques.

Chapter 7: Conclusions

Finally, Chapter 7 outlines the most important conclusions of the research as well as recommendations for future research and potential commercial development and how the technique might be improved.

Chapter 2: Theory and Background

2.1. Introduction

The purpose of this chapter is to provide a detailed synopsis of the theoretical underpinnings of the experimental procedures utilised as part of this Ph.D. study and described in the subsequent chapters. Furthermore, the justification, motivation and context of this research will be put in context of the current relevant research landscape.

Cardiovascular disease (CVD) is among the leading cause of deaths in the world [14] and is additionally associated with an increased risk a number of conditions such as heart failure, hypertension, diabetes mellitus and cerebrovascular disease [15].

2.1.1. Current diagnostic approach

A number of different approaches have been used to diagnose CVD and these methods are typically utilised after acquiring a detailed clinical history of the patient and their family [16].

Digital subtraction angiography (DSA) was the gold standard for assessment of vascular health until recently however discussions in the literature have suggested it should be relegated to a secondary diagnostic approach due to its invasive nature and risk of complications compared to other techniques, to be replaced with the new primary diagnostic approach of duplex ultrasound [17]. It is currently primarily used in assessment of below-the-knee arterial disease or in situations where other diagnostic approaches disagree [16], this is due to the higher sensitivity of 94% to 100% and specificity of 65% to 97% compared to similar techniques [18,19].

Computed tomography angiography (CTA) has the advantage of short examination times, which lead to reduced motion artefacts while also providing high resolution, 3D

visualisation, and being a widely available technique. However, the drawbacks of CTA include: a lack of haemodynamic data, radiation exposure to the patient, and the use of iodinated contrast agents which can cause nephrotoxicity in renal-compromised patients [16]. Some studies have been carried out into the reduction of contrast agent based nephrotoxicity but further research is required [20,21].

Magnetic resonance angiography (MRA) can be utilised as a contrast based angiography technique (using gadolinium) or as a non-contrast technique using phase contrast or time-of-flight techniques [16,22]. Using the non-contrast techniques results in reduced resolution and an increased susceptibility to artefacts which limits their use on a wide scale. However, the non-contrast techniques are particularly useful in patients with mild to moderate chronic renal disease as they eliminate the risk of nephrotoxicity from the contrast agent. MRA has superior soft tissue resolution over CTA but it has a longer scan time, resulting in motion artefacts. MRA also has a greater number of contraindications such as pacemakers and other implants which are not categorised as MR safe [16]. An additional consideration of MRA is that the relatively small bore of the scanner can be a limit to patient comfort in cases of claustrophobia [16].

Duplex ultrasound is currently considered the first step in any diagnostic review of the vascular system due to its wide availability and low cost [16]. The use of pulsed wave (PW) Doppler ultrasound in particular is considered the gold standard technique in the detection of arterial stenosis as the increase in peak systolic velocity in the presence of arterial obstruction is easily detectable while being both non-ionising and non-invasive [16].

These techniques, by and large, depend on the detection of obstructions in the vasculature. The diagnostic value that they provide is predominantly, therefore, for later stage CVD.

The treatment options available for late stage CVD are mostly surgical, and all carry inherent risk [16]. Therefore, there exists a need for a new diagnostic method which can be utilised to detect an earlier stage of CVD or even the initiation of it by measuring the morphological effects of early stage disease. One potential biomarker of these effects is wall shear stress which has been linked to arterial wall stiffening and the formation of atherosclerotic plaques [15,23].

2.2. Wall shear stress

Wall shear stress (WSS) is defined as the tangential force per unit area that is exerted by the flowing blood on the surface of the endothelium and vice versa. This can be expressed mathematically as follows:

$$WSS = -\mu \frac{\delta V}{\delta r}|_{r=R} \tag{2.1}$$

where μ is the dynamic viscosity of blood $\delta V/\delta r$ is the velocity flow profile, sometimes referred to as the wall shear rate, and R is the vessel radius. WSS has been linked to CVD for many years, with several major studies having examined its role in atherogenesis. WSS has been shown to be particularly useful in the assessment of vascular reactivity [24], wall thickening [25], and atherosclerosis [26,27]. In the 1970s, it was theorised that a high WSS would cause damage to the endothelium resulting in the formation of atherosclerotic lesions, however Caro et al. [28] proposed that *in vivo* results indicated that low WSS values coincided with areas of increased lesion formation. This was later confirmed experimentally in the 1980s and early 1990s through a number of studies, also, demonstrating that the measurement of WSS was of critical importance in the early diagnosis of renal artery stenosis [29–32]. Malek et al. [27] provides a detailed analysis of the historical evolution of the role of WSS in understanding atherosclerosis. In addition, Malek et al. states a range of WSS values typically exhibited *in vivo*, with values

Commented [AM2]: Removed abbreviation

of 1 – 7 Pa being characterised as low risk and values in the range -0.4 – 0.4 Pa characterised as at risk of developing CVD. Chatzizisis et al. [33] reported similar values of WSS for regions at risk of developing atherosclerosis to Malek et al., with WSS values above 3 Pa considered to be high and WSS ≤ 1 Pa considered to be low and at risk.

Commented [AM3]: Added based on Dervil's comment

Palombo et al. [12] outlines a relationship between WSS and arterial stiffness and its role in atherogenesis. While Palombo et al. does note that the co-localisation of increased arterial stiffness and atherosclerosis may be incidental, they state that the process of arterial stiffening is typically characterised by the alteration of the extracellular matrix that can lead to pathophysiologic processes which increase the likelihood of lipid accumulation at the onset of atherosclerosis [12]. Wentzel et al. [34] describe the role of WSS in the development of atherosclerosis as the low and oscillatory WSS values suppression of the atheroprotective gene which prevents inflammation and lipid accumulation leads to development of CVD.

There have been a number of methods utilised in the assessment of WSS, the most predominant of which will be outlined here.

2.2.1. Phase contrast MRI

One methodology which is utilised frequently for the assessment of wall shear stress is phase contrast magnetic resonance imaging (PC-MRI). PC-MRI is based on the relative phase shift of spins moving along the vessel. By applying a gradient field along the vessel, a spatially dependent phase shift in the spins is set up, the region is then imaged a short time later and a quantitative blood velocity flow profile can be determined as blood velocity will be linearly proportional to its phase shift.

Shaaban et al. [35] outlined a comprehensive review of PC-MRI. Due to the nature of MR imaging, the voxels imaged contain an average value of velocity from all tissue

contributions, both moving and stationary. This leads to a large source of error in this methodology where the position of the vessel wall in the edge voxel is not known due to limited spatial resolution. Osinnski et al. [36] showed that this partial volume error can lead to a 34 % underestimation of WSS. Reneman et al. [37] suggested that this limitation prevents measurement of blood velocities closer than 1000-1200 μm to the vessel wall. Additionally there is a source of error associated with the limited temporal resolution of MR imaging, Katritsis et al. [13] has stated that the long scan times of 25-30 seconds of MRI result in a number of inaccuracies due to motion of the patient and as a result, special precautions must be taken when examining blood flow during dynamic processes.

Potters et al. [38] proposed that 3D cine PC-MRI represented the best methodology for the evaluation of wall shear stress as it is the only technique which allows for non-invasive measurement of 3D blood velocity gradients. In this study, a technique was developed which allows the researchers to calculate volumetric WSS which they claim provides a better clinical biomarker as it can be used to evaluate local variations along the entirety of the vessel wall. However, this increased WSS resolution comes at the expense of the need for additional velocity measurements and the researchers were forced to use natural neighbour interpolation combined with a smoothing spline fit at each point on the vessel wall. This technique was validated on in simulation studies before being applied to PC-MRI data from six healthy volunteers.

A recent study undertaken by Peng et al. [39] evaluated WSS in hypertensive rats using PC-MRI. In this study, a population of 7 hypertensive rats were studied using a 7T animal MRI scanner. This study attempted to determine differences in WSS values between two models of rats, spontaneous hypertensive rats and Wistar Kyoto rats. In the process of undertaking this study, it was found that limitations in spatial resolution posed large problems for PC-MRI and there was difficulty in maintaining the level of precision

required for completely accurate readings, leading to “unavoidable” underestimation of WSS. In order to try and improve the flow measurements, efforts were made to increase the spatial resolution (to 0.16 mm), however the corresponding decrease in signal-to-noise ratio (SNR) required the researchers to acquire more signal averages, lengthening the scan time.

2.2.2. Particle image velocimetry

Another method which is used to measure WSS is particle image velocimetry (PIV), this technique is based on the rapid capture of two sequential digital images; the images are acquired using a digital camera. Flow measurements are inferred due to the motion of tracer particles between the images, the relative motion of which are computed using cross-correlation techniques. The particles are typically fluorescent and are illuminated by a thin, two-dimensional plane of well defined, laser light. This method is limited *in vivo* as it is an optical technique and, as such, it has limited penetration depth; this makes it unsuitable for flow measurements outside of transparent media, therefore it cannot be used for arterial analysis although it can provide insight into WSS variation in different flow conditions.

In one study, carried out by Hochareon et al. [40], PIV was utilised to determine wall shear rates in a 50cc artificial heart made of Plexiglas . The images were analysed with a multigrid cross-correlation scheme which was developed as part of the study. The work shows that PIV can be utilised for rapid accurate determination of wall shear rates and it has the additional flexibility to be utilised on a variety of surface geometries. However, the author notes that a more accurate shear rate assessment would require higher magnification and the utilisation of specialised techniques.

In another study, carried out by Natarajan et al. [41], PIV was used in order to examine the effect that an arterial stent would have on blood flow using numerical simulations, with a particular emphasis on fluid shear rate contours and wall shear stress maps. The numerical methods were then compared to experimental results determined from PIV analysis. This study utilised three examples of corrugated vessels; a sharp stented vessel, a smooth stented vessel, and a non-stented vessel. The sharp stented vessel is designed to approximate the vessel immediately after the introduction of the stent and is referred to as the "worst-case geometry". The smooth stented vessel, by contrast, is a representation of the stent after time has passed, smoothing the edges and leading to the stent becoming endothelialised. The non-stented vessel acts as a control. Flow was visualised using neutrally buoyant crystalline particles with a diameter of 150 ± 100μm. The primary results of this study showed that wall shear stress values can be increased by as much as a factor of three due to the introduction of arterial stents.

When it comes to application of PIV *in vivo*, additional factors need to be taken into account, for example, the tracer particle size is limited to the scale of the vessel which needs to be studied. Vennemann et al. [42] provides insight into this area by examining the blood flow in the beating heart of a chicken embryo. This study proposes the use of micro particle image velocimetry (μPIV) for this application as it is capable of measuring instantaneous flow fields at sub-millimetre scales in regions of highly unsteady flow. Measurements were made at nine discrete points in the cardiac cycle, with a separation of 50 ms and each measurement consisting of up to 50 images pairs which were analysed using ensemble correlation techniques. The results of this study show that μPIV is capable of accurate, rapid visualisation of the flow velocity distribution in a beating embryonic avian heart. Additionally, the author outlines the advantages of nanoscale fluorescent tracer particles, whose small dimensions allows for light emitted by the particles to be

separated from the light scattered by tissue and erythrocytes. The smaller particle size also allows for a greater number of particles, giving µPIV a higher information density for the correlation, leading to an overall greater resolution in the velocity flow distributions. Finally, the small liposomes or particles (200-400 nm) are more readily able to penetrate the cell-depleted layer near the vessel wall and more closely follow the flow of plasma close to the vessel wall itself. This allows for a more accurate determination of the velocity gradient close to the vessel wall and, consequentially, yields a more accurate value for wall shear stress. Despite the significance of these results, the clinical feasibility of this technique for humans is not addressed in this study.

In a study undertaken by Anastasiou et al. [43], µPIV is utilised for the examination of blood like fluid flow in a microchannel resembling a bifurcated small artery. By examining the flow profiles of both Newtonian and non-Newtonian fluids, the study demonstrates that the assumption that blood behaves as a Newtonian fluid is not valid for small vessels (600µm in this case), while this is not surprising for vessels where the vessel diameter is similar in size to red blood cells (6 µm), this is not expected to be a reliable assumption for arterial flow. In addition, the study demonstrated that in bifurcations, the outer wall, experiencing a lower WSS than the inner wall, is more prone to development of atherosclerotic plaques.

Although particle imaging velocimetry provides good results, it is limited by its poor penetration depth. Phase contrast MRI itself is capable of generating excellent anatomical detail, however it suffers from poor spatial resolution for velocity quantification and extremely poor temporal resolution. Due to the extremely long scan times, this technique could not accurately measure WSS throughout the cardiac cycle in real time, making it less attractive than other techniques.

2.2.3. Doppler Ultrasound

While PW Doppler ultrasound can be used to measure WSS directly, there are a number of key limitations to the assessment of WSS via PW Doppler ultrasound, each of which is related to the difficulty in resolving the precise velocity measurements required for its analysis. Firstly, due to the relatively weak backscatter intensity of red blood cells combined with the lower concentration of red blood cells near the vessel wall, the resulting Doppler signal recorded close to the vessel wall will be proportionally weaker than the Doppler signal recorded from the centre of the vessel. This represents a significant problem as WSS measurement requires the blood velocity flow profile to be evaluated as close to the vessel wall as possible. The second limitation for WSS measurements is that of temporal resolution. When using spectral Doppler for WSS analysis, there is a limit to the number of velocity measurements which can be acquired at a certain time point. A single range gate or, in the case of multigate systems, range gates of sufficiently small gate size, must be placed at radial positions in the vessel [3,5]. The number of positions that can be covered is limited and, for small gate sizes, there is no way to quantify the entire velocity flow profile within a single cardiac cycle. Multigate systems can measure an entire profile across a vessel but only at a single longitudinal position, necessitating additional measurements to quantify the WSS at different positions in the vessel. This means that when calculating WSS, the velocity flow profile will be assembled from a number of triggered acquisitions taken from the same time point in different cardiac cycles. While this may not be a problem for phantom measurements, it could potentially cause an increase in errors when measuring *in vivo* due to respiratory motion resulting in the position of the vessel shifting between acquisitions. The final limitation to be aware of for WSS measurements relates to the velocity resolution of the system. Due to the relatively slow-moving blood velocities close to the vessel wall, the

Commented [AM4]: Added based on Kumars comemnt

changes in velocity at the vessel wall as a result of the wall stiffness variation would be small. This means that the system used would ideally have a high level of resolution for low velocity variations.

A possible alternative approach to reduce the effects of these limitations is to eschew measuring velocities close to the vessel wall and, instead, analyse velocities measured at the centre of the vessel lumen. An estimation of the WSS can still be calculated with these measurements and using an alternative approach.

One potential alternative WSS assessment method was illustrated by Katritsis et al. [13] based on Poiseuille's law. Starting with Poiseuille's law for volumetric flow rate (Q):

$$Q = \frac{\pi R^4 (p_1 - p_2)}{8\mu L} \tag{2.2}$$

where R is the lumen radius, p_1 and p_2 are the pressure values at the beginning and end of a vessel segment of length L, and μ is the dynamic viscosity. Poiseuille defines WSS in this regime as:

$$WSS = \frac{R(p_1 - p_2)}{2L} \tag{2.3}$$

By combining these equations, an equation expressing WSS in terms of volumetric flow rate is achieved:

$$WSS = \frac{4\mu Q}{\pi R^3} \tag{2.4}$$

The volumetric flow rate can be taken as the product of the average flow velocity and the cross-sectional area of the vessel and, for fully developed and parabolic flow, the average velocity is equal to half the maximum velocity.

This allows the computation of the WSS using the equation [13]:

$$WSS = \frac{2\mu V_{max}}{R} \tag{2.5}$$

Where: V_{max} was the peak velocity recorded at the centre of the vessel. There are two key assumptions made with this assessment method: that there is fully developed flow in rigid vessels, and that the liquid behaves as a Newtonian fluid. Depending on the circumstances of the measurement being made, there is the potential that neither of these assumptions are valid when performing measurements *in vivo*.

Another potential method to determine the WSS without having to acquire measurements close to the vessel wall was proposed by Blake et al. [9]. This method starts from an equation proposed by Womersley [44] for the velocity profile, *v(y,t)*, of a fluid in a long rigid pipe:

$$v(y,t) = \sum_{k=0}^{\infty} Re\left\{V_{mean,k} e^{j(k\omega t - \varphi k)} \left[\frac{J_0(\tau_k) - J_0(\tau_k y)}{J_0(\tau_k) - 2J_1(\tau_k)/\tau_k}\right]\right\} \tag{2.6}$$

Where y is the normalised radial component; t is time; k is a parameter describing flow conditions; $Re\{.\}$ represents the real part of a complex function; $V_{mean,k}$ are the Fourier components of the mean velocity; j is the imaginary number; ω is the angular frequency;

φ represents the phase of each harmonic; J_0 and J_1 are the zeroth and first order Bessel functions; and τ_k is given by:

$$\tau_k = R\sqrt{\frac{k\omega}{\sigma}}j^{3/2} \tag{2.7}$$

Where R is the vessel radius, and σ is the kinematic viscosity of the fluid.

The relationship between the Fourier components of the mean velocity can be related to the Fourier components of the peak (centre) velocity in the same terms:

$$V_{mean,k}e^{-j\varphi k} = V_{centre,k}e^{-j\varphi k}\left[\frac{J_0(\tau_k) - 2J_1(\tau_k)/\tau_k}{J_0(\tau_k) - 1}\right] \tag{2.8}$$

Equation 2.8 can then be inserted into Equation 2.9 to yield an expression for the velocity profile in terms of the centreline velocity:

$$v(y,t) = \sum_{k=0}^{\infty} Re\left\{V_{centre,k}e^{j(k\omega t - \varphi k)}\left[\frac{J_0(\tau_k) - J_0(\tau_k y)}{J_0(\tau_k) - 1}\right]\right\} \tag{2.9}$$

This expression of the velocity profile can then be used to calculate WSS as normal. As stated previously, this method relies on the assumption that the flow is laminar in rigid vessels and that the fluid is Newtonian. In principle, the Womersley conditions require steady flow; however, this is stated by the authors to be of negligible effect given that the frequency harmonics are separable. This means that the flow can be thought of as steady flow with a series of high frequency harmonics superimposed upon it. The authors tested this technique using a series of flow phantoms which were constructed such that distension was low, on the order of 1%, indicating that the Womersley conditions were

satisfied. This however, poses a challenge for the clinical situation and for methods such as in this study where the elasticity of the vessels is of diagnostic significance. While this technique has been used successfully in clinical situations to measure WSS [9,45], it has not lended itself to the quantification of the variation of WSS due to variation in vessel wall stiffness.

A significant shortcoming associated with these parabolic and Womersley profile assumptions is that the blood velocity profile is often not axisymmetric and fully developed *in vivo* which is a requirement for these techniques. This limits their applicability to vessels which are particularly long and straight, although is it not necessarily true that characteristically long and straight vessels will exhibit fully developed flow [46]. A study carried out by Mynard et al. [47] found that measurement of WSS using parabolic and Womersley velocity profile assumptions could result in errors of 30 – 60%.

2.2.4. Plane Wave Doppler Ultrasound Imaging

Another method of utilising ultrasound for the purposes of examining blood flow is to use *UltraFast* ultrasound imaging. Bercoff outlined the key principles behind *UltraFast* ultrasound [48]. In essence, the improved processing capabilities were the result of increased demand for performance and graphical display in the video game industry which lead to the development of complex multi-core CPU architecture that is the basis of *UltraFast* ultrasound imaging. In 2009, the company SuperSonic Imagine (Aix-en-Provence, France) released the first fully digital ultrasound scanner, the Aixplorer. The Aixplorer was unique in that it does not rely on an increased number of hardware processing channels and, instead, processes data entirely on its CPU and GPU. Due to the lack of integrated processing channels, the system is not limited by hardware and is capable of computing as many channels in parallel as is required, limited only by the

processing potential of the system. For conventional ultrasound systems, the time taken to build an image, T_{image} is given by the following:

$$\boldsymbol{T_{image} = \frac{N_{lines} * 2 * Z}{c}} \quad (2.10)$$

where: Z is the image depth, c is the speed of sound in tissue, and N_{lines} is the number of lines in the image. Traditionally, the only way to increase the framerate has been to utilise parallelisation schemes which process multiple image lines at once. Multi-line modes can intuitively also be used to increase the number of lines computed in an image without decreasing the framerate. The advantage of the Aixplorer digital architecture is its ability to process all lines in an image simultaneously, therefore, by utilising a plane ultrasound wave, *UltraFast* imaging need only be limited by the time of flight of the ultrasound pulse to and from the target depth. Bercoff goes on to suggest that due to the nature of the *UltraFast* regime, Doppler ultrasound can be completely re-envisioned. Instead of separate acquisitions of colour flow Doppler and quantitative spectral Doppler, quantitative Doppler data can be acquired for each pixel in a colour box in real time.

In a study carried out by Couture et al. [49], the use of *UltraFast* ultrasound imaging was investigated, specifically with respect to its effects on microbubble contrast agents. In this study, the tendency of microbubble contrast agents to rupture under significant acoustic radiation pressure was exploited to perform dissolution imaging in a wall-less vessel phantom. Lipid shell contrast agents (Bracco Research, Plan-les-ouates, Switzerland) were diluted in degassed water, this solution was then made to flow through the phantom via a gravity pump. It was stated in this study that, due to the nature of *UltraFast* imaging, there was a trade-off between signal-to-noise ratio and framerate; however, SNR can be regained through the use of multiple plane waves emitted at different angles and recombining successive backscattered echoes coherently. The study successfully imaged

the dissolution of microbubbles using *UltraFast* acquisition, which would have been impossible to achieve using conventional ultrasound imaging. In addition, it was found that tracking the dissolution of the microbubbles helped to distinguish microbubbles near a wall. Couture et al. suggested that the high temporal resolution could be applied to future work, specifically regarding new contrast imaging modalities such as attachment of microbubbles to diseased cells.

It is proposed herein that *UltraFast* imaging can be utilised in the assessment of WSS to overcome one of its key measurement limitations. Namely, the requirement for sufficient temporal resolution to evaluate the WSS at a single point in the cardiac cycle. Methods have been proposed in the literature to circumvent this problem using estimations based on fluid dynamics [9,13], however, this work aims to show that such estimations may not be necessary as the *UltraFast* imaging regime can evaluate the velocity at every point in the field of view simultaneously.

The subject of the minimum imaging capabilities of a particular technique to be considered adequate for measurement of WSS is somewhat vague. This section has discussed the importance of three particular parameters of note, namely, the spatial resolution, the temporal resolution, and the signal-to-noise ratio. The distinction between one imaging technique which is considered adequate and another which is not is somewhat arbitrary, however for the purposes of this work, the minimum requirements were defined thusly:

- The spatial resolution should be sufficient to allow for a minimum of 6 velocity values to be recorded in one vessel radius, or 12 measurements across the entire vessel diameter. As the expected velocity flow profile for fully developed flow is a parabola, which in ideal circumstances can

be fully described mathematically with data 3 points, 6 data points being twice the mathematical minimum was selected as a somewhat arbitrary real-world minimum. This value would allow for two measurements of WSS to be calculated, one from each side of the vessel, at each longitudinal vessel position while accounting for errors in velocity. For the renal artery, with a radius of ~3.6mm this would imply a minimum spatial resolution of ~0.6 mm

- The minimum value of temporal resolution should be such that the velocity of an entire region of interest (i.e. the entire vessel in the field of view) can be quantified at sufficient speed that the systolic velocity can be extracted without influence of the lower diastolic velocity which would result in a lower average velocity. It has been assumed previously that under a time period of 10 ms or shorter, arterial waveforms can be considered to be approximately constant [50].
- The minimum signal-to-noise ratio required for a WSS measurement is particularly difficult to quantify as it may be patient dependent (depth of vessel, overlying fat layers, etc.) therefore it was proposed that the ideal assessment technique should have a well-established contrast agent enhancement method. This would allow for fine control of SNR on a patient-by-patient basis.

Commented [AM5]: Added based on Dervil's comments

Table 2.1: The current techniques available for the assessment of WSS with advantages and disadvantages of each.

Technique	Advantages	Disadvantages
Phase contrast MRI	Superior anatomical detail Fully 3D flow imaging	Prohibitively long scan times Limited assessment capability close to vessel wall High cost
Particle image velocimetry	High precision of flow localisation Sub-millimetre scale assessment of WSS	Extremely limited penetration depth Cannot be utilised in abdomen or in large vessels
Doppler ultrasound	High spatial resolution Inexpensive Widely accessible	Limited temporal resolution Weak Doppler signal from blood Limited velocity resolution
Plane wave Doppler ultrasound	Superior temporal resolution Full velocity quantification in field of view simultaneously	Weak Doppler signal from blood Limited velocity resolution

Table 2.2: The current techniques available for the assessment of WSS with the minimum requirements for WSS assessment

Technique	Spatial resolution	Temporal resolution	SNR	Scan time
Phase contrast MRI	1 – 1.2 mm > 0.6 mm	25 – 30 s > 10 ms	Can be varied by contrast agent	25 – 30 s Reasonable for patient
Particle image velocimetry	~ 0.1 – 10 µm << 0.6 mm	~ 1 ms < 10 ms	Cannot be varied by contrast agent	450 ms Reasonable for patient
Doppler ultrasound	0.5 mm < 0.6 mm	~ 1 ms < 10 ms	Can be varied by contrast agent	~ 1 hour Not reasonable for patient
Plane wave Doppler ultrasound	0.1 mm < 0.6 mm	~ 0.2 ms < 10 ms	Can be varied by contrast agent	1 – 2 s Reasonable for patient

A summary of the discussed techniques in this section as well as their respective advantages and disadvantages is included in Table 2.1. It can be seen from this Table that, while all techniques provide a good level of accuracy in WSS measurements, PC-MRI and PIV have limited usefulness in clinical diagnostics due to limited temporal and spatial resolution (PC-MRI) and extremely limited penetration depth (PIV). Doppler ultrasound presents a number of disadvantages, one of which can be overcome by utilising plane wave acquisitions, namely the limited temporal resolution. It is clear therefore, that the

plane wave Doppler ultrasound assessment technique is potentially the most useful provided the velocity resolution and SNR can be improved.

2.3. Use of Test-bed phantoms for validation of new imaging techniques

To validate the efficacy of new Doppler ultrasound analysis techniques, it was necessary to develop a robust phantom test bed; this allowed for novel techniques to be tested in a reliably consistent test environment designed to be anatomically realistic without the full complexities inherent with imaging *in vivo*. Flow phantoms have been used in ultrasound quality assurance and as performance testing tools since the late 1980s and reviews of their usage and the materials used to substitute tissue are common [51,52]. The operating principle of these phantoms is the imitation of acoustic and mechanical tissue characteristics by varying the backscatter and attenuation values of the phantom, arguably the most important acoustic parameters for these phantoms to replicate are: acoustic velocity; attenuation coefficient; scattering coefficient; and non-linearity parameter. For phantoms utilised by elastography, mechanical properties such as Young's modulus are also important.

To date, many phantom designs have been used for assessment of Doppler ultrasound techniques. Law et al. [51] conducted a comprehensive review of early flow phantom designs featuring internal tubing composed of materials such as glass, quartz, Teflon, and a number of polymers. These materials have varying success at mimicking the acoustic behaviour of tissue *in vivo* as the materials can often cause unwanted distortion and attenuation of the ultrasound beam if not sufficiently acoustically analogous to human tissue. Consequently some researchers have attempted to reproduce realistic physical models of human vasculature through the use of excised vessels from human cadavers

[53,54]. It has been shown, however, that excised arteries are susceptible to acoustic and geometric changes if not correctly stored and maintained [55]. It is also difficult to characterise excised vessels to allow for a high standard of acoustic and geometric reproducibility across phantoms. Additionally, the use of excised human tissue requires strict adherence to legislation and consideration of biological safety hazards that are not a concern when using non-biological materials. It is therefore desirable in the production of flow phantoms to use materials which can be well characterised and reproduced consistently to a high degree of acoustic and mechanical precision. One such material is polyvinyl alcohol cryogel (PVA-c).

King et al. [56] outlined a procedure for the development of a PVA-c based vessel mimicking material (VMM) which can be manipulated into a variety of complex vessel geometries and maintains long term stability. PVA-c has the advantage of an adjustable mechanical stiffness: as the PVA-c is subjected to sequential freeze-thaw cycles, the material stiffness increases due to molecular cross-linking. The study aimed to test the effects of varying the number of freeze thaw cycles for several PVA-c samples of different production recipes. For each PVA-c type, 6 samples were produced each exposed to a different number of freeze thaw cycles (1-6). Overall it was found that the acoustic velocity of the material increased with increasing freeze thaw cycles, increasing from 1510 ± 5 m s^{-1} to 1562 ± 5 m s^{-1}, an approximate acoustic velocity increase of 10 m s^{-1} per f/t cycle. The Young's modulus was observed to increase with increasing freeze-thaw cycles, although there was a levelling off after 5 freeze thaw cycles. It was suggested that this plateau was the result of the PVA-c reaching a saturation of molecular cross-linking. Additionally, it was found that the silicon carbide particles had a significant sedimentation problem which could not be overcome, resulting in two distinct layers in the VMM sample containing SiC. It was because of this sedimentation problem that the

optimum VMM recommended did not contain silicon carbide and, instead, it was advised that VMM should be made using only PVA-c and an anti-bacterial agent. Based on the results for acoustic velocity of the samples, the author recommended using two freeze thaw cycles as the speed of sound (1538 m s^{-1}) most closely resembled the speed of sound in tissue (1540 m s^{-1}).

Another study which examined the use of PVA-c as a tissue mimicking material was Cournane at al. which used PVA-c in order to reproduce the mechanical characteristics of tissue precisely [57]. In this study, PVA-c was used in addition to an anti-bacterial agent (benzalkonium chloride), aluminium oxide (Al_2O_3) acoustic scatterers (0.3µm) to provide the Doppler speckle and increase the acoustic attenuation coefficient, and glycerol ($C_3H_8O_3$) to vary the acoustic velocity. The acoustic properties of the PVA-c samples were determined using a custom scanning acoustic macroscope system and mechanical properties were determined using a LR30K*Plus* system (Lloyd Instruments, UK). The study claimed that the results showed a successful application of low concentration PVA-c for mimicking a range of shear elastic modulus and acoustic velocity values of the liver. It was stated, however, that because PVA-c is considered to be approximately elastic and so doesn't accurately mimic the shear loss modulus of the liver tissue which is considered to have highly lossy viscoelastic properties at a shear wave frequency of 50 Hz. Overall, the study concluded that PVA-c worked well as a tissue mimicking material (TMM) for representing liver tissue.

Commented [AM6]: Added based on Kumar's comment

Commented [AM7]: Kumar's comment.

Commented [AM8]: Kumar's comment

When designing anatomically realistic flow phantoms, one key consideration to take into account is the state of disease in the tissue. Of particular interest for this work is the production of artificial plaques and stenoses in the vessel itself. Ramnarine et al. [58] conducted a study which investigated the use of shear wave elastography on vessel phantoms which simulated both soft hard and carotid plaque characteristics. In this study,

PVA-c was utilised as a vessel mimicking material to make three sample vessels which were submerged in a water-glycerol bath. The vessels produced were: a homogenous standard PVA-c vessel; a "hard" phantom which contained a piece of PVA-c within a stenosis which had previously undergone two freeze thaw cycles prior to the production of the rest of the vessel; and a "soft" phantom in which butter was enclosed in the stenosis. Blood mimicking fluid was pumped through these vessel using both steady and pulsatile flow conditions. The phantoms were then analysed using shear wave elastography with an Aixplorer ultrasound system with L15-4 probe (Supersonic Imagine). The authors conclude that the plaques used in this study represent true anatomical conditions which were useful in calibration and optimisation of the shear wave elastography settings without any time constraint.

In another study focused on plaque characterisation, shear wave elastography was used to characterise hard and soft plaque inclusions in carotid artery phantoms [59]. The soft plaque inclusions for this study were created by first moulding a vessel around a bronze rod with a diameter of 6 mm and a 1.5 mm extension attached to create a cavity in the vessel wall. This PVA-c vessel was then subjected to two freeze thaw cycles. Following this, a small sample of the PVA-c solution was injected into the cavity before the entire vessel was exposed to an additional freeze thaw cycle. The hard plaque inclusions were produced by separately subjecting PVA-c samples to seven freeze thaw cycles before placing them in an acrylic mould which had PVA-c poured into it. The vessel was then subjected to a further three freeze thaw cycles. Two control vessels were made without any plaque inclusions, one for each mould used for the soft and hard plaque inclusion vessels. The vessels were then tested using shear wave elastography to attempt to measure quantitatively the plaque characteristics and compare the results to mechanical testing and, therefore, characterise the mechanical parameters of soft and hard plaques for shear

wave elastography. The results show that there was good agreement between the shear wave assessment and the mechanical testing, with a slight overestimation in the SWE measurements of shear moduli for both soft and hard plaques, and a slight underestimation in the SWE measurements of shear moduli in the vessel wall. The study concluded that the plaque utilised in the phantoms was a good mimic of the clinical setting, however, there were some limitations of the work. It was pointed out, for example, that the plaques used in this study were uniformly hard or soft, whereas real atherosclerotic plaques are inhomogeneous, consisting of calcified, fibrous, and necrotic regions.

Chatelin et al. [60] introduced a method for producing a fibrous soft tissue analogue using PVA-c. The motivation for this study was the inability of phantoms to mimic soft tissue which is predominantly composed of fibres, such as muscles tendons, and cerebral tissues. The study uses PVA-c due to its highly controllable mechanical parameters; the goal of the study was to create an anisotropic PVA hydrogel. This was achieved by first subjecting the PVA-c to two freeze thaw cycles. Following this, the sample was subjected to a further three freeze thaw cycles while placed in a modified tensile test setup which stretched the material to 180% of its original length. This was done so as to promote polymer cross-linking in a preferred direction. A second PVA-c sample was prepared under the same conditions without being placed in the stretching apparatus to act as a control. The anisotropy was then characterised using shear wave elastography on an *UltraFast* Aixplorer system (Supersonic Imagine, Aix-en-Provence, France). It was determined that the PVA-c was incompressible for small strains, it was additionally assumed that the PVA-c would be linearly elastic, although this was not determined during the study. The overall results were a success, with the phantom accurately mimicking the desired mechanical anisotropy of biological fibrous tissues. The authors

suggest that this makes the phantom ideal for the study of anisotropy and development of new techniques based around it, such as new ultrasound probes designed for musculoskeletal and cardiac applications.

2.3.1. Acoustic and mechanical properties of tissue mimics

A full review of physical tissue properties was carried out previously by Duck [4]. Mechanical properties of arteries are more difficult to establish. The full elastic properties of a human artery vary significantly with respect to the layer of the vessel examined, however the layer which is of most concern to the development of atherosclerosis is the innermost arterial layer, the intima, which consists of the basal lamina and the endothelial cells. McKee et al. [61] showed that there are significant differences between measured Young's modulus values of human arteries in the literature, sometimes spanning several orders of magnitude. When measured using indentation techniques, such as the tip of an atomic force microscope, the values recorded for veins and arteries spanned the range of 6.5 – 560 kPa. However, the same tissues were recorded in the range of 600 – 3500 kPa when using tensile mechanical measurements. It was readily concluded that these results implied that the elastic properties of tissue are not constant for all length scales and that care must be taken to ensure the correct measurement is recorded for the correct application. One possible cause of this discrepancy suggested by the author was trapped water in tissue which, due to its incompressibility, increased the Young's modulus of the tissue. In the specific case regarding arteries, it is likely that a significant degree of bulk elastic properties from the adventitia were offsetting the relatively lower Young's moduli of the media and the intima. This would indicate that a more accurate modulus value to aim for is the values of the inner layers exclusively rather than a modulus measurement from the entire vessel. Jacot et al. [62] made micro-indentation measurements of the

Commented [AM9]: Reworded based on Kumar's comment

luminal side of an excised human saphenous vein, ~1 cm long, sliced open longitudinally. They recorded an elastic modulus of 8.2 ± 3.8 kPa. The measurement was independent of position and there was no significant difference detected for subsequent measurements of the same position. A similar measurement was made by Engler et al. [63] which showed that the Young's modulus of the medial artery layer was approximately in the range 5 – 8 kPa. Another indentation experiment carried out by Lundkvist et al. [64] showed that the elastic modulus of the intimal wall of a healthy femoral artery was 34.3 kPa. More recently, Rezvani-Sharif et al. [65] have shown that a typical healthy artery will have a Young's modulus of approximately 24.8 – 34.9 kPa from the internal elastic lamina. Similarly, the values for diseased and fibrous arterial tissue has been reported to range from 182 – 649 kPa [66]. A systematic review of elasticity values reported in the literature was carried out by Boesen et al. [67] They found that the Young's modulus varied from 39.7 – 83 kPa for healthy vessels, while diseased vessels were found to have values in the region 116 – 751 kPa.

2.4. Summary

Cardiovascular disease is among the leading causes of death in the world and is associated with a number of additional life threatening and life limited conditions. However, the methods used in the diagnosis of CVD are largely dependent on detecting the presence of arterial stenoses, which are associated with the later stages of the disease. When diagnosed, the treatment methods for CVD are largely surgical, which carry inherent risk to the patient.

There exists, therefore, a clinical interest in the development and optimisation of a diagnostic screening technique which can be applied earlier in the disease stages to indicate a patients risk of further atherogenesis.

A potential clinical biomarker which could be used as part of this screening technique is wall shear stress, which is related to the blood velocity profile. By precisely measuring the velocity of the blood close to the vessel wall, an indicator of arterial health can be established which could provide early treatment options which would potentially be considerably safer for the patient.

A number of methods of assessing WSS have been presented each with advantages and disadvantages; however, there remains a critical need for a widely available clinical technique which can provide an accurate WSS measurement with a high degree of precision.

Chapter 3: Ultrasound scanning system calibration

3.1. Introduction

This chapter outlines the calibration and characterisation of the Aixplorer ultrasound system (Supersonic Imagine, France) as well as experimentation to determine the reproducibility of certain aspects of the data acquisition. When undertaking testing of new diagnostic techniques, it was important to ensure that the system was responding appropriately and within expected tolerances. The properties of interest for the Aixplorer system were the acoustic characteristics of its pulses, the Doppler dynamic range, and the intrinsic spectral broadening. The pulse characteristics provided understanding of the effect of transmission settings on the pulse bandwidth, an important parameter because it determines the limits of integration of multifrequency Fourier analysis in Chapter 4. The Doppler dynamic range provides insight into the ability of the Aixplorer system to simultaneously display sonogram intensities, as very weak blood signals could be muted by adjacent strong velocity and tissue signals and situations in which the signal-to-noise ratio is too high for the system could result in the saturation of the Doppler spectrum. It was important to measure the intrinsic spectral broadening due to its effect on the overestimation of velocity in Doppler ultrasound and the inaccuracies this brings; using this data it would be possible to implement a correction factor to ensure that the recorded velocities were as accurate as possible.

Additionally, the geometry of the flow phantoms necessitated the repositioning of the transducer multiple times to fully evaluate the blood flow profile at all points in the vessel so it was important to ensure that the repositioning of the transducer did not result in misalignments which would introduce inaccuracies to the results.

3.1.1. Transmission characteristics

3.1.1.1. Tissue effects

Ultrasound pulses are mechanical waves which interact with the media they pass through by imparting energy in the form of either absorption or reflecting the ultrasound wave. This property of ultrasound can be useful and is the basis for a number of diagnostic techniques such as measuring fluid viscosity [68], elastography [69], and remote palpitation of tissues [70]. This property is also associated with a number of bio-effects such as tissue heating, acoustic cavitation and non-linear signal reflection.

In the absence of bone from the insonation field, the temperature rise in tissue is normally not pronounced and expressed in degrees Celsius by the thermal index (TI) of the scanner, intended to give a rough guide to the likely maximum temperature rise that might be produced after long exposure [71]. The temperature rise in the tissue is proportional to beam intensity and so will be greatest at the beam focus. In practice the rate of temperature rise at the focus of the beam will equal the rate of temperature loss to conduction to surrounding tissues and convection from surrounding blood when equilibrium is reached, after approximately 30 seconds [3]. Over longer scanning times, heating in regions insonated by a wider cross-section of the beam will begin to heat up due to not being as efficiently cooled by conduction. This effect is compounded close to the transducer surface which itself will also begin to heat up over longer periods of insonation [3]. In principle, these thermal effects are small and likely not to be of concern for most patients. The one area in which the tissue heating may be significant is in routine pre-natal ultrasound scanning [72].

Aside from the indirect thermal effects of ultrasound beams, the other main effect on tissue is that of mechanical effects. A mechanical effect which can be of concern in patient imaging is cavitation, whereby the ultrasound waves interacts with gas bubbles in a liquid.

Commented [AM10]: Changed from "significant" to avoid confusion. Based on Kumar's comment

Cavitation is typically split into two categories, stables and inertial. In stable cavitation, the bubble expands and contracts in response to the pressure variation of the ultrasound pulse, resulting in a period "breathing" motion. This can lead to damage of cells which are in suspension and can act as cavitation nuclei such as erythrocytes, leucocytes, and platelets when the cell membranes rupture from the high shear forces that stable cavitation produces. Inertial cavitation, by contrast, is a more violent and potentially destructive interaction between ultrasound and suspended nuclei. Inertial cavitation is typically caused by large pressures associated with short, high intensity pulses. The strength of these pulses cause the suspended bubbles to undergo dramatic size variations and can collapse due to the inertia of the surrounding liquid. The potentially harmful effects of cavitation led to the development of the mechanical index (MI) which is defined as the ratio of the peak negative pressure of the pulse to the square root of the pulse transmission frequency. It is believed that for mechanical indices lower than 0.7, the physical conditions for inertial cavitation cannot develop [3,73]. Table 3.1 illustrates the recommended exposure times and index levels for obstetric and neonatal ultrasound, while Table 3.2 illustrates the recommended exposure times and index levels for non-obstetric and non-neonatal ultrasound.

Table 3.1: BMUS recommended exposure limit index values for obstetric and neonatal ultrasound [8]**.**

Application	**Thermal index value**			**Mechanical index value**		
	0 – 0.7	**0.7 – 3.0**	**>3.0**	**0 – 0.3**	**>0.3**	**>0.7**
Obstetrics up to 10 weeks	Safe	Time limited	Not recommended	Safe	Safe	Risk of cavitation
Obstetrics more than 10 weeks	Safe	Time limited	Not recommended	Safe	Safe	Risk of cavitation
Neonatal – transcranial and spinal	Safe	Time limited	Not recommended	Safe	Safe	Risk of cavitation
Neonatal – general and cardiac	Safe	Time limited	Time limited	Safe	Time limited	Risk of cavitation
Foetal Doppler heart monitoring	Safe	Safe	Safe	Safe	Safe	Safe

Table 3.2: BMUS recommended exposure times and index values for non-obstetric and non-neonatal ultrasound [8]**.**

Application	**Thermal index value**		**Mechanical index value**	
	0 – 1.0	**>1.0**	**0 – 0.3**	**>0.7**
General abdominal	Safe	Time limited	Safe	Risk of cavitation
Peripheral vascular	Safe	Time limited	Safe	Risk of cavitation
Unlisted applications	Safe	Time limited	Safe	Risk of cavitation
Eye	Safe	Not recommended	Safe	Risk of cavitation
Adult transcranial	Safe	Time limited	Safe	Risk of cavitation
Peripheral pulse monitoring	Safe	Safe	Safe	Safe

In principle, the thermal and mechanical indices allow for ultrasound operators to ensure that the transmitted pulses do not exceed dangerous levels. The current BMUS guidelines [8] state that for obstetric and neonatal imaging TIs between 0 – 0.7 are typically safe, TIs between 0.7 – 3.0 are safe for limited periods of time depending on certain factors and what tissue is being imaged, and scanning with TIs above 3.0 is not recommended. For non-obstetric and non-neonatal imaging, TIs between 0 – 1.0 for all imaging applications. TIs above 1.0 are safe for limited periods of time for most applications depending on the tissue being imaged with the exception of the eye, which should not be imaged with a TI greater than 1.0. The guidelines also state that mechanical indices < 0.7 are typically safe outside of general and cardiac neonatal imaging, where indices > 0.3 can result in lung or intestine damage [8].

Another consideration for pulse characteristics is the susceptibility of microbubble contrast agents to cavitation effects. As a large enough Doppler pulse pressure could

result in the rupture of contrast agents in the region of view and lead to a sudden increase in signal-to-noise ratio (SNR), which then falls off. In the case of the SonoVue contrast agent, this maximum pressure above which changes to bubble characteristics are observed is 150 kPa, and bubble destruction occurs at pressures exceeding 300 kPa [74]. This is an important consideration for application of contrast agents to Doppler measurements as the destruction of bubbles can be both a hindrance or deliberate to give momentary increases in SNR or to observe how inflowing blood perfuses tissue [74].

3.1.1.2. Pulse parameters

The central transmission frequency and the frequency bandwidth can have a significant effect on imaging. High transmission frequencies are more strongly attenuated by the media they pass through, limiting their maximum penetration depth. The benefit of high transmission frequencies is an increase in axial resolution and an increase in velocity accuracy in Doppler [3]. This is not a trivial effect for Doppler diagnostics as in order to measure the blood flow for larger tumours the frequency must be lowered relative to small tumours resulting in higher blood velocities becoming aliased [75].

An important part of this work was to develop new spectral analysis methods for Doppler ultrasound that allow for greater velocity resolution and SNR over PW Doppler by reducing the spectral variance of the received Doppler echoes. It is worth noting that SNR is generally based on purely the parameters of the acquisition and cannot be improved using post-processing techniques. What this method set out to achieve was to capture additional signal information present in the returning pulse that is normally not utilised by traditional 1-dimensional Fourier techniques thus the SNR was "increased" over standard methods through improved analysis efficiency. The technique developed for this was the multifrequency *UltraFast* Doppler spectral analysis (MFUDSA) algorithm. The specifics of this algorithm are given in Chapter 4 but, briefly, the algorithm relied on the

extraction of additional spectral information from the full bandwidth of transmitted frequencies. The MFUDSA required the integration of the Doppler response in the frequency space with the transmitted frequency bandwidth acting as the limits of integration. It is well understood that the length of an ultrasound pulse is inversely proportional to the bandwidth of transmitted frequencies [76]. This is, more generally, a property of all waves and is due to the limitation of distance and frequency resolution whereby increasing the former, results in a decrease in the latter. This also means that for long pulses with small frequency bandwidths there is also a corresponding increase in axial and lateral resolution [3,77].

An additional motivation for analysing the pulse parameters of the incident ultrasound that would be used later in this work was the application of the so-called *UltraFast* Doppler ultrasound. This is a new diagnostic technique available on the Aixplorer system which was first outlined by Bercoff et al. [78,79]. In principle, a single element transducer or a transducer making a flat acquisition would have a maximum frame rate determined by the speed of sound of the insonified material and the depth of interest:

$$PRF_{depth} = \frac{c}{2Z} \tag{3.1}$$

Where PRF_{max} is the maximum frame rate, c is the speed of sound, and Z is the depth. This is the maximum frame rate that can physically be achieved by any ultrasound system at the cost of significant spatial resolution. Typically, an ultrasound insonation is carried out in an element-wise process with each individual element firing and waiting to receive an echo, reducing the frame rate substantially but recovering the spatial resolution:

$$PRF = \frac{c}{2Z}\frac{1}{N_{lines}} \tag{3.2}$$

Where N_{lines} is the number of transmitted lines from the transducer. In practice, various firing regimes can be applied to increase the effective frame rate by a factor of 2-4, however. This process is more complex for Doppler imaging. In colour Doppler, flow velocity estimation is carried out by insonating the medium with N pulses (known as the ensemble length) set to a fixed pulse repetition frequency (PRF). To avoid aliasing, this PRF cannot drop below twice the maximum Doppler frequency:

$$PRF_{flow} \geq 2F_D \tag{3.3}$$

Where F_D is the maximum Doppler frequency. This means that, for colour Doppler, the number of lines in an image that can be scanned is limited by the ratio of two PRFs, the PRF_{depth} which is determined by the depth of the vessel and the PRF_{flow} which is determined by the maximum velocity of the blood. This means that the maximum number of lines that can be insonated before beginning again is the limited to:

$$N_{lines} = \frac{PRF_{depth}}{PRF_{flow}} \tag{3.4}$$

In cases where the region of interest is composed of more lines than N_{lines}, the region must be subdivided into a number of segments, $N_{segments}$. It follows that the total number of firings necessary to compute a colour Doppler image is:

$$N_{firingsC} = N_{lines} * N_{Segments} * N \tag{3.5}$$

In *UltraFast* imaging, the elements of the transducer do not need to be individually fired because the entire imaging region is insonated by a series of tilted plane waves at a number of angles which can be iteratively reconstructed to recover the spatial resolution. The maximum number of tilted plane waves that can be fired is the same as the number of lines which can be fired in a conventional scan:

$$N_{angles} = \frac{PRF_{depth}}{PRF_{flow}} \tag{3.6}$$

Because the entire imaging region is insonated instantaneously, there is no need to subdivide the image into segments as with conventional imaging, meaning the total number of firings necessary to produce the image is given by:

$$N_{firingsU} = N_{angles} * N \tag{3.7}$$

The factor increase in frame rate associated with *UltraFast* Doppler is therefore equal to $N_{segments}$. For typical colour flow imaging at high flow speeds, $N_{segments} \approx 64$. For lower flow speeds, this gain is less significant ($N_{segments} = 1 - 3$) but there is still significant improvement over conventional colour flow imaging as each pixel is insonified many more times (a factor of N_{angles} increase) [79].

Bercoff et al. [79] carried out a comprehensive analysis of the performance of *UltraFast* Doppler versus conventional colour Doppler and found that the *UltraFast* mode considerably outperformed the conventional mode with a reduction in acquisition time of up to a factor of 16 with no loss in image quality. A secondary experiment was carried out where the ensemble length of the *UltraFast* mode was progressively lowered to increase temporal resolution and even at its lowest level, corresponding to a factor of 14

Commented [AM11]: Added based on Kumar's comment

increase in temporal resolution, the *UltraFast* mode still maintained greater image fidelity. When examining low flow in small vessels, the *UltraFast* protocol exhibited a decrease in variance by a factor of 14 and greater flow sensitivity.

3.1.2. Intrinsic Spectral Broadening

All Doppler ultrasound measurements are subject to an inherent broadening of the received Doppler shift frequencies due to a number of physical effects inherent to ultrasound imaging. This effect, known as intrinsic spectral broadening (ISB), is caused predominantly by two effects, transit time broadening (TTB) and geometric spectral broadening (GSB). Early work in the 1970s and 1980s by Newhouse et al. [80–82] outlined the physical phenomena behind both factors of spectral broadening. TTB can be thought of as a single flow line crossing an incident focused ultrasound beam, a scatterer moving through the beam will have a finite transit time due to the finite beam width which leads to a broadening of the received echoes from this scatterer [81]. Conversely GSB is caused by the fact that two adjacent transducer elements will have slightly different insonation angles which results in each element recording a different Doppler frequency due to the angle dependence of the Doppler equation [3,80]. It has been observed that for beam angles of 60° velocity overestimation of up to 40% has been present [83].

Commented [AM12]: Added based on kumars comment

Newhouse et al provided a theoretical basis for the understanding of ISB in the literature and concluded that "[TTB and GSB] were proved to be one and the same effect" [82]. This conclusion was a consequence of the discovery that a similar property had been found in the related field of laser Doppler radar, known as "Doppler radar ambiguity" and "wave vector ambiguity". Guidi et al. [84] provides a detailed breakdown of the history of the literature surrounding TTB and GSB and illustrates a framework for the understanding of TTB and GSB as separate phenomena rather than being equivalent. The authors states that the beam width of an ultrasound pulse at its focus is related to the ratio

of the aperture width and the focal length and as such the distance a scatterer needs to cross is directly dependent of the geometric properties of the transducer. Guidi et al. therefore concluded that the statement "TTB and GSB are equivalent" should be suffixed by the additional qualifier "at the transducer focus".

Commented [AM13]: Added based on kumars comment

Comprehensive work has been carried out to characterise the degree of velocity overestimation for a number of parameters for various Doppler systems. Hoskins undertook a large scale test of the response of ISB to various factors [85]. Using a string phantom calibrated to have known velocities, 14 transducers across 7 systems were tested for a range of velocities, beam filament angles, and depths. The error in maximum velocity varied between -4% and +47%. Looking the parameters individually; it was founded that the velocity had no effect on ISB for a range of 50 – 250 cm s^{-1} and the depth similarly had no effect across 20 – 150 mm. The beam filament angle on the other hand had a dramatic effect with a significant increase in ISB as the angle varied from 40 – 70°. Despite the velocity and depth not having an effect on ISB, the system still recorded overestimated maximum velocities for the lowest beam filament angle of 20%, indicating that there is no critical angle below which there is not an error associated with the maximum velocity.

Hoskins presented a method for correcting the maximum velocity of the Doppler spectrum by calibrating each transducer of a scanner using a string phantom of known velocity outputs [86]. A correction factor can be made by setting up a string phantom with the same acquisitions parameters that will be used for flow measurements (velocity, depth, beam angle, and aperture position) and determining the percentage of ISB and the percentage velocity error according to the equations:

$$ISB(\%) = \left(\frac{V_{max} - V_{min}}{V_{max} + V_{min}}\right) * 100 \quad (3.8)$$

$$Error(\%) = \left(\left[\frac{V_{max}}{V_{string}}\right] - 1\right) * 100 \quad (3.9)$$

Where V_{max} is the maximum velocity of the Doppler spectrum, V_{min} is the minimum velocity of the Doppler spectrum, and V_{string} is the true velocity of the string phantom. These values can be used to apply a correction factor to the Doppler spectrum and improve the accuracy of flow based analysis.

Another option to reduce the influence of ISB was proposed by Osmanski et al [1]. This method relies on the fact that for a scatterer of a single velocity interrogated with an ultrasound beam of infinitesimal beam width, the Doppler spectrum would be a single line corresponding to the Doppler frequency shift of the scatterer velocity. The spectrum of Doppler frequencies recorded is due to a number of factors, ISB as previously discussed is one factor, but a spread of blood velocities within the range gate would also lead to a broadening of the Doppler spectrum. The correction factor method proposed by Hoskins attempts to quantify just the ISB by measuring the broadening for a string phantom which has only a single velocity. This then allows the ISB to be discounted and any remaining broadening in the spectrum is considered to be due to velocity variation. Osmanski et al. proposes instead that, when using *UltraFast* Doppler, it is possible to remove the ISB without previously determining the velocity correction factor with a string phantom.

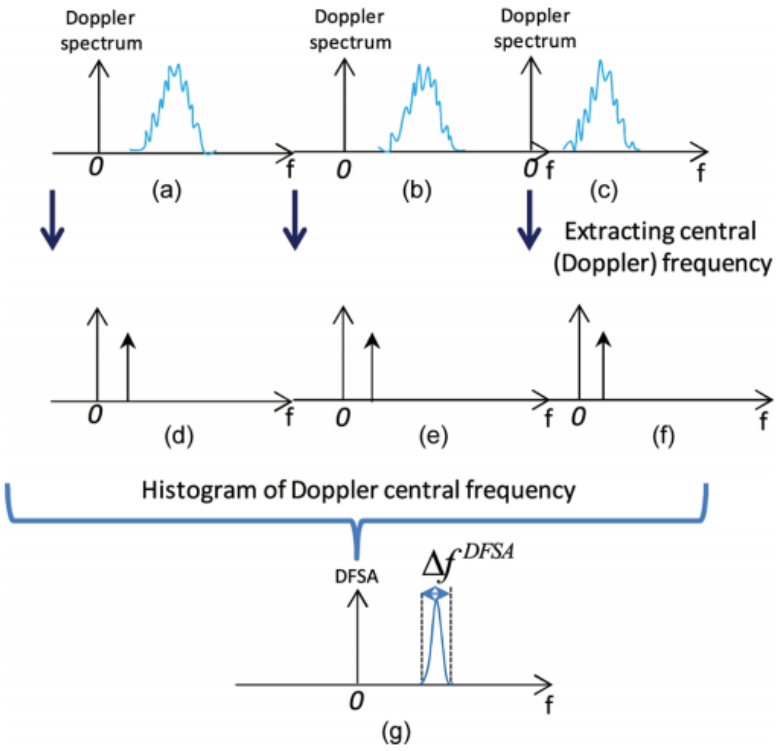

Figure 3.1: Illustrative diagram of the method proposed by Osmanski et al. Adapted from Osmanksi et al. [1]***. (a)-(c) three Doppler spectra are extracted from different longitudinal positions in a vessel. (d)-(f) the central frequency of each spectra is computed. (g) The central frequencies are combined to produce a unified spectra.***

This method relies on the *UltraFast* mode allowing the complete insonation of an imaging region simultaneously. This allows for multiple spectra to be selected at different longitudinal points in a vessel (but at the same radial position) which should represent the same collection of velocities but will have different central frequencies due to the variation in velocity present at that radial position. The central frequencies can then be

extracted and the remaining spectra discarded. The central frequencies are then combined to form a new spectra of which the broadening is only caused by velocity variation and no ISB remains. This methodology was tested using an agar based flow phantom and *in vivo* using data recorded from a healthy human carotid artery. The results of this analysis found that this cancellation method reduced the ISB by a factor of 7 ± 4 *in vitro* and 6.5 ± 3 *in vivo* compared to a theoretical prediction of 5.9 ± 0.2. The author states that the slight disagreement between the experimental results and the theoretical value is likely due to the assumption that the velocity spectrum is Gaussian in the theoretical model.

3.1.3. Dynamic Range

The dynamic range (DR) is a measurement of an ultrasound system's ability to accurately represent the full range of echo intensities present in a received pulse [3]. It can be defined as the ratio of the largest echo amplitude which can be measured without causing saturation to the smallest echo amplitude that can be detected, a quantity which can be calculated using Equation 3.10.

$$DR = 10 \log_{10} \left(\frac{I_2}{I_1} \right) \tag{3.10}$$

In order to accurately represent the detail of objects in the imaging region, the voltages recorded by the transducer for a received echo are converted into greyscale values based on the size of the voltage, i.e. the intensity of the backscatter. This can pose a problem due to the finite bit size devoted to displaying pixel intensities. In most display units the greyscale value of a pixel is assigned 8 bits or 256 possible values. This corresponds to a maximum difference between the darkest and brightest part of the screen of approximately 24 dB. Due to the differences in backscatter between interfaces, there can often be very large differences in voltages for different reflections, for example a tissue-air or a tissue-liver interface would yield a large reflection whereas the signal from blood

would comparatively be quite weak. This means that for B-mode scanning, very large dynamic ranges are necessary in the transducer architecture to ensure that all the echoes can be recorded, often as high as 100 dB [3].

The effective dynamic range, when the information is displayed, is often different due to the limitations of the display capabilities, so the received voltages are typically passed through a compression procedure which uses a non-linear amplifier to boost the signals from weak echoes. This means the effective dynamic range is often much less than that of the transducer. Similar to B-mode, the Doppler spectrum must also be contained within the 24 dB limit of the display unit being used. This means that a flow system which has air in it or a large concentration of microbubble contrast agents can quickly become saturated and difficult to parse.

Despite the importance of having a high dynamic range, particularly when utilising contrast agents which have a greater chance of saturating the Doppler spectrum, there has thus far been limited investigation in the literature into the effective dynamic range of Doppler systems or the measurement of this quantity. It is thus believed that the procedure presented in this work is an important step in quality assurance for ultrasound scanners and the neglection of its measurement represents a gap in the literature. This is despite the fact that dynamic range is listed as a parameter which should be prioritised by the American Institute for Ultrasound in Medicine (AIUM) and the Institute of Physical Sciences in Medicine (currently the Institute of Physics and Engineering in Medicine (IPEM)) [87].

One method through which the dynamic range can be evaluated is by analysing the effect of the Doppler spectrum of increasing the concentration of high-backscatter materials. One such material which is a common component in blood mimicking fluid (BMF) is

Orgasol®. Ramnarine et al. [2] demonstrated the relative backscatter of Orgasol® particles in BMF solutions with varying particle concentrations for a number of particle sizes as seen in Figure 3.2. Therefore, a series of BMF solutions could be manufactured with a varying concentration of Orgasol® particles and used to test the resolvable limits of an ultrasound systems dynamic range.

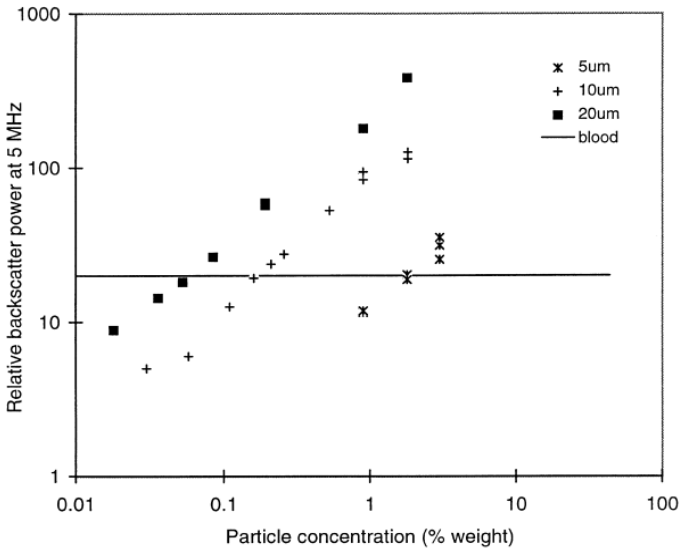

Figure 3.2: The relative backscatter of BMF featuring varying concentrations of Orgasol® particles of different sizes. The solid line indicates the backscatter of blood – adapted from Ramnarine et al [2]**.**

3.2. Methodology

3.2.1. Measurement of Aixplorer pulse characteristics

This experiment was designed to measure the pulse bandwidth and pulse pressure for a range of different acquisition regimes. Both the bandwidth and the acoustic pressure of the pulse were measured using a needle hydrophone (SN1548, Precision Acoustics, UK) in conjunction with a pulse amplifier (PA10019, Precision Acoustics, UK). A hydrophone is a passive single element transducer which can precisely measure incident insonation. The apparatus for conducting this experiment is shown in Figure 3.3.

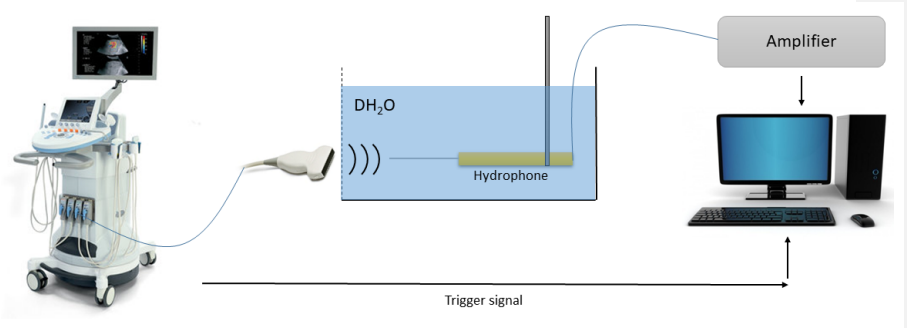

Figure 3.3: The apparatus used for the measurement of the Aixplorer pulse characteristics. The hydrophone was placed in a container with an acoustically transparent window and submerged in deionised water.

The hydrophone was connected to a mount on a vibration excluding track used for optics experiments and then placed in a specially constructed tank featuring an acoustically transparent window made of cellophane, positioned parallel to the optical track. The tank was filled with deionised water and the SuperLinear™ SL15-4 transducer (Supersonic Imagine, France) was clamped and coupled to the acoustically transparent window with a layer of ultrasound gel. Using the Aixplorer B-mode imaging as a guide, the hydrophone

was carefully manipulated to lie in the imaging plane of the transducer. It was then possible to precisely adjust the hydrophones axial position by moving it along the optical track; allowing the tip of the hydrophone to be placed exactly at the transducer focus. The apparatus was then left overnight to allow the tank water to degas.

A programme was written in LabVIEW (National Instruments, USA) to control and record the hydrophone voltage measurements in response to the incident pulse. The programme was designed to initiate the measurement when it received an input trigger from the scanner, the hydrophone would then record the signal as an array of voltages which would be passed through an amplifier and saved as a .txt file by the LabVIEW programme. The amplifier was set by trial and error using the signal display in LabVIEW to maximise the signal without saturating it. The parameters for this experiment are given in Table 3.3, for each possible combination of parameters three pulses were recorded.

Table 3.3: Transmission parameters for which pulses were recorded using the hydrophone

Frequency (MHz)	5.0, 5.6, 6.4, 7.5, 9.5, 11.25
Pulse length (transducer half cycles)	2, 4, 6, 8, 10, 12

An example of the voltage with respect to time recorded by the hydrophone is shown in Figure 3.4.

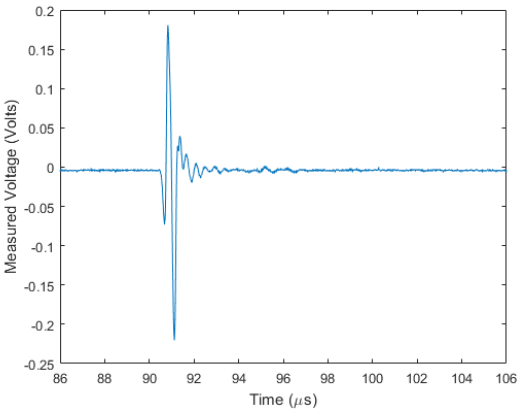

Figure 3.4: An example pulse recorded by the hydrophone

The recorded voltage data was analysed using a custom MATLAB (Mathworks, USA) programme. The first half of the programme calculated the frequency bandwidth by applying a Welch transform to the recorded signal. Once in frequency space, the programme could calculate the full width at half maximum (FWHM) of the central peak as a measurement of the frequency bandwidth.

The second half of the programme was used to calculate the peak positive and negative pressures of the pulse. This was done by applying a conversion factor described in [88]. This conversion is shown in Equation 3.11.

$$P(t) = \mathcal{F}^{-1}\left\{\frac{\mathcal{F}(V(t))}{M_H(\omega)}\right\} \tag{3.11}$$

Where P was the pressure, V was the measured voltage, $\mathcal{F}$ and $\mathcal{F}^{-1}$ were the Fourier and inverse Fourier transforms, respectively, and $M_H(\omega)$ was the hydrophone frequency response.

The sensitivity of the hydrophone was only measured at integer frequencies, the model of this systems power function was determined in an earlier study [89], and this profile was used with the power function to interpolate the data points between these measured values. This was done by fitting the data in the calibration certificate (Figure 3.5) with a power function:

$$\mathrm{M}(\omega) = \frac{\mathrm{S}(\omega)}{\mathrm{J}} \tag{3.12}$$

where S(ω) is the transmit sensitivity, *J* is the reciprocity parameter, $J = 2A/\rho c$, A is the area of the transducer, ρ is the medium density, and *c* is the speed of sound in the medium [89].

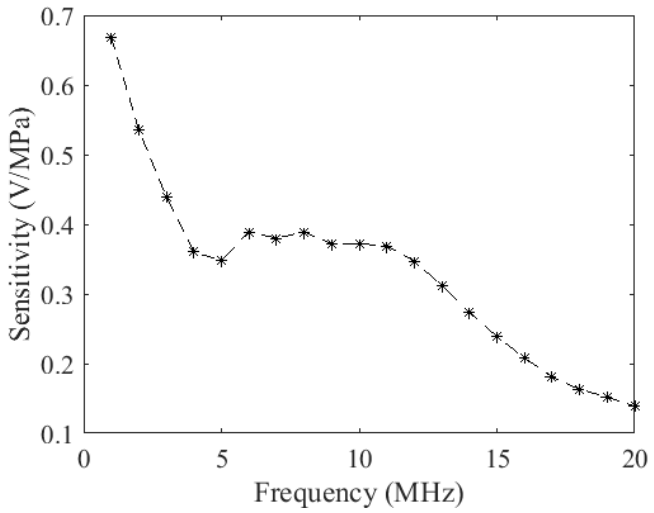

Figure 3.5: The frequency response profile of the hydrophone at integer values between 1 and 20 MHz (Taken from the calibration certificate).

The interpolated sensitivity function calculated and used for this analysis was:

$$M_H(\omega) = 5x10^{-5}\omega^4 - 0.0024\omega^3 + 0.037\omega^2 - 0.2287\omega + 0.8561 \quad (3.13)$$

where $M_H(\omega)$ was the sensitivity of the hydrophone (V/MPa) and ω was the frequency (MHz) [89].

3.2.2. Intrinsic Spectral Broadening

Quantification of the intrinsic spectral broadening (ISB) was carried out using a Doppler string phantom (model 043, CIRS, USA) pictured in Figure 3.6. The phantom consisted of a 20.71 L tank with an acoustically reflective string mounted on a 50 W motor with a velocity accuracy stated in the data sheet of ± 1% of stated speed. This phantom could be run at constant voltage to provide a constant velocity, a number of periodic test waveforms, or a number for pre-programmed physiological waveforms. The phantom tank was filled with deionised water and left to degas for 24 hours. The phantom was equipped with a corrective setting for use when imaging in water so the speed of sound did not need to be altered to minimise errors. The SuperLinear™ SL15-4 transducer (Supersonic Imagine, France) was placed in the tank at a known depth and at a 60° beam filament angle and clamped to ensure it could not move during testing. For each depth to be analysed, the phantom was set to a range of velocities and 5 measurements of the maximum and minimum velocities of the Doppler spectrum were recorded for each velocity setting. The full range of depths and velocities examined are given in Table 3.4.

Table 3.4: String Doppler phantom parameters for ISB measurements

Velocity (cm s^{-1})	10, 20, 30, 40, 50, 100, 150
Depth (cm)	1, 2, 3, 4

Figure 3.6: A CIRS string phantom consisting of a linear motor and a string with a strong acoustic response

In addition to quantifying the ISB, the ISB cancellation method proposed by Osmanski et al [1] was also investigated. The ISB cancellation method relies on discarding all but the peak velocity information for a single position in a blood vessel and averaging the peak velocities across a range of longitudinal positions in the vessel. As such, the method was more easily investigated using a flow phantom instead of a string phantom.

To facilitate this investigation a simple walled flow phantom connected to a magnetically driven Micropump shoe suction pump head (Michael Smith Engineering Ltd., UK), coupled to a DC servo motor (McLennan Servo Supplies Ltd., UK). The servo motor was driven by a servo amplifier (Aerotech Ltd., UK), receiving an analogue voltage input from a digital-to-analogue conversion (DAC) board. Using a computer, digital voltages were output to the DAC board from a programme developed in LabVIEW (National Instruments, USA) to have a constant flow velocity of 30 cm s^{-1}. The ultrasound

transducer was coupled to the phantom at a 60° beam vessel angle. 5 *UltraFast* insonations were carried out in the Aixplorer scanner research mode to allow for the in-phase quadrature data to be directly exported via USB. These data were analysed using custom code written in MATLAB (Mathworks, USA) to apply the method described by Osmanski et al. 5 longitudinal vessel positions were selected and gated to be at the equivalent radial positions to one another. The central frequencies from the corresponding Doppler spectra were then extracted and combined to produce a new spectrum.

3.2.3. Dynamic Range

In this experiment, the Doppler dynamic range (DDR) of the Aixplorer system was determined by varying the backscatter intensity of a range of blood mimicking fluids (BMFs) which were imaged using spectral Doppler in an ultrasound flow phantom. The phantom was an anatomically realistic walled renal artery flow phantom and the BMF used was an Orgasol® based solution, both were produced using the same methodology outlined in Chapter 4. The Orgasol® particles used were 5µm in size to match the diameter of red blood cells, the Orgasol® concentrations tested were 0%, 2%, 3%, 7.5%, and 10%.

The flow phantom was connected to the pump system as in the previous section. The pump system was connected to a reservoir containing the specific concentration of BMF, for each data point and formed a semi-enclosed pumping circuit. When changing BMF reservoirs, the pumping system was connected to a reservoir of deionised water as an intermediary to ensure the flow phantom was completely flushed of the previous BMF.

This experiment was carried out on the SuperLinear™ SL15-4 linear transducer, aligned at 60° to the vessel. The phantom was set up so that the vessel was at a depth of 7 cm from the transducer. For each concentration of BMF, images of the Doppler spectrum

were acquired at three different gain settings; 10%, 20%, and 30%. For each of these settings, 10 images were acquired, yielding 150 Doppler spectrum images.

When the data for this experiment were acquired, it was analysed using the *FIJI* distribution of ImageJ (Wayne Rasband, Public Domain - https://fiji.sc/). First the images were converted from DICOM format to PNG format. This allowed for more rapid batch processing of the data. For each concentration and gain setting a macro was set up to select a rectangular region of interest around the Doppler spectrum, avoiding any elements of the UI. The macro then calculated the integrated pixel intensity of the region of interest and saved the results to a text file.

This data was then loaded into MATLAB (Mathworks, USA) where a graph of integrated pixel intensity with respect to Orgasol® concentration could be generated. The Doppler dynamic range could then be calculated using the linear portion of this graph with Equation 3.10.

3.2.4. Transducer placement

Due to the curved geometry of the vessels produced for this study and described in detail in Chapter 4, acquiring a full velocity map of the entire vessel was not possible in a single insonation as parts of the vessel lay out of the plane of the ultrasound beam in any one transducer alignment. This meant that it was necessary to re-position the transducer to acquire separate velocity maps for the pre- and post-curvature regions of the vessel. This created a potential source of error due to misalignment of the transducer during repositioning which may have resulted in an incorrect velocity map due to a mismatch in insonation angle, or due to the beam subtending the incorrect plane of the vessel, i.e. not passing through the centre of the vessel.

The best approach for reducing this potential source of error was to use a rigorous procedure to ensure that the transducer was in as good an alignment as possible. Table 3.5 outlines a checklist of items which were optimised when positioning the transducer. The positioning was carried out in B-mode before switching to Doppler or research modes. Each parameter was optimised in sequence multiple times in increasingly finer detail until no further improvements could be made.

In order to test the reproducibility of this method a test of the values acquired using this method was carried out. A flow phantom featuring a curve was connected to the flow system with a steady flow of 30 cm s^{-1}. The transducer was positioned above the linear region of the vessel and its alignment was optimised based on the parameters in Table 3.5. A Doppler sonogram was generated for the centre of the vessel, the range gate size was 1.0 mm. 10 measurements of the peak velocity were recorded and the transducer was completely removed from the phantom. This process was repeated a total of 5 times in which 5 identical acquisitions were made for the curvature region of the vessel. The assumption that was made was that only the peak (centreline) velocity needed be taken for this evaluation as, if there was a transducer misalignment, the peak velocity would be always be reduced which made it a reliable metric for the accuracy of the alignment.

Table 3.5: Optimisation parameters for verifying the transducer alignment

Transducer angle	Ensure the transducer is vertical along its intermediate axis, apply a 60° insonation angle along the minor axis as normal
Transducer transverse position	The transducer should be moved back and forward perpendicular to the vessel until the vessel diameter at the image focus is greatest
Major axis angle	The transducer should be rotated clockwise and anticlockwise in its major axis until both sides of the vessel have similar brightness and diameters

These data were analysed using an analysis of variation (ANOVA) statistical test in MATLAB (Mathworks, USA) to determine if the populations of velocities were the same for each imaging region. The null hypothesis of this test was that the populations of velocities were identical. The alternative hypothesis was that the velocities varied between individual transducer alignments, indicating that repositioning the transducer was introducing errors to the velocity estimation.

3.3. Results

3.3.1. Measurement of Aixplorer pulse characteristics

A representative example of the frequency space spectra is presented in Figure 3.7 for the 5.6 MHz transmission frequency. For each spectrum, there was a main peak centred at the central transmission frequency of 5.6 MHz and, in some cases, additional peaks at 11.2 MHz and 16.8 MHz which corresponded to the first and second harmonics of the pulse, respectively. For each measurement, the peak frequency and bandwidth (taken as

the frequency with the largest amplitude and the full width half maximum of the main peak) were determined.

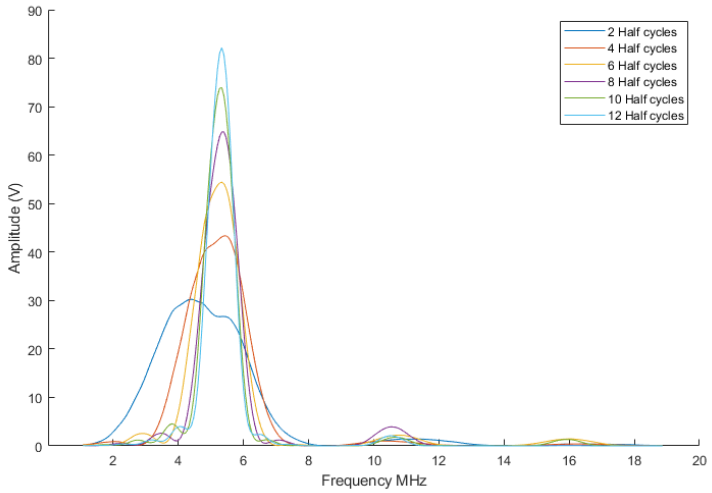

Figure 3.7: Representative spectra for central transmission frequency of 5.6 MHz for a range of transducer half cycle settings

The parameter which was of greatest concern for use in the multifrequency *UltraFast* Doppler spectral analysis (MFUDSA) algorithm was the pulse bandwidth. This was taken to be the FWHM and this parameter is presented graphically in Figure 3.8. The hydrophone data was also used to determine the peak positive and peak negative pressures of the pulses; this data is presented in Figure 3.9.

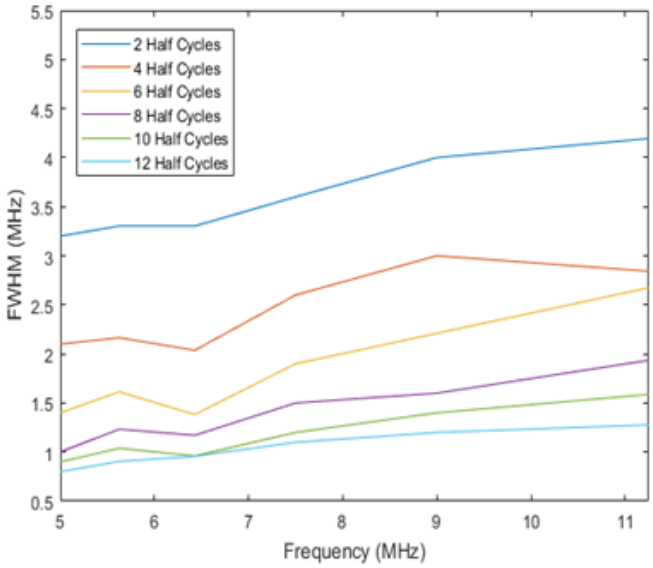

Figure 3.8: Bandwidth (FWHM) with respect to transmission frequency for varying pulse length settings

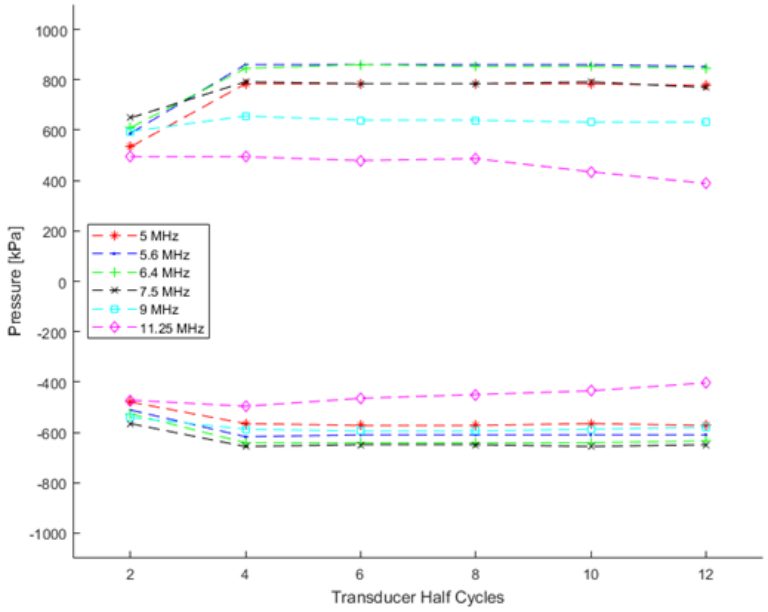

Figure 3.9: Peak positive and peak negative pressures as a function of transducer half cycles for a number of transmission frequencies.

The measurements of pulse bandwidth were used to compare the performance of the 2D Fourier analysis to the 1D Fourier analysis. Two ratios were calculated; the first, R_{SNR} was defined as the ratio of the 2D SNR to the 1D SNR. This ratio was plot with respect to pulse length in Figure 3.10; where it can be seen that this value was maximised for the lowest possible half cycle settings and appeared to trend downward with increasing half cycles. The second ratio, R_{FWHM}, was an examination of the velocity resolution (taken as the full width half maximum of the resulting Doppler spectrum for each technique) and was the ratio of the 1D FWHM to the 2D FWHM. This value is presented in Figure 3.11, it can be seen that it was maximised at 2 transducer half cycles. The error bars in Figure

3.10 and Figure 3.11 are representative of one standard deviation for each transducer half cycle setting.

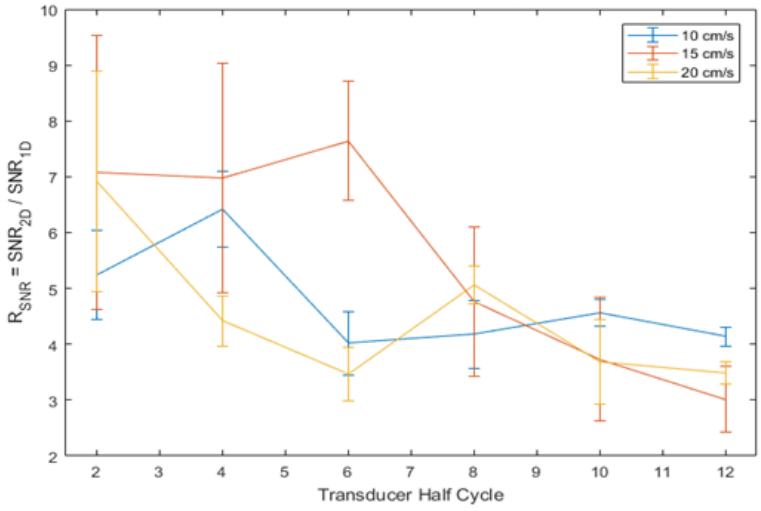

Figure 3.10: Variation of the ratio of 2D SNR to 1D SNR with respect to pulse length. The error bars correspond to one standard deviation.

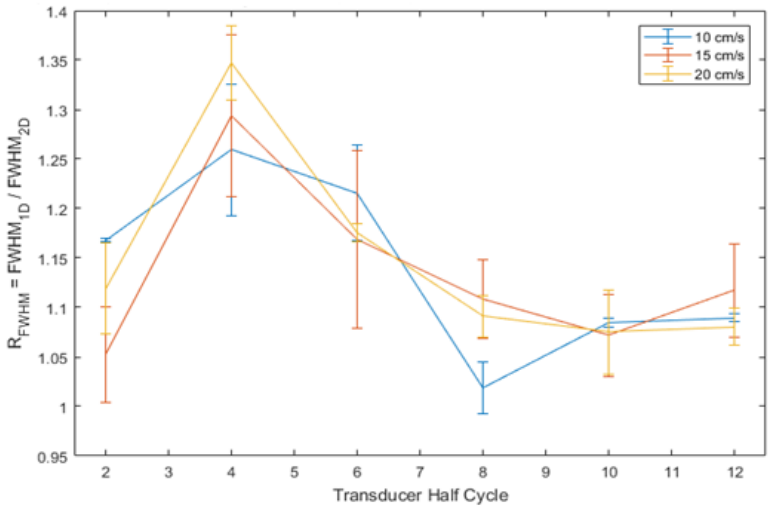

Figure 3.11: Variation of the ratio of 1D velocity resolution (FWHM) to 2D velocity resolution with respect to pulse length. The error bars correspond to one standard deviation.

3.3.2. Intrinsic Spectral Broadening

The intrinsic spectral broadening (ISB) measurements were analysed using MATLAB and a number of graphs were produced. An example of the variation of ISB with respect to velocity is given in Figure 3.12. The ISB follows a power law with respect to velocity with $R^2 = 0.97 – 0.99$ for each depth tested. The percentage ISB varied approximately in the range 4 – 10%. The variation of ISB with respect to depth was also investigated and a graph of the ISB with respect to depth is included in Figure 3.13.

To combine the ISB variance with respect to velocity and with respect to depth, a surface was fitted to the 3D data of ISB with respect to both velocity and depth. The surface is shown in Figure 3.14. This surface is defined by the following equation with an $R^2 = 0.96$:

$$f(V,d) = 447.4V^{-1.86} + 0.4203d + 1.754 \quad (3.14)$$

Where V was velocity in cm s^{-1} and d was depth in cm. This equation differed only slightly from the power law expressions which were calculated for the ISB with respect to velocity alone due to the ISB only having a very slight linear dependence on depth. In the curve the ISB varied approximately in the range of 2 – 10%. The advantage to utilising a surface fit like Equation 3.14 is that it can be easily coded into automated velocity estimators to simultaneously shift calculated velocities based on their magnitude while also using the vertical pixel index of the field of view combined with the resolution of the scanner to determine the depth of the velocity measurement and apply an additional correction.

In addition to quantifying the ISB for the SL15-4 transducer, the method proposed by Osmanski et al. [1] was tested to determine the feasibility of ISB cancellation for the same transducer. When the cancellation procedure was applied, the ISB measured for the flow phantom at a pump velocity of 30 cm s^{-1} was 0.46% which was a reduction of a factor of 6.5 ± 0.3.

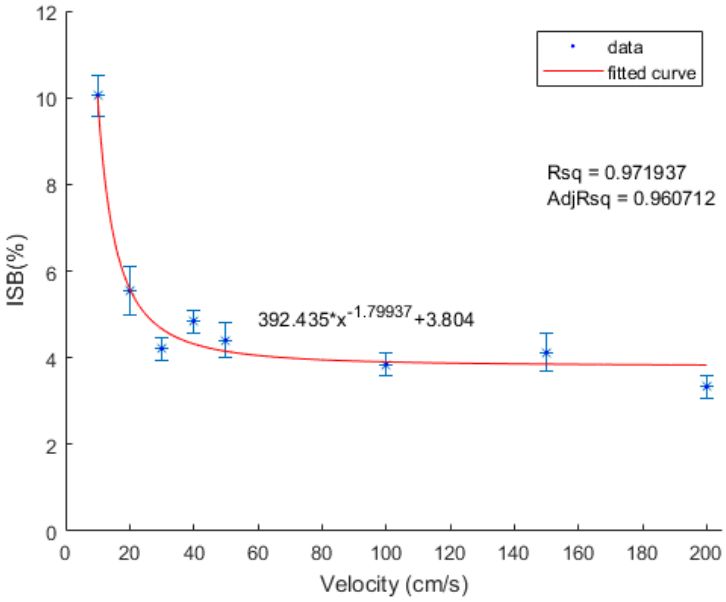

Figure 3.12: ISB with respect to velocity for a depth of 4 cm

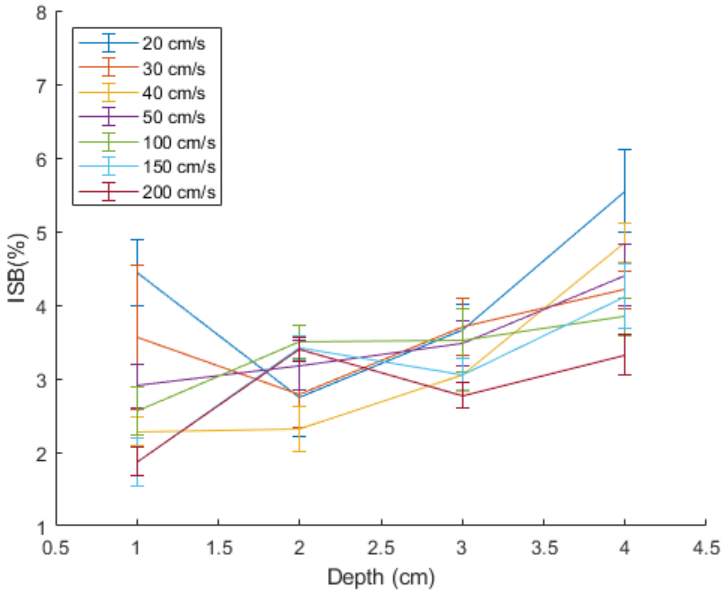

Figure 3.13: ISB with respect to depth for a number of velocities

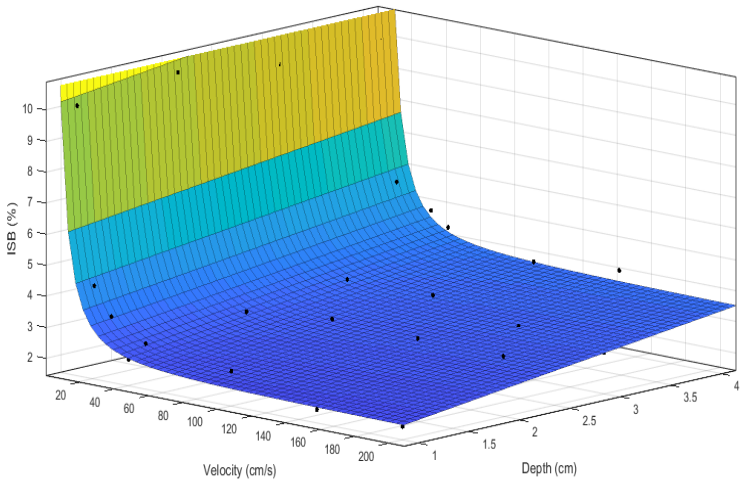

Figure 3.14: Interpolated surface for ISB with respect to velocity and depth

3.3.3. Dynamic Range

As the Orgasol® concentration increased in this experiment, the Doppler spectrum became increasingly illuminated to the point of saturation at the highest concentrations. The integrated pixel intensity values for each BMF concentration are illustrated in Figure 3.15. Using the linear region of this surface, the effective Doppler dynamic range was calculated as 16.7 ± 0.28 dB. The effect of varying the system gain was minimal as the ratios for each curve were largely unchanged with respect to gain setting.

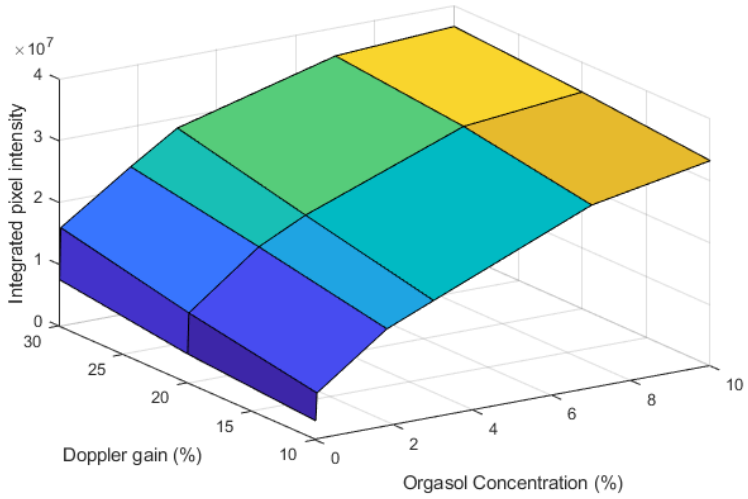

Figure 3.15: Integrated pixel intensity values with respect to BMFs of varying Orgasol® concentrations

3.3.4. Transducer Placement

The peak velocities recorded for a number of transducer positionings for the linear and curvature regions are presented in Figure 3.16 and Figure 3.17. For each region, an ANOVA test was carried out for the velocity populations to determine if there was a significant difference between the repositionings of the transducer. The results of this test

were p = 0.9789 and p = 0.3224 for the linear and curvature region, respectively. In both cases, the null hypothesis was accepted and the velocity populations were taken to be identical.

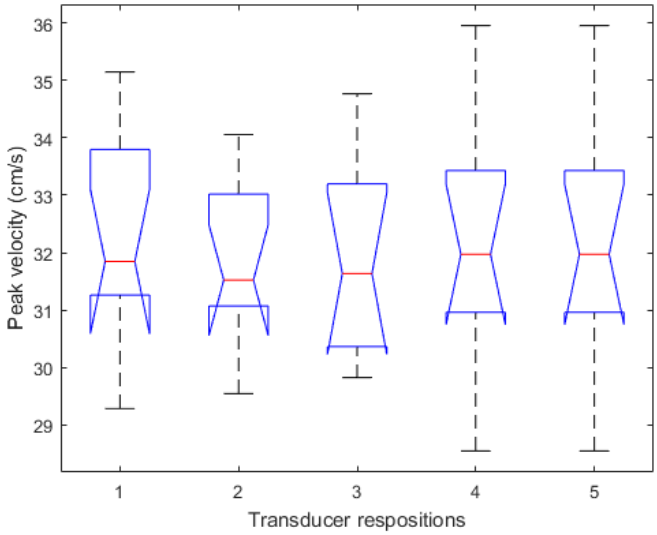

Figure 3.16: Box plot of the peak velocities recorded in the linear region of the vessel. The red lines represent the median velocity for each population, the notch represents the 60% confidence interval. The whiskers represent the 95% confidence interval.

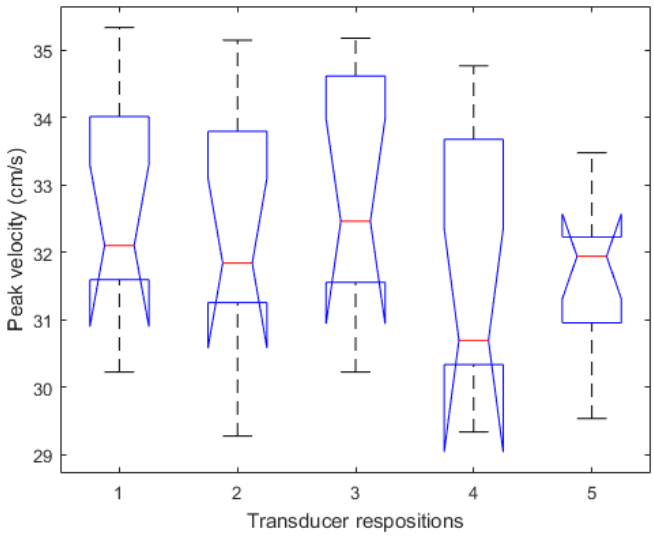

Figure 3.17: Box plot of the peak velocities recorded in the curvature region of the vessel. The red lines represent the median velocity for each population, the notch represents the 60% confidence interval. The whiskers represent the 95% confidence interval.

3.4. Discussion

3.4.1. Measurement of Aixplorer pulse characteristics

From the investigation into the pulse characteristics, it was found that the pulse bandwidth had a strong dependence on pulse length and frequency while the pulse pressure presented little variation with the same parameters. The relationship between pulse length and pulse bandwidth is a well-known corollary of the Heisenberg Uncertainty Principle which is true for all waves [90], this can be more easily understood by conflating the pulse length with time uncertainty and the frequency bandwidth with energy uncertainty. Similarly, the observed increased bandwidth with higher transmission frequencies was an effect of

the Heisenberg Uncertainty Principle, this could be seen by recalling the pulse length is measured in half cycles or one half of a wavelength; therefore for two pulses of different half cycle settings, the pulse with the higher transmission frequency would represent a shorter time interval due to its half cycles transmitting more rapidly. This effect results in shorter pulse lengths for higher frequency pulses of constant half cycles. With a view to maximising the effectiveness of the multifrequency Doppler, data were acquired to provide a comparison between 2D and 1D Fourier analysis of flow data. The results of this showed that, when using 2D Fourier analysis the SNR improved by a factor of 4 – 8 and the velocity resolution improved by a factor of 1.10 – 1.35. The SNR improvements were concentrated where the pulse length was shorter, with the shortest pulse setting (2 half cycles) showing the largest improvement for all velocities measured. The velocity resolution, however, showed the largest improvement for the second shortest pulse length. This is likely due to the increased interrogation of velocity information with respect to pulse length that is seen in PW Doppler [5]. This indicated that the best pulse length setting for use with 2D Fourier analysis was 4 half cycles as it maximised the gain in velocity resolution while the gain in SNR remained high.

The transmission frequency was also an important parameter for the 2D analysis. While the hydrophone results would suggest that a higher transmission frequency would be ideal due to the fact that it provides additional pulse bandwidth for the 2D analysis; in practice this was not an ideal insonation condition as it is well understood that ultrasound attenuation increases proportionally to transmission frequency, leading to a lower SNR overall. An additional, reason for the use of a lower transmission frequency was found in the literature relating to the frequency-based attenuation of the ultrasound pulse intensity. Evans & McDicken [5] have reviewed several models presented for the effect of frequency-dependent ultrasound attenuation and scattering. The researchers stated that

the relative shift in the central frequency of an ultrasonic pulse was proportional to the error in velocity estimation of pulsed wave Doppler systems. It was therefore important to quantify this effect. The shift in central frequency was modelled for scattering and attenuation according to the following equations:

$$\%\Delta f_{c(SCAT)} \approx \left[\left\{1 + \frac{1}{N^2}\frac{1}{\ln(2)}\right\}^{1/2} - 1\right] \tag{3.15}$$

$$\%\Delta f_{c(ATTEN)} \approx \frac{4.14\alpha_0 Z f_c}{N^2} \tag{3.16}$$

Where $\%\Delta f_{c(SCAT)}$ is the percentage increase in transmission frequency due to Rayleigh scattering from blood, $\%\Delta f_{c(ATTEN)}$ is the percentage change in transmission frequency due to frequency-dependent attenuation, N is the number of pulse cycles, α_0 is the attenuation coefficient (measured in dB cm^{-1} MHz^{-1}), Z is the depth (in cm), and f_c is the central transmission frequency (in MHz). Evans & McDicken combined these two models and presented a graph of the combination which is reproduced here in Figure 3.18. In Figure 3.18 the percentage change in central frequency is examined with respect to the number of half cycles for a number of values of K = $\alpha_0 Z f_c$, or the product of the attenuation coefficient, the depth, and the central transmission frequency. For low values of K, Rayleigh scattering dominated and the received central frequency was increased at low numbers of pulse cycles, and for high values of K, attenuation dominates, leading to a decrease in the received central frequency. As established previously, the best pulse length setting for the multifrequency system was at 4 half cycles or 8 pulse cycles using the same convention as Evans & McDicken. It can be seen in Figure 3.18 that for 8 pulse cycles, the effect of scattering is negligible and higher K values had a greater effect on the central frequency shift and, therefore, the accuracy of the velocity estimation. Of the

values affecting K, attenuation coefficient and depth could not be changed *in vivo*, therefore lowering the value of K by utilising a lower transmission frequency was selected as the best option to limit any errors in velocity estimation.

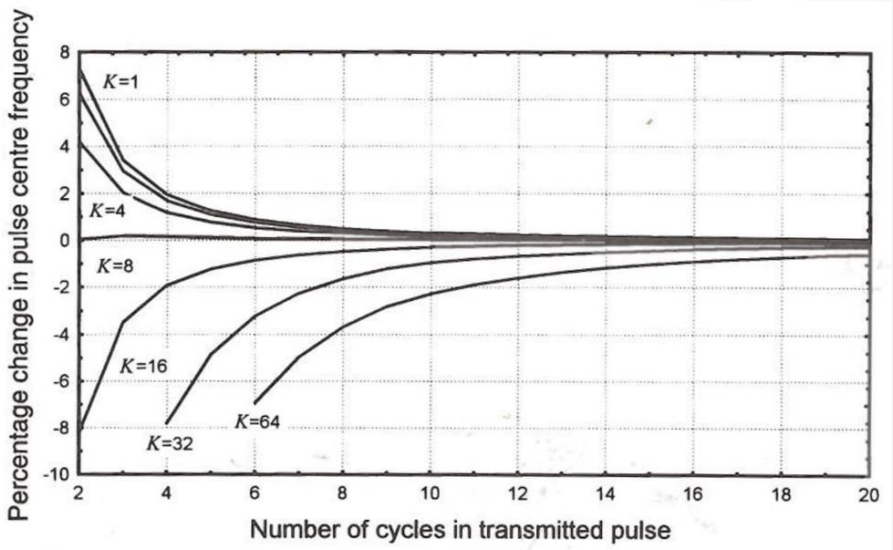

Figure 3.18: Percentage change in central transmission frequency of an ultrasonic pulse due to scattering and attenuation with respect to number of pulse cycles for varying values of K (the product of attenuation coefficient, range, and pulse central frequency) – adapted from Evans & McDicken [3]**.**

The investigation into pulse characteristics also provided information on the acoustic pressure exerted by an *UltraFast* acquisition on the Aixplorer. The magnitude of the highest pressure recorded was 806.59 kPa, however it was important to note that the acoustic characteristics of the microbubble contrast agents are only stable up to certain pressures. In the case of the SonoVue contrast agent, this maximum pressure above which changes to bubble characteristics are observed is 150 kPa, and bubble destruction occurs at pressures exceeding 300 kPa [74]. This means that to avoid microbubble destruction,

when using *UltraFast* acquisitions, the acoustic power must be set to a minimum of -4.29 dB and to avoid changes to bubble characteristics the acoustic power must be set to a minimum of -7.31 dB.

3.4.2. Intrinsic Spectral Broadening

The ISB was evaluated for a range of velocities and depths and was found to have a linear dependence with respect to depth and a power law dependence with respect to velocity. The relation between each of these parameters was fitted to a surface and the equation of that surface was given in Equation 3.14. In these measurements, the ISB of the Aixplorer system varied in the range 2 – 10%. This was a considerable improvement over previous studies where the ISB is typically in the range of 20 – 30% [85,91–93]. Some examples in the literature of considerably lower ISBs are available, such as the study carried out by Walker et al. [94] on three cardiac systems which reported one scanner with a consistent velocity overestimation of 5% and two scanners with velocities recorded within expectations. This suggests that the results for the Aixplorer or not atypical and may just be an indication of particularly good engineering and calibration. Looking at previous examinations of ISB with respect to velocity, it can be seen that there was not typically a reported dependence of ISB on velocity for velocities above 50 cm s^{-1} [85,91]. This is largely in line with what was observed in this work for higher velocities while the power law dependency was largely only detected for velocities <40 cm s^{-1}. It is believed that the dramatic observed increase in ISB below this velocity threshold is not a product of the system itself but, instead, a product of the limited cursor velocity resolution at very low velocities leading to an overestimation. Furthermore, the highest values of ISB were recorded for the lowest velocities examined and represent velocity errors on the order of ± 1 cm s^{-1} which is smaller than the measured velocity resolution for the Aixplorer system.

Previous studies into the effect of depth on ISB have concluded that it has no or a negligible effect on ISB [85,95] while the results of this work indicate a weak linear dependence on depth. When taking a cursory glance at these results, they seem very unintuitive. As ISB is a geometric effect, dependent on the difference in insonation angles between transducer elements, the logical consequence of increasing depth should be a linear reduction in ISB but this is not observed. A potential explanation for this effect was described by Hoskins et al. [96] where it was established that different manufacturers of ultrasound scanners have specified a wide variety of Doppler aperture sizes and that as depth increases, the Doppler aperture also increases. This would explain the observed trend of constant ISB with respect to depth and even the results of this study detecting a slight linear increase in ISB with respect to depth as the increasing aperture size would compensate for the geometric decrease in ISB that should be observed with depth. It stands to reason, therefore, that should the gate depth become large enough that the entire transducer array is utilised for the Doppler aperture, then increasing depth beyond that point would be correlated with a decrease in ISB, however, this threshold depth may be so deep as to cause aliasing in all but the slowest velocities meaning it is likely not of practical concern.

One parameter that wasn't investigated in this work that has a demonstrable effect on ISB was Doppler gain. Steinman et al. [95] showed that as Doppler gain was increased, there was a proportional increase in ISB, with the largest ISB associated with Doppler spectrum saturation. This would firstly indicate that Doppler gain should be minimised in quantitative studies to increase accuracy but, additionally, it would be worth considering in future studies utilising ultrasound contrast agents as the increase in SNR may come with the trade-off of decreased velocity accuracy.

A study which investigated in detail the effect of contrast agents on velocity accuracy was Browne et al. [97] which investigated specifically the peak velocity measurements and the ratio of the peak velocity in a stenotic region to the peak velocity in a pre-stenotic region. This study showed that the application of contrast agents in Doppler ultrasound resulted in an increase in the measured peak velocity, thought to be due to the preferential attenuation of higher Doppler shift frequencies and representative of real velocities which heretofore had gone unrecorded. This study concluded that the application of contrast agents is, therefore, an essential step in acquiring the most accurate patient data. This conclusion, combined with that of Steinman et al. indicated that while contrast agents increase the value of ISB, they provide an increasingly important role in diagnosis, particularly when attenuation is high such as in obese patients. Therefore, there is a significant interest in the development of methods which can be used to minimise the ISB.

The ISB cancellation method proposed by Osmanski et al. [1] was evaluated and it was found to reduce the ISB of the transducer by a factor of 6.5 ± 0.3. This is comparable to the results of Osmanski et al. which achieved ISB reductions of a factor of 7 ± 4 *in vitro* and 4.6 ± 0.9 *in vivo*. This result showed that for *UltraFast* acquisitions, the effect of ISB can be reduced to the point of being negligible [1]. This was an important result as it indicated a potential avenue for the free application of contrast agents without incurring negative effects on the velocity accuracy. Consequently, this technique was incorporated to the MFUDSA algorithm and used for all further velocity analysis when imaging in *UltraFast* mode.

3.4.3. Dynamic Range

The results of this study into the effective Doppler Dynamic range of the Aixplorer system were a DDR of 16.7 ± 0.28 dB. This represents approximately 2/3 of the possible pixel

intensities of a bit-depth of 8 that is present in most scanners. It has been stated that to allow for the simultaneous display of, for example, the liver tissue interface and blood in the same image, a dynamic range of 100 dB is required [3]. In principle, this is not achievable on an 8 bit intensity display but would in principle be achievable for a 16 bit display (65536 pixel intensity values). In order to capture the full range of echoes within the confines of an 8 bit display, most ultrasound scanners utilise compression algorithms in the form of non-linear amplifiers [3,5]. The results of this study indicate that for the Aixplorer system, under its current compression architecture, there is approximately 7 bits or 128 pixel intensity values available for displaying continuous Doppler intensities. This result was important for the application of microbubble contrast agents as a relatively small concentration of microbubbles could result in complete saturation of the Doppler spectrum.

3.4.4. Transducer Placement

There was no significant difference between the velocities recorded for different transducer positionings for either the linear or curvature regions within the vessel. Although, with $p = 0.3224$, the results for the curvature region indicated a possible introduction of error. This is likely due to the relative short absolute length of this region, approximately 2 cm compared to the 5 cm of the linear region, which may have increased the difficulty of properly aligning the transducer. Another potential source of error for this was that, although care was taken to ensure the vessel was at the transducer focus, there may have been effects due to variation in the slice thickness that would increase errors in the velocity assessment due to the partial volume effect. Overall, these results were taken to mean that the contribution of repositioning the transducer had a negligible effect on the systemic errors for the flow experiments.

3.5. Conclusion

The purpose of this chapter was to examine some key parameters for the calibration and optimisation of future experiments. The pulse characteristics were evaluated using a hydrophone to determine the ideal transmission settings to use in 2D Fourier analysis. It was found that the pulse bandwidth had an inverse relationship with pulse length and a positive dependence on transmission frequency. Further analysis into the effect of transmission parameters on SNR and velocity resolution indicated that the ideal pulse length was 4 half cycles to maximise the velocity resolution while maintaining a high SNR. While the ideal transmission frequency was as high enough to provide an increased pulse bandwidth but low enough that attenuation of the signal didn't degrade the SNR. The transmission parameters used for all further experiments were a transmission frequency of 5.6 MHz with a pulse length of 4 half cycles.

The intrinsic spectral broadening was measured for the transducer which was used for all the experiments in this work (SL15-4 linear) and a calibration surface was generated for the ISB with respect to depth and velocity. Using the equation of this surface, the code used for analysis could be modified to automatically apply a correction factor to the Doppler spectrum to shift velocities to their "true" value as measured from the string phantom. This correction factor was applied to all further non-research mode acquisitions in this work. The method proposed by Osmanski et al. to allow for cancellation of the ISB entirely when using *UltraFast* acquisitions was also evaluated and it was found to provide a 6.5 ± 0.3 factor reduction in ISB. This method was effectively capable of cancelling the ISB, however it could only be utilised for *UltraFast* acquisitions which took place in the Aixplorer research mode because it required the raw data for the analysis. This method was utilised on all further research mode *UltraFast* acquisitions in this work.

The effect of the transducer repositioning was evaluated and found to not have a significant bearing on the systemic errors in velocity. In all further flow experiments, the protocol outlined in this chapter for positioning the transducer was followed to prevent the introduction of uncertainties.

This chapter has outlined the procedures undertaken to calibrate and characterise the systems used in this work to ensure that the data they provide is accurate, precise, and understood in the context of the capabilities and limitations of the hardware used. This is an important, albeit often overlooked, aspect of medical and scientific measurements which provides crucial understanding and traceability for the methodology used elsewhere in this work. The pulse characteristics of the Aixplorer SL15-4 transducer were of vital importance to the analysis undertaken in Chapter 4, which relied heavily on the bandwidth of the transmitted pulses in its calculations. The intrinsic spectral broadening was an important consideration for both the analysis in Chapter 4 and the experiments in Chapter 5 as it was fundamental to ensuring that the correct velocities were calculated by the post-processing algorithms as well as correcting for the velocities displayed by the scanner itself. The Doppler dynamic range of the Aixplorer system is an often unexplored quantity in the literature, and this work provided a clear understanding of exactly what the limits of the system are, this was important to ensure that the spectrum was always appropriately concentrated without saturation for the best possible velocity estimation. Finally, it was important to ensure that the repositioning of the transducer between acquisitions was carried out with as little disruption to the accuracy of the results as possible, and a protocol was established for all future acquisitions to enable this.

Chapter 4: Phantom Production

The contents of this chapter have been accepted, in edited form, for publication in Physica Medica pending peer review.

4.1. Introduction

This chapter outlines a procedure for the manufacture of a renal artery flow phantom for use in Doppler ultrasound. Many phantom designs have been tested for use in Doppler flow experiments, as discussed previously, however these designs have not been able to create a simulation of the progression of atherosclerosis and, to date, there exists a need for a robust and reproducible design for a phantom testbed which can accurately display the progression of arterial disease. The motivation behind this work is to outline a protocol which can produce a series of geometrically identical walled flow phantoms which display varying levels of wall stiffness as an indication of early stage atherosclerosis. This phantom production procedure used a poly-vinyl alcohol (PVA) based vessel mimicking material (VMM) and used an agar-based tissue mimicking material (TMM) to surround the vessel, the materials were selected for production due to their highly tuneable acoustic properties to appropriately mimic the situation *in vivo* while also, in the case of PVA-c, having the property of variable Young's modulus.

PVA is a synthetic polymer made through the hydrolysis of polyvinyl acetate. PVA has been widely utilised as a component in the production of medical phantoms due to the fact that its mechanical properties can be precisely controlled through physical and chemical cross-linking processes. The most commonly used method to initiate cross-linking is the application of sequential freeze-thaw cycles to aqueous PVA solutions [56,98–101]. When PVA is placed in an aqueous solution and exposed to freeze thaw cycles, a polymerisation takes place which results in an increase in material stiffness; the material formed by this procedure is a cryogel known as poly-vinyl alcohol cryogel

(PVA-c). PVA-c has been widely used as a tissue mimicking material (TMM) for ultrasound and MR imaging [100] and its strength and robustness allow for its use in flow phantoms as a vessel mimicking material (VMM) [98]. The physical properties of PVA-c are largely determined by the initial degree of hydrolysis of the PVA, typically varying from 80% to greater than 99% hydrolysed [102]. In this work the formulation of PVA used was 99%, which allowed for a high degree of polymer crosslinking.

There have been several studies into the mechanical properties of PVA-c [56,57,98,100,103]. Some examples from the literature are included in Table 4.1. It can be seen from this table that accurate mimicking of vessel mechanical characteristics has been shown to be possible with relatively low concentrations of PVA-c. It has been noted in the literature that one of the most important factors in the degree of cross-linking in PVA-c is the rate at which the thaw takes place during free-thaw cycles [57,100]. This would imply that sample volume is also an important factor which may affect the mechanical properties, since the thaw rate is dependent on parameters such as sample material, surface area and the involved heat transfer kinetics [57,100].

Two standards for evaluating the mechanical properties of viscoelastic solids are International Organisation for Standardisation (ISO) no. 7743 and no. 37. ISO 7743 [104] specifies that a cylindrical test sample of typical height 12.5 ± 5 mm and diameter 29 ± 0.5 mm is subjected to 5 compression cycles, with a compression speed no greater than 50 mm min^{-1} until a strain of 30% is reached. The Young's modulus can then be calculated from the linear region of a stress strain curve generated using the 5^{th} compression cycle. ISO 37 [105] provides a procedure for tensile mechanical testing, where the test object used is dumbbell shaped with a testing region between the flanges of typical thickness 3.0 ± 0.2 mm, length of 25 ± 0.5 cm, 20 ± 0.5 cm, or 10 ± 0.5 cm, and a width of 6.0 ± 0.5 mm.

Therefore, given the dependence on thaw rate on sample geometry, this raises the question as to whether using a relatively large compression test sample, such as those in ISO 7743 [104], is a valid comparison to what would be relatively small vessel mimicking samples of different geometry. As such, ISO 37 may allow for a more accurate estimation of the mechanical properties of the vessels, given the similarities in size. One parameter which is of use in this area is the sample area to volume ratio (SA:V)), a large SA:V indicates that a material will more rapidly approach a homogenous internal temperature uniform to its surroundings. Taking the dimensions of the cylindrical and dumbbell samples, the SA:Vs can be calculated as 298 m^{-1} and 1000 m^{-1} respectively, indicating that the dumbbell samples have a significantly higher ability to reach homogenous temperatures relative to their surroundings than the cylindrical samples. This presented the opportunity to introduce a method which would allow for an increased degree of certainty in the mechanical properties of PVA-c as heretofore no evidence has been presented in the literature of a direct comparison between the elastic properties of the test sample geometries and the geometries of the vasculature being mimicked. This elevated the protocol described in this chapter to novelty as it will have a significantly improved certainty that the phantoms are accurately mimicking the situation *in vivo*.

***Table 4.1: Young's elastic modulus values given for various forms of PVA-c as compared to values of tissue* in vivo.**

Healthy vessel (kPa)	Diseased vessel (kPa)	Freeze thaw cycles	PVA-c (5% w/v) (kPa)	PVA-c (10% w/v) (kPa)		PVA-c (15% w/v) (kPa)
5 – 83	116 – 751	1	2.5 ± 0.09*	24 ± 0.42¶	19 ± 2†	190‡
		2	2.7 ± 0.09*	70 ± 1.80¶	80 ± 16†	346‡
		3	3.5 ± 0.1*	87 ± 1.85¶	102 ± 12†	
		4	5.4 ± 0.12*	115 ± 6.63¶	136 ± 26†	
		5		135 ± 9.81¶	160 ± 42†	1840‡
		6			164 ± 34†	

* [57]

¶ [103]

† [56]

‡ [98]

As previously discussed, there has been disagreement as to the true stiffness values of arteries, in the literature [61]. When measured using indentation techniques, such as those utilising the tip of an atomic force microscope, the values recorded for veins and arteries spanned the range of 6.5 – 560 kPa. However, the same tissues were recorded in the range of 600 – 3500 kPa when using tensile mechanical measurements. It has been theorised that this discrepancy is due to the retention of large quantities of water in excised tissue which, due to its incompressibility, results in a large increase in Young's modulus for

measurements over long length scales [61]. Therefore, it can be assumed that, for the purposes of flow experiments where small length scales dominate, the stiffness values of vessels determined using nanoindentation techniques should be taken as the ground truth. With this assumption, the range of vessel stiffness values can be achieved using 10% w/v and 15% w/v PVA-c formulations for reasonably low numbers of freeze thaw cycles, as indicated in Table 4.1.

The purpose of this chapter was firstly, to provide a description of the methods used for the production of tuneable PVA-c vessel and the corresponding flow phantoms. Secondly, the aim was to develop test procedures which incorporate industry test standards, utilising these methods to characterise the mimicking properties of the materials used in the production of these flow phantoms. This chapter provides the basis for the entire work of this thesis as it allows for the development of a reliable testbed that closely mimics the ground truth of the *in vivo* situation.

4.2. Materials and Methods

4.2.1. PVA-c vessel mimic production

The ingredients used in the production of the PVA-c VMM are outlined in Table 4.2. When the PVA-c constituents were being developed, the guidelines for the production of agar TMM were used as a basis [106,107]. However, the use of silicon carbide particles as attenuators was challenging in PVA-c production. The gelling temperature of agar was found to be approximately between 35 – 40° C which allowed for the material to become significantly more viscous before reaching room temperature, this is unlike PVA-c which doesn't begin to solidify until it has been in the freeze stage of the initial freeze thaw cycle for approximately 30 minutes at -30°C. This means that heavy particles, such as silicon carbide tended to settle out of solution before the material could solidify. It was decided

that using high density particles for the purposes of providing scatter and attenuation characteristics would be too challenging and so a liquid silicone emulsion was used in this production in addition to lower density aluminium oxide particles which did not present a sedimentation problem.

Commented [AM14]: Updated based on Kumar's comment

Two batches of PVA-c were made: a 10% w/v formulation and a 15% w/v formulation. The 15% w/v formulation differed only in the percentage of PVA-c (increased 5%) and deionised water (decreased 5%). The components used were selected to provide acoustic properties analogous to human arteries. Two sizes of aluminium oxide particles were included to act as acoustic scatterers and provide speckle in the ultrasound images. A custom 30% emulsion of silicone particles ranging in particle sizes 0.2 – 0.5µm was used as an attenuator and to provide appropriate scattering properties. Benzalkonium chloride was used as an anti-fungal agent to preserve the vessels, and glycerol was used as a plasticiser to fine tune the speed of the sound of the material.

Table 4.2: Constituent materials and concentrations used in the production of 10% w/v PVA-c VMM

Component	%(W/V)	Mass per 1L (g)
PVAc	10.00	100.0
Aluminium oxide (0.3µm)	0.73	7.3
Aluminium oxide (3µm)	0.72	7.2
Silicone Emulsion	1.50	15.0
Benzalkonium chloride	0.46	4.6
Glycerol	5.00	50.0
Deionised water	81.59	815.9

The components were placed in a metallic beaker and the total mass of the mixture was recorded. The beaker was then placed in a water bath at 90°C and continually mixed. The temperature of the material was monitored and once it had reached 90°C it was allowed to mix thoroughly at 100 rpm for 1 hour. The beaker was then removed from the water bath and the mass of the mixture was measured again, any difference is mass was rectified by adding deionised water to replace that lost by evaporation. The mixture was then placed in an ice bath and mixed continuously until it had cooled to 5°C. The purpose of this cooling step is to ensure that the particles in the mixture remain in suspension when the material undergoes its first freeze thaw cycle and to avoid sedimentation over a long freeze. Once the material was at 5°C, it was syringed into the interstitial space of the two part vessel mould and the moulds were placed into the freezer. At the same time, a number of smaller cylindrical and dumbbell samples were produced by pouring some of the batch directly into casting moulds which were also placed into the freezer. These samples were produced in line with ISO 7743 and ISO 37 and had the following dimensions. The cylinder samples had a height of 18 ± 0.5 mm and diameter of 30 ± 0.5 mm. The cuboid test section of the dumbbell samples had a width of 10 ± 0.5 mm, a depth of 2.5 ± 0.5 mm and an effective test length of 15 ± 0.05 cm. These dimensions gave SA:Vs of 244.444 ± 0.007 m^{-1} for the cylindrical samples and 1000 ± 0.125 m^{-1} for the dumbbell samples.

It is well established in the literature that the most important aspect of the freeze thaw cycle is the thawing section, specifically duration of the thawing section [102]. It was therefore important to ensure a consistent, homogeneous thaw for all samples. This was achieved by placing the samples in an insulated freezer with the door closed. At the conclusion of each freeze cycle, the power to the freezer was disconnected. This allowed for the samples to transition from -30°C to thermal equilibrium with room temperature 22°C over a period of 24 hours thereby, prolonging the thaw portion of the cycle and thus

inducing more cross-linking. A single freeze thaw cycle lasted 40 hours, consisting of a 16 hour overnight freeze at -30°C followed by a 24 hour thaw to room temperature. Completed samples could be used immediately after freeze thaw cycling or stored in a water-glycerol solution to prevent dehydration, a method which has been shown to be effective at maintaining the shelf life of PVA-c for up to 2 years [108].

4.2.2. Agar tissue mimic production

The tissue mimicking material was made in accordance with guidelines put forward by the International Electrotechnical Commission (IEC) [106,107]. The ingredients used in the production of the Agar TMM are outlined in Table 4.3. The purpose of each material is the same as in the production of PVA-c VMM, with the exception that silicon carbide is used instead of silicone emulsion as an attenuator. The reason for this is that agar TMM sets at room temperature and much more rapidly than PVA-c, so the relatively large silicon carbide particles are less likely to settle out of the mixture before the material has completely set, which is a much larger problem in the production of PVA-c.

Table 4.3: Constituent materials and concentrations used in the production of 3% w/v Agar TMM

Component	%(W/V)	Mass per 1L (g)
Agar	3.00	30.0
Aluminium Oxide (0.3 µm)	0.88	8.0
Aluminium Oxide (3 µm)	0.94	9.4
Silicon Carbide	0.53	5.3
Benzalkonium chloride	0.46	4.6
Glycerol	11.21	112.1
Deionised Water	82.97	829.7

The ingredients were weighed out using a precision mass balance (model: PGW 1502e, Adam Equipment, UK). The components were placed in a metallic beaker and transferred to a water bath at 90°C. The mixture was mixed continuously and temperature was monitored. Once the mixture had reached 90°C it was allowed to mix thoroughly at 100 rpm for 1 hour. The beaker was then removed from the water bath and allowed to continue mixing at room temperature while its temperature was monitored. The gelling temperature for agar TMM is at approximately 35°C, so the mixture was allowed to cool to approximately 45°C before pouring. This was to allow for ease of pouring with a relatively non-viscous mixture while limiting the duration the material would spend being unmixed before setting in order to prevent sedimentation. The agar TMM was poured into the completed phantom as well as cylindrical acoustic testing samples. The material would fully set after an hour and the phantom would be top with a layer of water-glycerol solution. The acoustic samples were also stored in water-glycerol solution.

4.2.3. Geometric Fabrication

A 3D model of the renal artery was previously developed for use in constructing flow phantoms which was also utilised in this work [109]. This model was based on CT data from a healthy volunteer from whom informed consent was gathered and the analysis was given ethical approval. These data were used to produce a number of additional renal artery models in the production of the vessel mimicking material. The various renal models used in this work are included in Figure 4.1 and the procedure for the production is included in Figure 4.2. The original model was adapted by reducing its diameter by 3 mm and a 20 mm diameter cylindrical section was added 10 mm distal from the vessel curvature. The purpose of these adaptions was to allow for a 1.5 mm vessel wall in the final vessel and to allow for the insertion of specially designed modular inserts which can

Commented [AM15]: Added based on Kumar's comment

finely control the vessel diameter, thus controlling the degree of stenosis in the final VMM. Using the adapted renal model, a silicone master mould was produced which would allow for the casting of inverse vessel moulds. A low melting point alloy (LMA) with a melting point of 47 °C (MCP 47, Mining and Chemical Products Ltd., Northamptonshire, UK) was cast in the silicone master moulds to produce a series of inverse vessel moulds. Using the original renal artery model, a number of outer vessel silicone moulds were constructed featuring a diameter of 10.6 mm. By placing the LMA inverse mould inside the outer vessel mould, a negative space is left to form the vessel with a wall thickness of 1.5 mm.

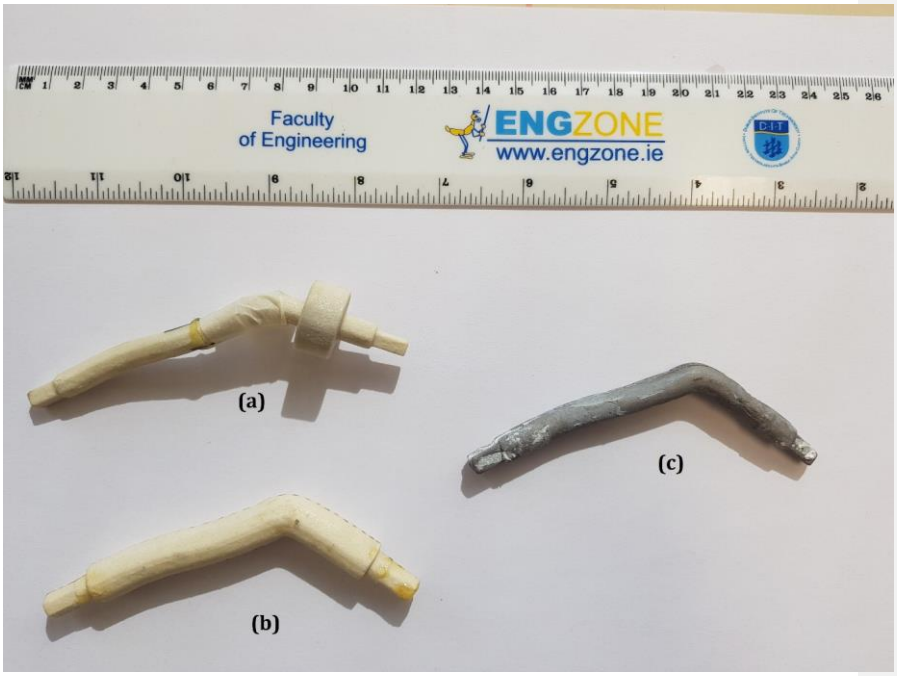

Figure 4.1: (a) Rapid prototyped model of renal artery based on CT data from a healthy volunteer. The diameter of this model was reduced by 3 mm to allow for a 1.5 mm vessel wall. This model also featured a 20mm diameter cylindrical section 10 mm distal from the curvature. The purpose of this feature was to allow for different modular inserts to be placed in the silicone master mould to precisely control the degree of stenosis in the LMA inverse mould. (b) Rapid prototyped model of the renal artery based on CT data from a healthy volunteer. This model was not altered from the CT data. (c) LMA inverse mould produced using the silicone master mould. This model did not feature a stenosis.

4.2.4. Vessel Production and Implantation

Once the LMA inverse mould was in place, the PVA-c VMM was syringed into the outer vessel mould and the entire mould was clamped and placed in a freezer at -30 ± 0.5 °C to

undergo freeze thaw cycling. Once the required number of cycles was complete, the vessel was removed and prepared for implantation.

Implantation preparation consisted of removing any excess PVA-c material that had overflowed inside the mould and cleaning the ends of the LMA inverse mould to ensure the ends of the vessel were clean and unobstructed. The vessel was then coupled to PVC tubing with an internal diameter of 7mm. The vessel and tubing were then placed in a sealable plastic container (HPL 818, Lock & Lock, USA) with dimensions of 20.5cm x 13.4cm x 12.0cm. The entry points for the tubing consisted of 8mm bore holes on adjacent sides of the container to facilitate the vessel curvature. These entry points were lined with 20 ppi sponge FT-T20, Foam Techniques ltd, Northamptonshire, UK) and secured with silicone sealant (DY1002, 151 Products Ltd., UK) to reduce leakages. At this point the phantom was tested for water tightness by filling it with water and leaving it for several hours; if there were no leaks, production was able to proceed. Rubber was layered on the bottom of the phantom to reduce strong acoustic reflections from the base of the phantom. The container was then filled with the agar based TMM, which was allowed to set completely.

The entire phantom was then placed in a water bath at 60°C for approximately 4 hours. This completely melted the LMA inverse mould inside the phantom which was removed and collected to allow for it to be recycled in future phantom production. Once the LMA had been removed, the tubing and vessel were filled with a water glycerol solution, and a layer of this solution was also poured on the top of the phantom. When not in use, the phantoms were all stored under these conditions to prevent dehydration and increase shelf life.

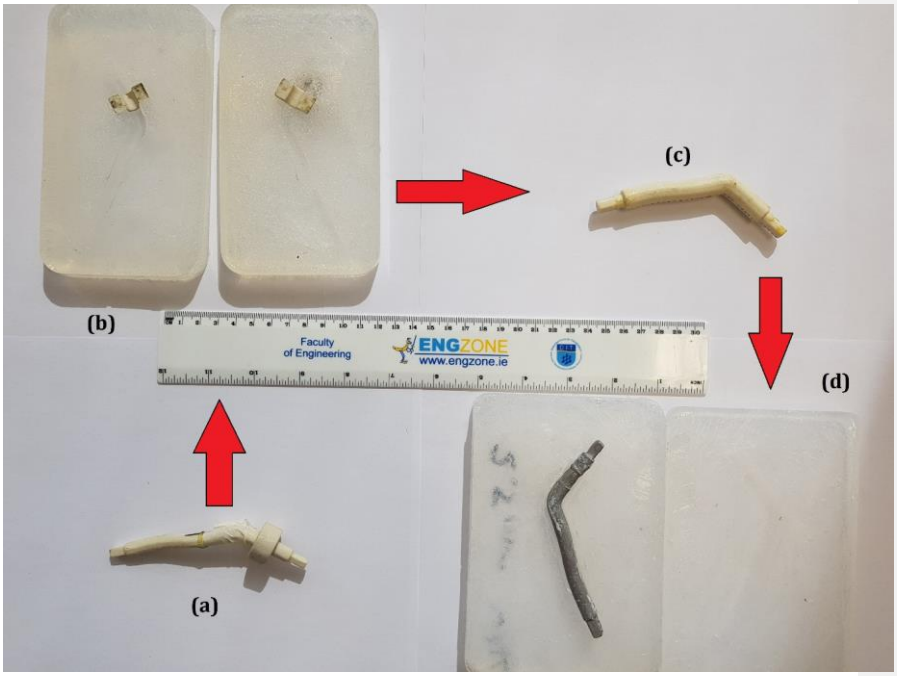

Figure 4.2: (a) Rapid prototyped model of renal artery from CT data of a healthy volunteer. (b) Silicone master mould produced using renal artery model. (c) Low melting alloy inverse mould of renal artery produced from silicone master mould. (d) Vessel mould with inverse mould in place. The vessel mould has an internal diameter 3mm greater than the inverse mould, giving a vessel wall thickness of 1.5 mm.

Figure 4.3: Lumen moulds made of low melting alloy. The vessel mimicking material was moulded around these inserts to produce an anatomically realistic vessel lumen. The low melting alloy could be removed later by placing the phantom in a water bath at 60°C.

4.2.5. Material Characterisation

4.2.5.1. Acoustic characterisation

An important step in ensuring that tissue mimicking materials are truly acoustically analogous to human tissue was characterising the acoustic properties of the materials, particularly speed of sound and attenuation. As mentioned previously, when TMM or VMM was produced, small cylindrical samples (height: 18 ± 0.5 mm, diameter: 30 ± 0.5 mm) were made at the same time to allow for acoustic characterisation. In order to interrogate the acoustic properties of these samples, they were scanned using a scanning acoustic macroscope (SAM). The SAM system relies on a pulse-echo substitution technique. The SAM system consists of a single element transducer (7.5MHz, V320, Panametrics, General Electric, USA), suspended over a water tank with a glass plate at the bottom acting as a plane reflector, and a pulse receiver (5052PR, Panametrics, General

Electric, USA), and an analogue-to-digital converter card (NI PCI-5124, National Instruments, USA). Using a programme developed in LabVIEW (Version 8.1, National Instruments, USA) the signal measured from the transducer can be recorded. An illustration of the SAM system setup is given in Figure 4.4. By comparing the differences in signals between a sample and a reference pulse where the tank is empty, the speed of sound and attenuation can be determined from the following equations:

$$C_s = \frac{C_w}{1 + \Delta t \frac{C_w}{2d}} \tag{4.1}$$

$$a(f) = \frac{20}{2d} log_{10} \frac{A(f)}{A_0(f)} \tag{4.2}$$

Where: C_s is the speed of sound in the sample; C_w is the speed of sound in water; Δt is the time delay between the reference pulse and the sample pulse; d is the sample thickness; a(f) is the attenuation of the sample; A(f) is the pulse amplitude measured from the sample pulse, A_0(f) is the pulse amplitude measured from the reference pulse.

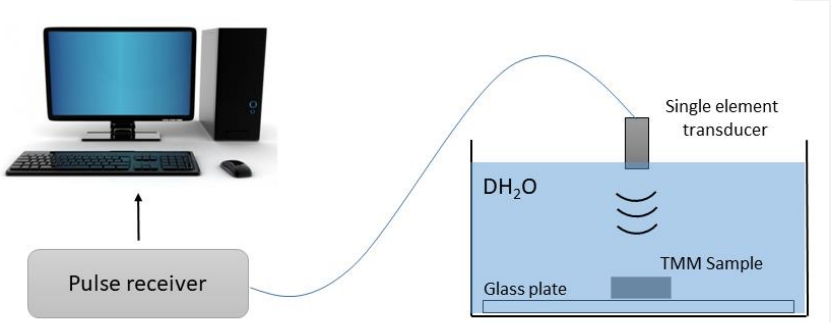

Figure 4.4: The apparatus of the scanning acoustic macroscope (SAM) system. A glass plate is submerged in a tank of deionised water which reflects the ultrasound pulse. By comparing the returning signals when passing through a material sample with a reference signal, acoustic properties can be measured.

4.2.5.2. Mechanical Characterisation

During the production of the PVA-c VMM, a number of dumbbell shaped test samples were produced using a custom 3D printed mould. The purpose of these samples to allow for tensile testing using a material tester (Lloyd Instruments LR30K*Plus*, Ametek, USA). The samples were tested in accordance with ISO 37 [105]. The ISO defined tensile stress as the stress applied which causes elongation of the test sample in the direction of application of the stress, expressed as the force divided by the original cross-sectional area of the test sample. The tensile strain was defined as the elongation of the test sample in the direction of the tensile stress divided by the original length of the sample in that direction.

Sample preparation involved the conditioning of the test samples at the temperature of testing (18.5 ± 0.5 °C) for a minimum of 3 hours prior to testing. For each of the samples, width and depth were measured using a Vernier callipers before being fitted to the grips of the materials testing system. The system was then activated manually and the grips

moved apart until a non-zero load was detected, indicating the samples were taut. Care was taken to ensure the samples were not experiencing a load greater than 0.5N before zeroing the system at this position. The length of the sample between the two grips was measured and used to calculate the elongation setting. The system was then operated at a speed of 50 mm min^{-1} until a strain of 30% was reached, with the strain automatically released back to the zeroed position at a speed of 50 mm min^{-1} which consisted one tensile cycle. Each sample underwent 5 tensile cycles at 30% elongation with a 500N load cell, producing 5 stress-strain curves. The analysis of these data was carried out in MATLAB (Mathworks, USA). The linear region of each stress-strain curve could be determined by performing second order numerical differentiation on the data and evaluating what region in the dataset had gone to zero. The Young's modulus was taken as the slope of the linear region of the 5^{th} tensile cycle.

In order to ensure the validity of the mechanical testing results, a number of vessel-like test objects were also produced. These consisted of a standard hollow cylindrical shape but did not feature a bend like the vessel mimics so as to limit radial asymmetry. The cross sectional area of these samples was calculated by measuring the inner and outer diameters and using the formula for the area of an annulus. The samples could then be fitted to the grips of the tensile testing system and tested using the same method as a dumbbell sample.

In total, 5 formulations of PVA-c were mechanically characterised, with 5 dumbbell samples and 6 vessel samples for each. The formulations tested were: 10% PVA-c 2, 3, 4, and 6 freeze thaw cycles and 15% PVA-c 2 freeze thaw cycles. The dumbbell and vessel samples were tested for correlation using a Pearson correlation analysis in MATLAB. The null hypothesis for the analysis was that the two variations of samples were not correlated, the alternative hypothesis was that there was a correlation between

the samples Young's modulus values with respect to the number of freeze thaw cycles. The null hypothesis was rejected if $p > 0.05$.

4.2.6. Blood mimicking fluid production

In order to accurately model a vascular system for Doppler ultrasound, it was important to accurately reproduce the properties of blood both as a fluid and as a Doppler scattering agent. The blood mimicking fluid (BMF) used in this work was based on the work carried out by Ramnarine et al. [2] in producing a fluid with the correct viscous properties of blood and the appropriate red blood cell equivalent to function as a scatterer in the form of Orgasol®® particles (Arkema, France). Figure 3.2 previously presented the relative backscatter of Orgasol® with respect to blood for three particle sizes; 5, 10, and 20 µm, as reported in that previous work. It can be seen from this figure that, for smaller particle sizes, a higher concentration of Orgasol® is required to achieve the same backscatter level present in blood. For this work, the 5 µm particle was selected as it is approximately the same size as red blood cells (6 µm) which function as scatterers *in vivo*. Therefore, the required concentration to achieve the correct backscatter is 1.82% w/v of 5 µm Orgasol®.

The components used in the production of BMF are outline in Table 4.4. Dextran (Sigma-Aldrich, USA), a branched complex glucan, formed the base viscosity of the fluid, closely matching the fluid dynamics of blood. Synperonic A7 detergent (Conservation Resources, Ltd, UK) was used as a surfactant; this lowered the fluid surface tension and allows for the dissolution of polar molecules enabling a homogenous suspension of Orgasol® particles in the fluid. Benzalkonium chloride (Sigma-Aldrich, USA) functioned as an anti-fungal agent, increasing the shelf-life of the BMF. Glycerol (Sigma-Aldrich, USA) was used as a plasticiser, which controlled the speed of sound in the fluid as well as fine tuning the viscosity.

Table 4.4: Constituent materials and concentrations used in the production of 1.82% Orgasol® BMF

Component	%(W/V)	Mass per 1L (g)
Orgasol® particles (5μm)	1.82	18.2
Dextran	3.42	34.2
Synperonic A7 detergent	0.92	9.2
Benzalkonium Chloride	0.46	4.6
Glycerol	10.25	102.5
Deionised water	83.13	831.3

The BMF was produced in two stages; first the fluid was produced using each component without the Orgasol®. The deionised water, glycerol, Synperonic A7 detergent, and benzalkonium chloride were mixed together in a 1L high-density polyethylene (HDPE) container with a screw top. The dextran was added to the HDPE container which was then sealed and shaken to combine. The container was then left in a warm place for a minimum of 3 hours. The second stage of production was the addition of the Orgasol® particles. Orgasol® was stored as an ultrafine powder and dry Orgasol® posed a significant health risk if inhaled or from skin or eye contact, therefore it was handled through a rigorous safety protocol. A small quantity of Orgasol® powder required for producing BMF was stored in a double sealed Tupperware and plastic zip lock bag inside an airtight Tupperware container to allow for ease of transport. The Orgasol® container was never opened outside of a fume hood. Using nitrite gloves, laboratory PPE, and a fume hood the Orgasol® powder could be weighed out and placed into the HDPE containers which

were then sealed. The work area was wiped down with alcohol wipes which were disposed of in a zip lock plastic bag along with the gloves used to prepare the Orgasol®.

Once the Orgasol® transfer was safely completed, the HDPE containers had to be shaken vigorously to wet the Orgasol® particles and thoroughly dissolve them in the solution. The resulting mixture was then passed through a fine mesh sieve (38 μm) and shaken in its container repeatedly until it could pass through the sieve without any residue remaining behind. The BMF was then ready for use in flow experiments. Prior to running any experiments, it was prudent to shake the BMF again to ensure the Orgasol® was in solution. This often resulted in the formation of air bubbles which would saturate the Doppler signal so care was taken to pour the BMF into the flow system reservoir slowly and the reservoir was connected to the flow system so as to draw BMF from the bottom of the reservoir and deposit BMF at the top of reservoir. Even after taking these precautions, significant air would often remain in the BMF as it passed through the flow system; the only remedy for this was to run the system at a high flow rate for approximately 1 hour to remove the bubbles.

4.2.7. Geometric accuracy

In order to assess the reproducibility of the VMM fabrication method used to produce the phantom lumens, the geometric accuracy was determined. Five LMA lumen moulds were produced and the diameter was measured at three locations along the moulds. The locations measured were 10 mm from the inlet, 10 mm from the bend and 10 mm from the outlet. All measurements were made using a Vernier callipers and repeated three times. The diameters of the models were compared across the three locations and between models using a one-way analysis of variation (ANOVA) test. The five LMA moulds were then used to make 5 vessels which were implanted in phantoms and the LMA was removed. The phantoms were then connected to the flow system, filled with a 9.5%

glycerol water solution which had a speed of sound of 1540 m s^{-1} and scanned in B-mode with an ultrasound system (Aixplorer, Supersonic Imagine, France) using a SL15-4 linear transducer at central transmission frequency of 5 MHz. Longitudinal images of the vessel were acquired for each specified diameter measurement location with the transducer positioned to place the focus of the transducer at the measurement location. The locations were specified using acoustic markers in the form of echogenic fishing line with diameter of 1 mm imbedded in the phantom perpendicularly to the vessel at the locations to be measured. These threads produced a strong reflected ultrasound signal allowing the locations to be found easily. For each measurement position three B-mode images were acquired.

Commented [AM16]: Added based on Kumar's comment

The images were exported to MATLAB and analysed using a line profile tool. The line profile identified the pixel intensity versus distance of a user specified region of interest which allowed for the clear differentiation of the vessel edges. An example of a line profile extracted from a B-mode image is shown in Figure 4.5. The pixel distance of the vessel diameter was converted to distance (mm) by multiplying the pixel distance by the pixel spacing of the scanner. A one-way ANOVA test was carried out on the diameters in each phantom and between each phantom. A paired t-test was carried out between each LMA mould and its corresponding phantom for the three locations. The null hypothesis for each statistical test was that there was no difference between any of the diameters measured. If $p < 0.05$ then the null hypothesis was rejected and the alternative hypothesis was that there was a statistical difference between the diameters. All statistical tests were carried out in MATLAB.

Commented [AM17]: Clarified based on Kumar's comment

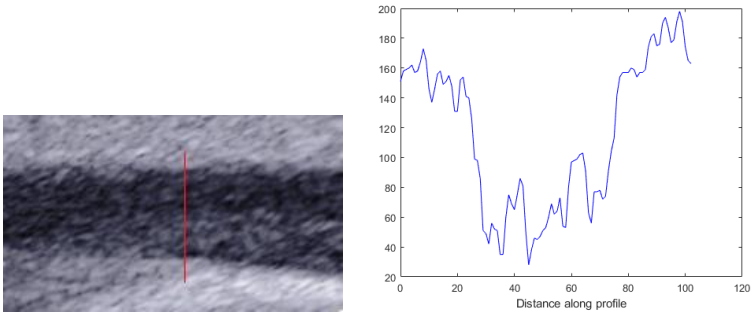

Figure 4.5: An example B-mode image (left) of the phantom lumen and the line profile (right) extracted from it. The diameter of the vessel was calculated by multiplying the number of pixels across the lumen with the pixel spacing of the ultrasound scanner.

4.3. Results

4.3.1. Acoustic characterisation

The results of the acoustic characterisation are presented in Figures 4.6 and 4.7. As the number of freeze thaw cycles was increased, a corresponding increase in speed of sound was found, varying in the range of 1556 – 1567 m s^{-1} for 2 – 6 f/t cycles. The values for the speed of sound were found to be within one standard deviation of the *in vivo* value for speed of sound for all freeze thaw cycle values, with the exception of 2 freeze thaw cycles.

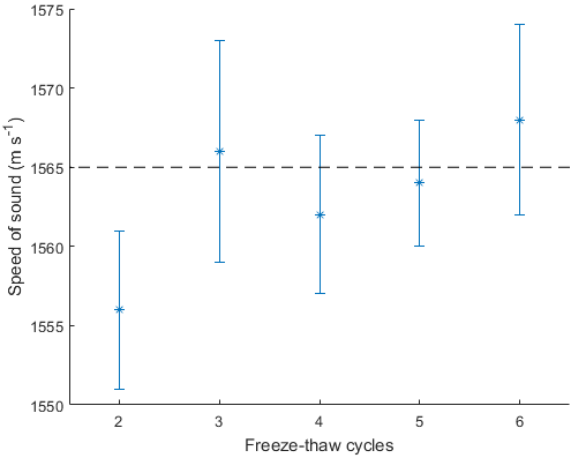

Figure 4.6: The effect of increasing freeze thaw cycles on speed of sound measurements for PVA-c. The error bars correspond to one standard deviation. The dashed black line indicates the* in vivo *value for arterial speed of sound [4]**.**

Similarly, the attenuation was found to increase with increasing numbers of freeze thaw cycles. The measured values of attenuation varied in the range 0.520 – 0.575 dB cm^{-1} MHz^{-1}. Again, these values were all within one standard deviation of the *in vivo* value for arterial attenuation with the exception of 2 freeze thaw cycles.

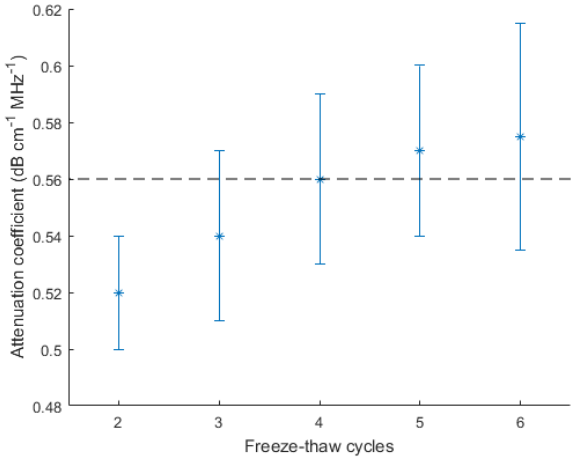

Figure 4.7: The effect of increasing freeze thaw cycles on attenuation measurements for PVA-c. The error bars correspond to one standard deviation. The dashed black line indicates the* in vivo *value for arterial attenuation.

4.3.2. Mechanical characterisation

The results of the mechanical characterisation are presented in Figure 4.8. For each number of freeze thaw cycle, the Young's moduli of the vessel-like samples were comparable to the Young's moduli values of the dumbbell test samples produced in accordance with ISO 37. The Young's modulus values with analysed using Pearson correlation, which gave an R^2 value of 0.9767. The p-value for this analysis was p = 0.0013, indicating that the R^2 value was highly significant and the alternative hypothesis was accepted.

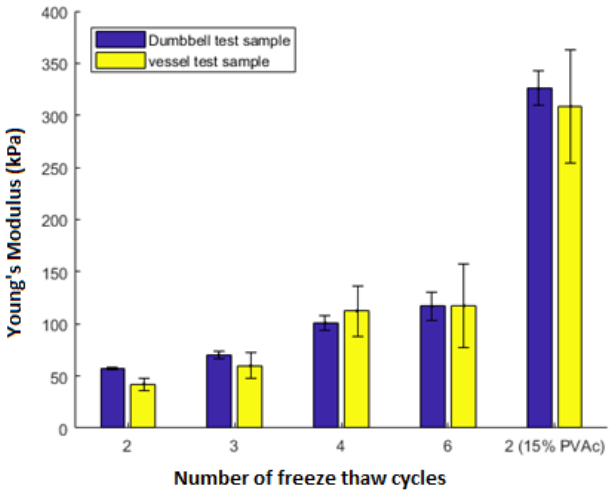

Figure 4.8: Comparison of Young's modulus values for increasing freeze thaw cycles between ISO 37 dumbbell test samples and the vessel-like test sample. The error bars correspond to one standard deviation.

4.3.3. Geometric Accuracy

The measured mean diameter (in mm) of the 5 LMA cores at 3 measurement positions as compared to the diameters measured using the line profile analysis of the phantom lumens at equivalent positions are presented in Table 4.5. A one-way ANOVA statistical test carried out for the populations of diameters between the measurement locations and between the LMA cores indicated that the diameters were the same at each measurement location and for each LMA core ($p = 0.3368$). An additional ANOVA test was carried out on the diameters measured using the line profile analysis procedure, with no significant difference in measured diameter detected ($p = 0.1763$).

Table 4.5: Comparison of mean diameters at three measurement locations across five LMA cores and five phantom lumens. LMA cores were measured using a Vernier calliper and the lumens were measured in B-mode.

Location	Mean Diameter LMA core [mm]	Mean Diameter phantom lumen [mm]
Inlet	7.61 ± 0.04	7.77 ± 0.04
Bend	7.58 ± 0.04	7.69 ± 0.05
Outlet	7.61 ± 0.04	7.66 ± 0.053

4.4. Discussion

When modelling a complex anatomical feature *in vitro* using non-biological materials, an important advantage gained over using, for example, excised biological tissue, is the ability to consistently produce an identical test environment to a high degree of precision across multiple phantoms, allowing for modification of individual geometric parameters while keeping the rest of the phantom design identical. It was important, therefore, to ensure that the procedure utilised demonstrated a high degree of repeatability. This meant that the ideal phantom material would be one which could be reliably reproduced to a high degree of anatomical realism.

Utilising a newly developed formulation of PVA-c to mimic arterial tissue, a technique for producing a range of anatomically realistic renal artery flow phantoms featuring varying degree of vessel stiffening was developed. This material was selected as the vessel mimicking material due to its unique crosslinking properties that allow its stiffness to be precisely controlled. The formulation of PVA-c can be complex and some

constituent materials, specifically particulate materials, commonly used elsewhere in TMM manufacturing are not suitable due to the relatively long set times of PVA-c.

The procedure used in the production of the PVA-c material was outlined. The vessel mimics were implanted horizontally at a depth of 7 cm, analogous to the depth of the renal artery in the abdomen [110]. Previous work using PVA-c has focused on its potential use in the design of late stage CVD phantoms in the formation of stenoses [108] or in liver perfusion phantoms [89]. A similar phantom construction procedure was carried out Qian et al. [111] for the purpose of particle image velocimetry; the authors utilised a similar formulation of PVA-c to produce a range of straight walled flow phantoms for the purposes of measuring the velocity profiles and calculating the wall shear rate. The primary difference between this work and that of Qian et al. is the use of anatomically realistic vessel geometries based on real patient data. These complex geometries required a more rigorous and novel means of confirming the mechanical properties of the material and, in combination with the varying wall stiffnesses modelling progressing CVD, these phantoms presented a novel testbed design that provides a clear and reproducible model of atherosclerosis *in vivo*.

Commented [AM18]: Reworded based on Kumar's comment

The geometric accuracy of the phantom lumen was assessed with respect to the clinical data of a healthy renal artery. The two sets of diameter measurements were compared using a one-way ANOVA statistical test, first on the LMA core population between the three measurement locations and second as a comparison between the LMA core diameters and the phantom lumen diameters. The ANOVA tests indicated that the LMA cores reliably produced vessels of the correct diameter consistently ($p = 0.3368$, $p = 0.1763$).

To ensure that the materials used in the construction of these flow phantoms were an accurate facsimile of the tissues *in vivo*, the acoustic properties of the vessel mimicking material were evaluated using a scanning acoustic macroscope. The speed of sound of the material varied between 1556 ± 5 to 1567 ± 6 m s^{-1} and the attenuation varied between 0.52 ± 0.02 to 0.58 ± 0.04 dB cm^{-1} MHz^{-1}. For 3 – 6 freeze thaw cycles, the values recorded were within one standard deviation of the *in* vivo value given in the literature for both the speed of sound and the attenuation of the material [4]. Research into arterial acoustic properties in the later stages of arterial disease indicate a potential change in the properties of tissue; for example, Saijo et al. [112] studied excised human coronary arteries featuring advanced atherosclerosis to determine their acoustic properties using a scanning acoustic macroscope. The results showed that the intima showed significantly increased speed of sound values in regions with collagen fibre present and where the vessel had become calcified (1680 ± 30 m s^{-1} and 1810 ± 25 m s^{-1} respectively). This indicates that as CVD progresses a more thorough modelling of the situation *in vivo* would include a corresponding increase in speed of sound. This is not entirely unexpected as the speed of sound and Young's modulus are related according to the equation:

$$c = \sqrt{\frac{E(1-\sigma)}{\rho(1+\sigma)(1-2\sigma)}} \ldots \tag{4.3}$$

where c is the speed of sound, E is the Young's modulus, ρ is the density of the material, and σ is the Poisson's ratio which can be taken as approximately 0.5 for soft tissue, and the […] denotes higher order terms which can be neglected [112]. Considering that the rest of Equation 4.3 is approximately constant for soft tissue, the relationship between speed of sound and Young's modulus can be exploited using ultrasound to allow for a more direct measurement of mechanical properties, this is the underlying mechanism to

shear wave elastography; the acoustic radiation force of the incident ultrasound beam can be used to produce shear waves through the medium which can be detected using ultrasonic tracking methods. This allows for the generation of tissue maps where the shear modulus of tissue acts as the contrast mechanism [78]. The velocity of these shear waves is then used to determine the local stiffness in the imaging region.

Similarly, for measurements of the speed of sound, an increase in attenuation was observed as a function of increasing freeze thaw cycles. This was also an expected result as the attenuation is proportional to the density of the material which increases as additional crosslinking takes place. Although the increase in speed of sound and attenuation appears to be linear in Figure 4.6 and Figure 4.7, it was expected that this steady increase would begin to reach an asymptotic limit as the absolute number of PVA molecular strands become crosslinked [56].

Commented [AM19]: Added based on Dervil's comments

To ensure that the phantoms were accurately modelling the increase in vessel stiffness as an indication of progression of CVD, the mechanical properties of the PVA-c material were measured for a number of freeze thaw cycles. Some previous mechanical characterisation of PVA-c has relied on the use of compression testing as outlined in ISO 7743, working under the assumption that a large cylindrical test sample would have broadly equivalent mechanical properties to the much smaller vessel [56,57,98,103,113]. As discussed earlier there are a number of limitations to this assumption, and a more direct comparison of mechanical properties was investigated using tensile testing, as outlined in ISO 37. The tensile testing was carried out using a dumbbell-shaped sample and compared directly to the vessel using a hollow cylindrical vessel-like test sample. It was believed that this would allow for a more direct comparison because the elastic properties of PVA-c are strongly related to the rate of thawing, which will take place over a longer timescale for a larger sample volume. The Young's modulus values for the

Commented [AM20]: Added based on Kumar's comment

dumbbell samples varied in the range 62 – 119 kPa for the 10% w/v PVA-c material for 2 – 6 freeze thaw cycles, and a single 15% w/v PVA-c batch was found to have a Young's modulus of 320 kPa for 2 freeze thaw cycles.

For each freeze thaw cycle, the vessel-like sample showed very similar results to the dumbbell sample. The two sample times were correlated ($R^2 = 0.9767$). This indicated that the dumbbell samples were extremely accurate in their modelling of the true stiffness values of the vessels produced for the phantoms. This further indicates that tensile testing carried out in accordance with ISO 37 is a more useful quantitative tool for the mechanical characterisation of PVA-c. This has provided a means of quantitatively assessing the Young's modulus for unorthodox vessel geometries through comparison with the dumbbell samples produced in accordance with ISO 37. The validity of this comparison was further strengthened through the use of an extremely precise production and freeze-thaw process. In effect, we have ensured that the mechanical characteristics of the PVA-c used in this work were highly tuneable with reproducibility precise values and we have provided a clear demonstration of the correlation between an industrial standard sample and our vessels instead of relying on there being an implicit correlation.

It is worth noting, however, that as the number of freeze thaw cycles increases, a stiffness maximum will gradually be achieved. This can be seen in Figure 4.8 where the increase in Young's modulus is less as the number of freeze thaw cycles increases. This would indicate that if the number of freeze thaw cycles is sufficiently large, the difference in rate of thawing due to sample volume becomes less significant as the material approaches its stiffness maximum regardless.

The Young's modulus values measured closely followed the literature values for approximate tissue stiffness. The most recent literature regarding vessel stiffness

estimated an upper bound for healthy arterial stiffness of 34.9 – 83 kPa [65,67] and an estimated range of diseased vessel stiffness of 116 – 751 kPa [66,67]. This indicates that for the samples produced, the 10% w/v PVA-c demonstrated an ideal healthy vessel stiffness for 2 – 3 freeze thaw cycles while the lower bound of typical diseased vessel stiffness was achieved for 4 – 6 freeze thaw cycles. There is a limit to the achievable vessel stiffness for a given percentage of PVA-c which, in addition to the inconvenience of the relatively long production times, preclude the use of 10% w/v PVA-c from suitably mimicking the higher stiffnesses recorded in diseased arteries. For this, 15% w/v PVA-c can be used as low as 2 freeze thaw cycles to mimic the more developed stages of the disease. In order to mimic an advanced form of atherosclerosis, the 15% w/v PVA-c solution could be tested for suitability as a vessel mimic at higher freeze thaw cycles, although the value is well within its range of possible stiffnesses as 15% w/v PVA-c has been observed with Young's modulus values as high as 1840 kPa [98]. This means that our vessel phantom can be accurately produced with the range of stiffnesses which correspond to a broad classification of early stage atherosclerosis, providing a strong and reliable testbed for measuring the flow characteristics of blood during disease progression. This allowed for the comparison of flow characteristics between different vessel stiffness values which can be taken as approximating stages of the disease. This meant that the phantom model could provide an insight into the role of WSS as a diagnostic tool in the diagnosis of CVD.

Commented [AM21]: Kumar's comment

Commented [AM22]: Kumar's comment

Commented [AM23]: Rephrased per Kumar's comment

4.5 Conclusion

The purpose of this chapter was to describe the development of a technique for producing consistent flow phantoms to provide a reliable testbed for Doppler flow experiments. It was important that the phantoms could be produced with: acoustically analogous

properties to human tissue *in vivo*; precisely controlled stiffness values; and consistent geometric accuracy.

This study provided a formulation of PVA-c that did not suffer from issues such as constituent settling or issues that would otherwise threaten the homogeneity of the material.

The results of this study indicated that PVA-c can be reliably produced with known acoustic properties. Previous work with this material has often opted to utilise compression testing to mechanically characterise it, however, this may not be a reliable method of ascertaining the mechanical behaviour of PVA-c. This work provided a method to verify the true stiffness of PVA-c vessels and showed a correlation between these data and a reliable benchmark to assess stiffness using tensile testing according to ISO 37.

This study tested the geometric reproducibility of this procedure and showed that the dimensions of the model used translated to the final vessels with a high degree of precision.

Phantoms are a useful resource in the validation of many diagnostic techniques. One of the best ways to test new and ground-breaking techniques is through the use of multimodality phantoms. Using the procedure outlined in this chapter, a multimodality phantom could be produced. This could be achieved by replacing the deionised water used in the PVA-c vessel production with a 10% w/v manganese chloride solution to allow for MRI imaging. Additionally, the use of attenuators in the production of the tissue and vessel mimicking materials could allow for adaption to CT imaging through minor modification of the Hounsfield units. This relatively simple adaption would allow for additional testing using CT and MRI imaging and a direct comparison between new techniques and established diagnostic methodologies. The addition of either of these

modifications of the production would likely result in an increase in Young's modulus, speed of sound, and attenuation, therefore the addition should be carried out with rigorous acoustic and mechanical analysis to ensure that the expected ultrasound properties are not significantly perturbed by this process. This is beyond the scope of this work, however, and is one possible avenue for further exploration in this area.

Commented [AM24]: Added based on Kumar's comment

This chapter provided a bedrock of validity to the rest of this work by establishing the consistency and accuracy of the production methods. This allowed for the production of a series of Doppler flow phantoms which could be used for further experimentation.

Chapter 5: Development of multifrequency *UltraFast* Doppler spectral analysis (MFUDSA) algorithm

5.1. Introduction

As stated previously, in order to measure WSS it is necessary to address several key imaging limitations associated with the technique as it currently stands, namely, the Signal-to-Noise ratio (SNR), the temporal resolution and the velocity resolution all need to be improved. The temporal resolution can be dramatically increased through the use of *UltraFast* Doppler acquisitions which utilises a series of tilted plane waves to allow for the measurement of velocity for each point in the vessel segment within the imaging plane in a single time point. The remaining limitations to the WSS measurement, namely SNR and velocity resolution, can be addressed by applying additional post processing steps to extract additional information from the full bandwidth of transmitted frequencies. The purpose of this chapter is to outline the approach and methods which were implemented as part of this project to make further improvements to the SNR and velocity resolution of the Doppler signal using digital spectral analysis.

5.1.1. Doppler processing

In order to develop an algorithm for the 2D Fourier analysis of Doppler data, it was first necessary to understand the requisite steps and define the criteria for optimum Doppler analysis and then develop an algorithm which incorporates each of those steps, in addition to performing the required analysis. A simplified block diagram of a standard pulsed Doppler system is given in Figure 5.1.

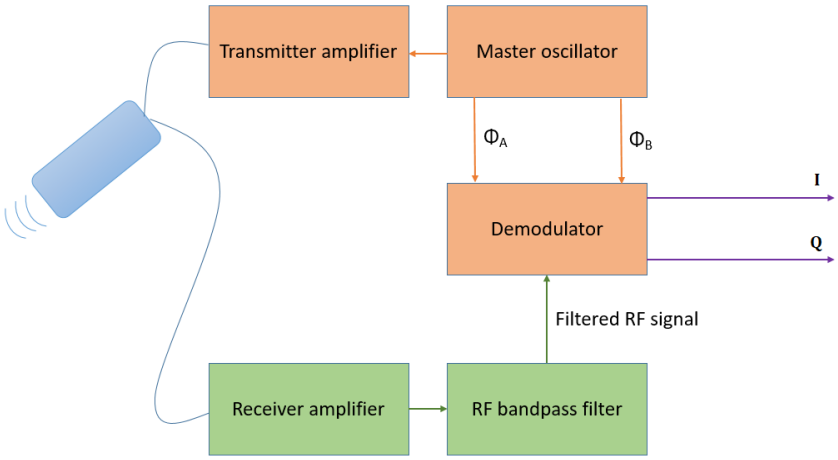

Figure 5.1: A simplified pulsed Doppler system. The pulse is defined by the master oscillator. The received echoes are demodulated using a reference from the master oscillator. I and Q are the resulting in-phase and quadrature outputs of such a system.

The principle of operation of a pulsed Doppler system is as follows [5]: the desired ultrasound pulse is specified by the master oscillator, this pulse is amplified and sent to the transducer for insonation of the medium of interest. The returning echoes are received and amplified before passing through a bandpass filter. A sharp low pass filter is used to remove the sampling frequency of the signal while retaining the lower Doppler shift frequencies, a high pass filter (wall filter) is also employed to remove the high amplitude, low frequency tissue clutter signal. The filtered signal is then demodulated, although the demodulation is commonly performed prior to the application of filters on modern digital ultrasound scanners. A more detailed schematic of a typical demodulator is illustrated in Figure 5.2.

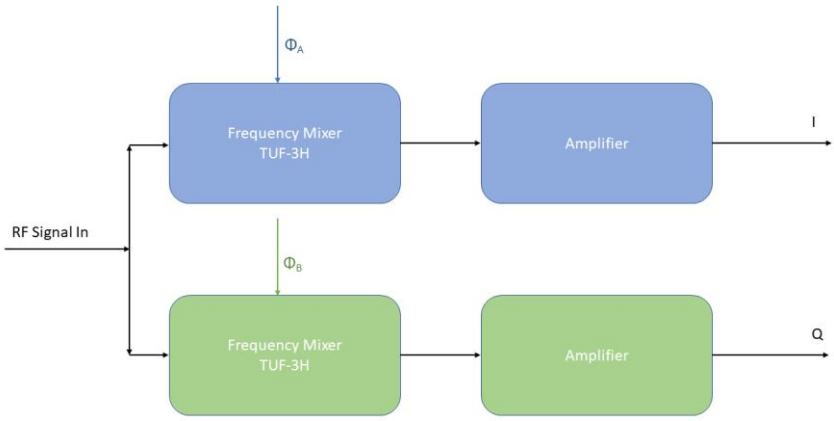

Figure 5.2: A typical demodulation block diagram used for pulsed wave Doppler signal analysis [5]

The most commonly used method of demodulation is phase-quadrature demodulation. This method uses two signals acquired from the master oscillator, φ_A and φ_B, which are an identical copy of the transmitted pulse and the transmitted pulse phase shifted 90°. By creating two out-of-phase signals, it is possible to determine the directionality of the recorded Doppler shifts. This can be carried out using a complex Fourier transform. This process can only be carried out on a digital system, unlike earlier analogue analysis methods, but its implementation is very simple. A complex signal is made by combining the IQ data as in Equation 5.1.

$$S(t) = I + Qi \tag{5.1}$$

When the signal, S(t), undergoes a complex Fourier transform, due to the symmetry properties of frequency space, the real part of Fourier spectrum will contain only the Doppler shifts corresponding to motion towards the transducer, whereas the imaginary part of the Fourier spectrum will contain those moving away from the transducer [5].

5.1.2. 2D Fourier analysis

Traditionally, when analysing Doppler pulses, the demodulated IQ signal, S(t), would undergo a 1D complex Fourier transform to produce a 1D frequency spectrum corresponding to the central transmission frequency. In the idealised case, where S(t) is a pure sine wave reflected from a line of particles of uniform velocity, the resulting frequency spectrum would resemble a delta function with a peak at the Doppler shift frequency corresponding to the velocity of the scatterers. As additional velocities are added, this delta function will spread into a Gaussian peak with a width dependent on the range of velocities present, if a sufficiently different velocity (greater than the velocity resolution of the system) is present it would result in a secondary peak in the frequency spectrum. By repeating this Fourier analysis over the entire time window, a sonogram can be produced which is commonly referred to as the Doppler spectrum. This spectrum is displayed as a column of greyscale values for each time point where the vertical axis represents the axial velocity derived from the Doppler frequency shift. Doppler spectra produced using discrete Fourier transforms tend to exhibit random fluctuations due to the stochastic nature of the ultrasound scatterers (red blood cells). These fluctuations are the cause of the typical granulation of the spectra which is known as Doppler speckle, and is regarded as a major limitation of discrete Fourier transform based spectral analysis [3,5]. A number of approaches have been proposed to counteract this limitation such as parametric spectral estimators and various smoothing functions [50,114]. Spectral estimators reduce spectral variance by limiting the influence of significant outliers to the data. For example, a moving average estimation method, such as the Blackman-Tukey transform, will provide this improvement by defining a subset size for a certain data series. The initial subset will consist of the first N values of the series, where N is the subset size; the first digit of the processed data series will be the average of the initial

subset. The subset will then shift forward by one, encapsulating the second element of the original data series onwards and generate the second digit of the processed data series as the average of the new subset. A moving average estimator, therefore, works as a kind of low pass filter, removing high frequency fluctuations from the data at the expense of frequency resolution [50]. Similarly, smoothing functions can be applied directly to the Doppler spectrum with the goal of reducing local variations at the cost of frequency resolution [114]. These methods provide a reduction in variance, allowing for a more qualitative view of the bulk trends in data over larger ranges, but they come at the expense of a strict decrease in quantitative information. An alternative approach to improve the quality of the generated sonogram through more rigorous analysis procedures such as 2D Fourier analysis which can provide similar improvements to the Doppler spectrum through the analysis of additional information and for no commensurate loss in resolution.

Commented [AM25]: Added based on Dervil's comments

Commented [AM26]: Added based on Dervil's comments

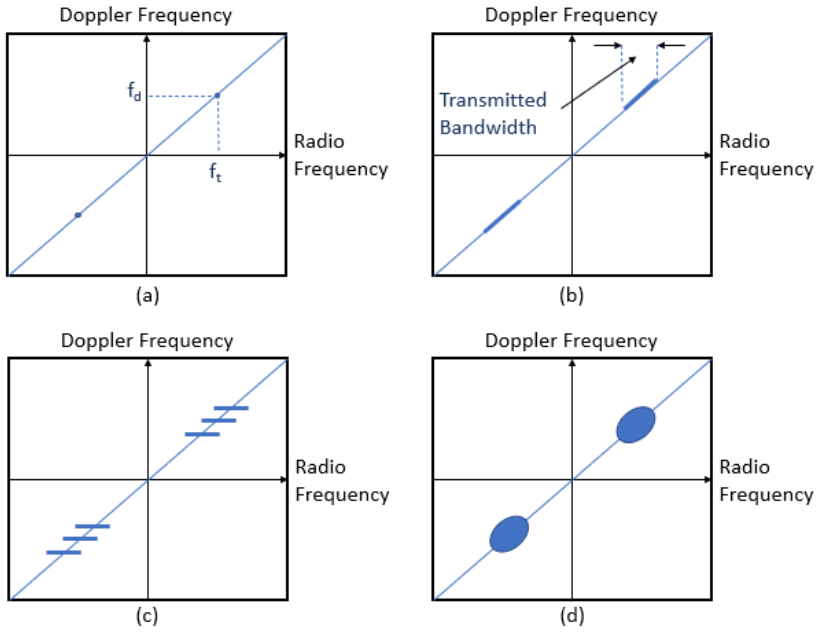

Figure 5.3: Visualisation of the frequency space produced from a 2D complex Fourier transform (adapted from Evans & McDicken [5]***.)***

(a) The ideal case of a pure sine wave results in a delta peak at coordinates (f_t, f_d).

(b) A range of transmission frequencies results in radial broadening of the spectrum.

(c) Finite sample volume length and finite observation time lead to broadening of the spectrum.

(d) The combination of these effects produces an ovular spectral distribution.

Returning to the ideal case of a pure reflected sine wave of uniform velocity, a 2D Fourier analysis would produce a frequency space where the delta function would be centred with coordinates of (f_t, f_d) where f_t and f_d are the transmitted and Doppler shift frequencies respectively (Figure 5.3(a)). It should be noted that in this idealised case, where the received pulse is a pure sine wave, all the information about the Doppler signal is contained in the 1D spectrum and no additional information can be gained from 2D

analysis. In practice, however, a pulsed wave Doppler system necessarily will transmit a range of frequencies which results in a broadening of the function along a radial line passing through the origin (Figure 5.3(b)). It has been shown that the slope of the radial line is proportional to the velocity of the scatterers [115], which makes intuitive sense considering that different velocities would lie on different points on the y axis, necessitating differing slopes to pass through the origin, with greater velocities resulting in larger slopes. An additional practical effect is the broadening of the spectrum in both the RF direction and the Doppler frequency direction due to a combination of finite sample volume length and finite observation time. This results in a smearing of the signal in both axes (Figure 5.3(c)). By combining all of these effects, the resulting frequency space display of a uniform velocity will resemble ellipses with the slope of the major axis of an ellipse being proportional to the velocity it represents [5]. Additionally, it is worth noting that the intensities of the 2D Fourier space representation of the signal can be extracted along the line $x = f_t$ to give the 1D Fourier spectrum, as seen in Figure 5.4.

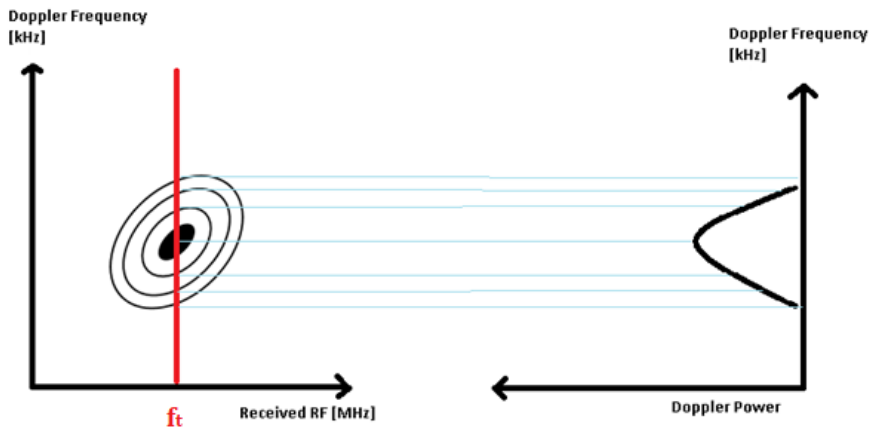

Figure 5.4: By evaluating the 2D Fourier space representation of a reflected ultrasound signal at the central transmitted frequency, the standard 1D Fourier spectrum emerges.- adapted from Evans & McDicken [5]**.**

There is, therefore, additional information to be gleaned from the 2D Fourier space that can be used to improve the precision of Doppler ultrasound. Two potential methods to extract this information are presented here.

The first method to utilise the additional 2D Fourier data is 'velocity matched spectrum' analysis first proposed by Torp et al. [6]. The mechanism behind this analysis approach is that the slope of the frequency space signal can be used to evaluate its corresponding velocity. This could be done by "scanning" with a certain expected velocity, for which the correlation length will be maximised when the true velocity matches the expected velocity. In principle, this could be done by manually drawing a line of best fit in the frequency space and measuring its slope and repeating this procedure for each time point of interest. It is mathematically equivalent to, instead, simultaneously processing several

data samples from different depths, allowing the movement of scatterers along the ultrasound beam to be measured between pulses. This results in a so-called range/time space which can be much more readily analysed using this method. By scanning through the range/time space with a number of predetermined velocity vectors, the magnitude of the correlation for each velocity can be recorded as the intensity of the velocity spectrum at that velocity. An example of this procedure is illustrated in Figure 5.5. This is effectively equivalent to integrating the 2D Fourier spectrum along a series of radial lines through the origin corresponding to pre-defined velocity values. One significant advantage of this procedure is that it can potentially supress the effect of aliasing in the Doppler spectrum. This is possible due to the fact that additional Fourier transform replicas in frequency space appear repeated infinitely along the Doppler frequency axis. And while the replicas are shifted in the Doppler frequency axis, they are not shifted in the RF axis, meaning that it maintains the same gradient. Torp et al. used this feature of the velocity matched spectrum analysis to supress the effect of aliasing for a Doppler signal from the subclavian artery which had a peak velocity at 4.5 times the Nyquist limit. Torp et al. could not remove the aliasing completely, but demonstrated that the Doppler spectrum could be extracted manually, indicating that with modern technology an automatic method could potentially be developed [6].

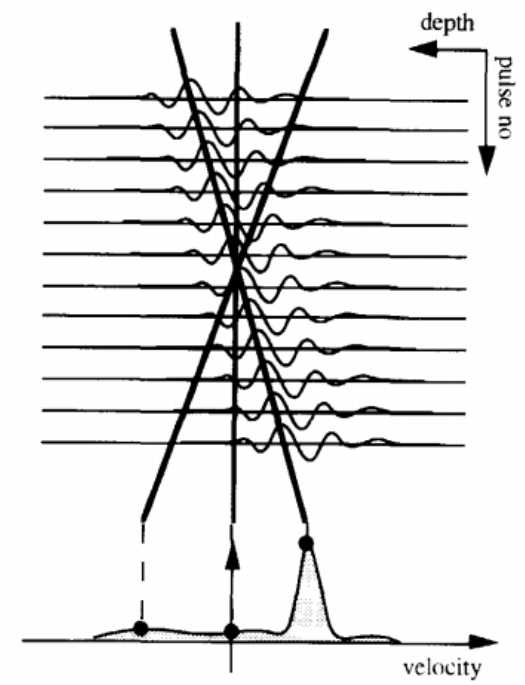

Figure 5.5: An example of the procedure used in velocity matched spectrum analysis to produce a velocity spectrum using 2D Fourier data – adapted from Evans & McDicken / Torp [5,6]**.**

The second method which can be used to extract additional information from the 2D Fourier transform is multifrequency Doppler analysis, first proposed by Loupas et al. [7,116,117]. It can be shown that it is possible to reduce the spectral variance of the power spectral density spectrum of a Doppler signal by averaging several uncorrelated Doppler spectra from different frequencies transmitted simultaneously [118]. The principle of multifrequency Doppler is a variation on this method where, instead of transmitting additional frequencies, the additional spectral information is derived instead by utilising the entire transmitted bandwidth of an ultrasound pulse. This can be thought of as though

the bandwidth of transmitted frequencies were individual transmitted pulses of zero bandwidth at a number of varying frequencies. In order to properly compute a spectral average of these uncorrelated spectra, it is first necessary to provide the appropriate spectral scaling before integrating the 2D frequency spectrum across the bandwidth of the pulse. Using this method, an expression for the power spectral estimate of the 2D Doppler spectrum, $\hat{P}_{MF}(f_d)$, may be written as:

$$\hat{P}_{MF}(f_d) = \frac{\int_{f_c-BW/2}^{f_c+BW/2} P(f_{RF}, \frac{f_d f_{RF}}{f_c})\, df_{RF}}{\int_{f_c-BW/2}^{f_c+BW/2} |U(f_{RF}-f_c)|^2\, df_{RF}} \tag{5.2}$$

Where, f_c is the central transmitted frequency, BW is the bandwidth of the pulse, $|U(f_{RF}-f_c)|^2$ is the Fourier transform of the pulses complex envelope, and $P(f_{RF}, \frac{f_d f_{RF}}{f_c})$ is the 2D frequency spectrum with the spectral scaling applied. Note that in the numerator, the contribution to the integral at $f_{RF} = f_c$ is the standard 1D Fourier transform and that RF frequencies greater than f_c will be compressed while frequencies less than f_c will be expanded [7]. An alternative way of viewing Equation 5.2 is as an integration along radial lines of the frequency plane passing through the origin. In this sense, the computation carried out is mathematically analogous to the procedure of velocity matched spectrum analysis, albeit computationally distinct. If this integral was computed without the spectral scaling present, it would be equivalent to integration of the 2D frequency spectrum along the RF axis which would result in significant spectral broadening.

The multifrequency Doppler showed considerable promise when first proposed with Loupas & Gill [7] finding a relative improvement in SNR of between 70 – 360%. The technique was also compared to another method for reduction of spectral noise; Welch's method. A comparison between a 1D Fourier analysis with no additional processing, a

1D Fourier analysis incorporating Welch's method, and a 2D Fourier analysis incorporating multifrequency Doppler is given in Figure 5.6. It can be seen in Figure 5.6 that out of the three Fourier analysis techniques presented, the multifrequency Doppler approach resulted in the lowest spectral variability while the standard 1-dimensional Fourier analysis had the greatest spectral variability. Welch's procedure exhibited an intermediate level of spectral variance which is expected as this procedure is a well-known method for the improvement in spectral estimates. It follows from this illustration therefore that multifrequency Doppler has the potential to provide an even greater improvement to spectral estimates.

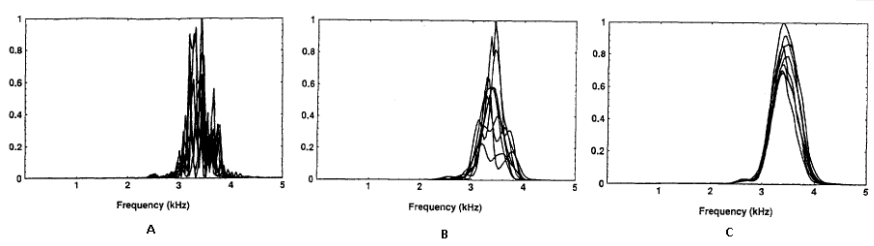

Figure 5.6: A comparison between 8 Doppler spectra computed using (a) 1D Fourier analysis with no additional processing, (b) 1D Fourier analysis incorporating Welch's method, and (c) 2D Fourier analysis incorporating multifrequency Doppler – adapted from Loupas & Gill [7]**.**

5.2. Methodology

5.2.1. Multifrequency *UltraFast* Doppler spectral analysis (MFUDSA) algorithm

The data used for the analysis in this work was acquired using a dedicated research package installed on the Aixplorer ultrasound scanner (Supersonic Imagine, France)

which allowed extraction of raw in-phase quadrature (IQ) data. These data were intended by the manufacturer for use in autocorrelation computation for colour Doppler and sample code was included with the research package, written in MATLAB (Mathworks, USA) for this computation. This data format was suitable to undergo multifrequency Doppler analysis and with some modifications to the sample code it would then be possible to perform multifrequency Doppler analysis on *UltraFast* Doppler data. This required a new processing algorithm to be developed which could be used in conjunction with *UltraFast* data, the multifrequency *UltraFast* Doppler spectral analysis (MFUDSA) algorithm, which was developed and evaluated in this project, the details of which are provided in the following paragraphs.

The MFUDSA algorithm was designed to take raw IQ Doppler data from the Aixplorer system and perform the necessary post-processing to produce a velocity output. A block diagram of the new developed MFUDSA algorithm is illustrated in Figure 5.7.

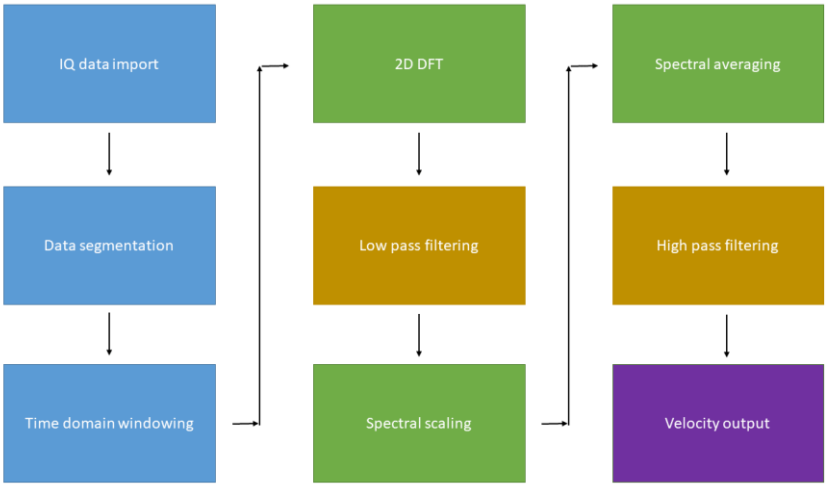

Figure 5.7: A block diagram of the steps in the MFUDSA algorithm. The diagram is colour coded to correspond to the different stages in the cycle: blue items are processing operations taken on the data in the time domain; green items are processing steps taken in the frequency domain; yellow items are signal filtering; and purple corresponds to the output information sent to the user.

The raw data was exported from the Aixplorer as a .DATA file format. This file included not just the measurement data but also the header data with information about the transducer and transmission settings for code optimisation. The first step was to extract the raw IQ data from this file. The IQ data would consist of a 1D vector of alternating pulses which would be reshaped into two matrices of dimensions x*y*t where x and y are the horizontal and vertical resolutions of the imaging field in pixels and t is the number of frames of the acquisition. These two matrices, I and Q, were the demodulated received signals from the imaging field. As the demodulation took place using on board processing, it was not necessary to perform that procedure in the algorithm. The I and Q matrices

were then linearly combined in the form IQ = I + Qi where i was the imaginary number. A representation of this new matrix, IQ, is given in Figure 5.8.

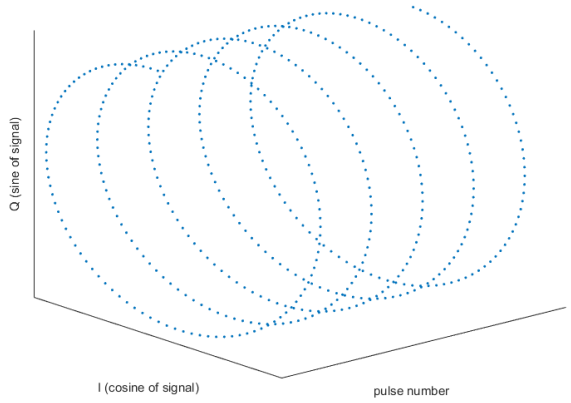

Figure 5.8: A representation of the combined IQ data form exported from the scanner in the form cos(S) + i*sin(S) where S is the original received signal and i is the imaginary number. This data was then analysed using in-house developed MATLAB code.

This data matrix was considerable in size, often approaching 1 GB, and had to be held in RAM for use in computations. However, a large portion of it was not significant for the purposes of Doppler processing as only the signal from inside the vessel was important. An improvement in processing speed was achieved by discarding unnecessary components as early in the procedure as possible. This was achieved by displaying a single frame of the acquisition and having a user input the start and end points of the vessel in the field of view. The vessel lumen diameter was 7 mm which corresponded to 70 pixels in the matrix, it could therefore be assumed that if the user specified points

within the vessel for the start and end points, the program could automatically discard any data with an index number 70 pixels lower than the lowest y co-ordinate specified and any data with an index number 70 pixels greater than the highest y co-ordinate specified. This assumption would be valid provided that the imaging region did not shift significantly during the acquisition, which in itself, would be grounds to discard a dataset, so this was taken as a reasonable assumption. The segmentation of the data was also used to isolate individual "pulse lines" to continue the processing of the algorithm. While these vertical lines were not true "pulse lines" as in traditional pulse wave Doppler (due to the plane wave acquisition utilised in *UltraFast* Doppler) they were taken to be analogous to pulse lines for ease of computation. The vessel was split into a number of vertical vectors and each vector was treated as a single pulsed wave Doppler acquisition. For each vector, there was a number of vectors each holding a range of ultrasound echoes where each vector represented a time point. The total number of frames in the acquisition determined both the frequency/velocity resolution of the output spectrum and the temporal resolution of the sonogram that would be produced (i.e. the product of number of frames used in the Fourier transform and the number of time points in the resulting sonogram could not exceed the total number of recorded frames). This section assumes a steady flow regime so that every acquisition frame can be utilised for generating the Fourier spectrum for now, generating sonograms which will be described later in this chapter. The range gate was digitally specified by selecting a pixel width of the gate and it was then iteratively moved through each vector using a "for" loop. The process of data segmentation is illustrated in Figure 5.9.

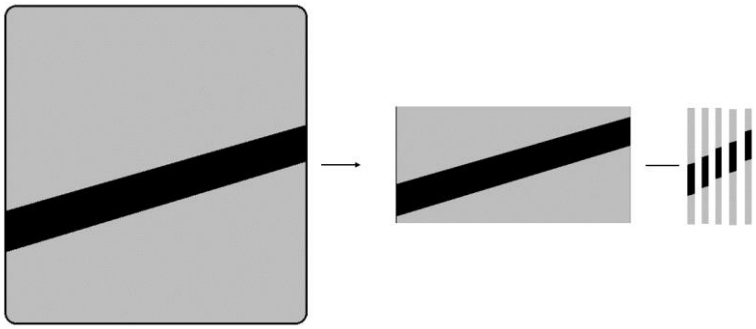

Figure 5.9: The segmentation process for the IQ data matrix. Considerable memory savings were made by discarding irrelevant data corresponding to areas of the imaging region outside the vessel lumen. This sectioning was also used to extract individual "pulse lines" for processing.

This data was then windowed in the time domain. This is a standard computation performed in signal analysis before implementing a Fourier transform. The purpose of this step was to truncate the signal close to the start and at the endpoints, as leaving them intact would have led to the formation of sidelobe artefacts in the frequency domain. An example of a typical time domain window is presented in Figure 5.10. Four different windowing functions were tested to determine the most appropriate function to use: Gaussian, Hamming, Triangular, and Bartlett. Using a windowing function results in a decrease in amplitude of the sidelobes while increasing the FWHM of the main peak in the frequency space. A comparison was made to qualitatively determine which filter provided the best reduction in sidelobe amplitude while preserving the frequency resolution of the main peak.

Commented [AM27]: Added based on Kumar's comment

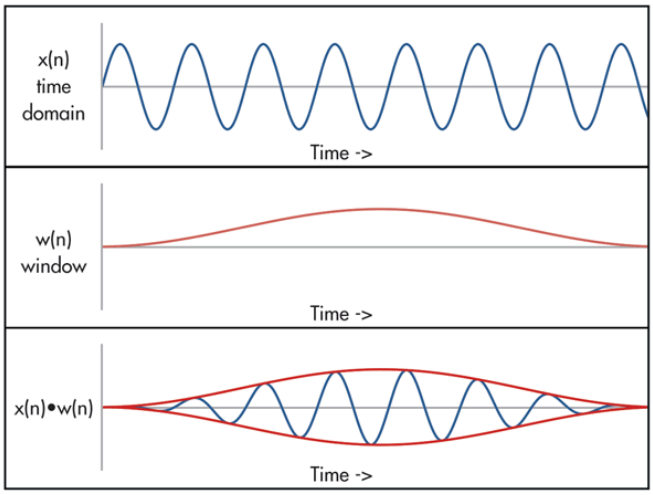

Figure 5.10: An example of a simple time domain windowing process. This procedure truncates the signal and reduces the effect of sidelobe artefacts in the frequency space.

The data then underwent a 2D discrete Fourier transform. As discussed previously, the 2D Fourier transform generates a frequency space bounded by the transmitted radiofrequency in MHz and the Doppler shift frequency in kHz. The spectrum forms in the shape of an ovular dispersion where the slope of the major axis is proportional to the velocity of the scatterers and the dispersion repeats infinitely in the frequency space. Once in the frequency domain, a low pass filter was applied on the data to remove the PRF. In traditional ultrasound processing architecture, the low pass filter would be applied prior to the signal demodulation, however the raw research mode data does not pass through any form of filtering prior to export so the filter had to be applied after importing to the programme. The reason why the filtering was carried out at this step and not earlier in the process is a matter of convenience as frequency-based filtering was trivial when the signal was converted to frequency space. Once the filter was applied, the Doppler spectra was

ready for multifrequency processing. The spectrum at this point resembled the illustration of a typical spectrum in Figure 5.11.

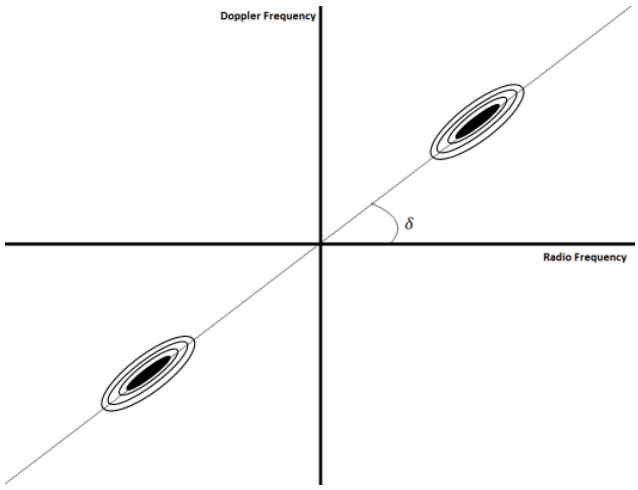

Figure 5.11: A typical Doppler spectrum produced by a 2D discrete Fourier transform after low pass filtering was used to remove the PRF.

The spectral scaling was then applied to the data. The purpose of this step was to "realign" the spectrum so that the integration would correctly sum the individual spectra. Previous experiments had been carried out to determine the bandwidth of a particular pulse for a number of transmission properties (see Chapter 3). Using the known bandwidth of the pulse, a scaling factor could be applied such that a frequency could be scaled according to the ratio f_{RF}/f_c. This process could be thought of as moving a spectrum of a given radiofrequency up or down proportionally to its value relative to the central transmitted frequency so that a horizontal integration would pass through all the spectra without broadening the velocity spectrum. The integration was then applied using the bandwidth of the pulse as the limits of integration. This produced a velocity spectrum that

represented the entire acquisition period, this was not a concern for steady flow but for pulsatile flow temporal resolution would have to be added.

5.2.2. Simulation Doppler data for algorithm validation

In order to fully validate each step of the newly developed technique, the algorithm was tested at different points. A block diagram of this procedure is included in Figure 5.12. The first validation point was testing the algorithm using simulated flow data and to this end a script was written in MATLAB to generate simple simulated flow data. The script was designed so that it could generate steady and pulsatile flow data and would output a matrix of IQ data which could be read by the MFUDSA algorithm.

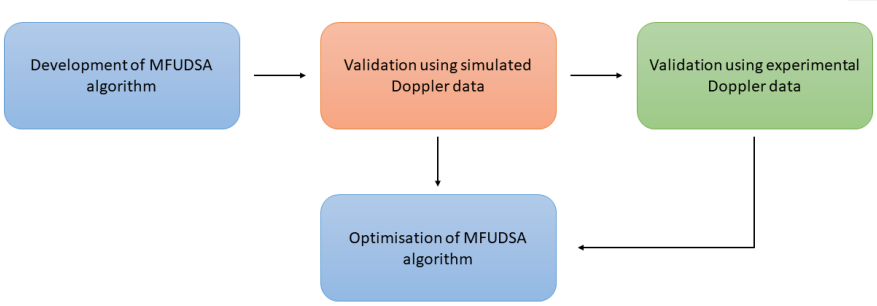

Figure 5.12: Validation steps of the MFUDSA algorithm

The resulting data contained only a single Doppler shift frequency (which could vary in time) which was not suitable for Multifrequency analysis. In order to introduce the extra data associated with a bandwidth of frequencies two for loops were constructed which would calculate the appropriate Doppler shift frequency for a range of frequencies in the pulse bandwidth and then superimpose the signals onto one another. Despite its relatively short length, this code required a considerable amount of memory and time to run. As such, the resulting simulated signal was only generated for one velocity setting and saved to avoid running this code if possible.

5.2.3. Experimental data

The second validation point was carried out using the raw Aixplorer Doppler data generated and acquired using an *in vitro* set-up utilising a set of flow phantoms, the design of which was specified in Chapter 3. These phantoms were connected to a magnetically driven cavity style pump head (Cole Parmer, Walden, UK) used to pump the blood mimicking fluid through the flow circuit coupled to a direct current servo motor (McLennan Servo Suppliers Ltd., Surrey, UK). The motor was driven by a servo amplifier (Aerotech Ltd, Berkshire, UK), multifunctional I/O board (National Instruments, Austin, TX, USA) and a computer controller program developed in LABVIEW (National Instruments, Austin, TX, USA) was used to output the required velocities (calibrated using timed weight collection). The BMF was degassed and was pumped through the phantoms and flow circuit for 1 hour prior to measurements to ensure no air bubbles remained.

In order for fully developed laminar flow to be present, the flow must follow a straight path for a certain distance known as the inlet length, L, defined as:

$$L = 0.04 * d * Re \tag{5.3}$$

where d is the diameter of the vessel, and Re is the Reynolds number defined as:

$$Re = \frac{\rho d v}{\eta} \tag{5.4}$$

where ρ is the density of the BMF, v is the mean velocity of the flow, and η is the viscosity of the BMF. Taking $\rho = 1.037$ g cm^{-3} and $\eta = 0.041$ g cm^{-1} s^{-1} for the BMF from previous work [108], and taking the mean velocity as half the maximum velocity, $v = 24$ cm s^{-1} with a diameter of $d = 0.7$ cm, this gives a required inlet length of $L = 11.90$ cm. To ensure

these conditions were met, the inlet length used was twice the minimum required inlet length; for all flow experiments the phantoms were set up to have an inlet length of 24 cm.

A flow resistor was connected to the outlet of the flow circuit to replicate the resistance of the vascular bed and thereby, damp out any reflections from the tubing connections. A steady flow velocity was specified at 30 cm s^{-1} and was determined to have a systematic uncertainty of ± 1.3 cm s^{-1}. Doppler data were acquired from the Aixplorer scanner with a range of transmission parameters to determine the optimal settings for the MFUDSA algorithm. The transmission parameters which can be controlled in research mode are: transmit frequency, pulse length (transducer half-cycle), PRF, and data length (number of frames). The depth could also be specified although this quantity was always minimised to reduce the data file size as much as possible.

5.2.4. Optimisation of MFUDSA algorithm

The performance of the MFUDSA algorithm could be optimized depending on the desired application and this was achieved through a number of factors, of which the transmission parameters played a key role. It was previously established that the best improvement in velocity resolution and SNR was achieved with a pulse length setting of 4 half cycles. Therefore, this value was used for all optimisation acquisitions. For each varying transmission parameter, experimental data was acquired using flow phantoms as described previously. The data was analysed in MATLAB. The values for transmit frequency tested were: 5 MHz, 5.6 MHz, 6.4 MHz, 7.5 MHz, 9.5 MHz, and 11.25 MHz, as these were the only transmission frequencies available for the SL15-4 transducer in research mode. In principle, it was expected that the higher the transmit frequency was, the better the velocity interrogation would be which would improve results. The bandwidth of the transmit pulse also depended on the transmit frequency, with higher

transmit frequencies having greater absolute bandwidths; however, the bandwidths were proportionally smaller compared to their transmit frequency. The PRF had a known effect on of velocity spectra. It was not expected to have an effect on the MFUDSA algorithm provided it was above the Nyquist threshold, but for completeness it was varied across the range of possible frequencies of the scanner (0.5 – 12 kHz). The data length was also varied across the total possible range (500 – 2000 data points). It is worth noting that, while not important for generating a single velocity output for steady flow, the data length is very important for generating time-varying sonograms and for variable velocities in general. This is because the total time of the acquisition is equal to the data length divided by the PRF which means that in order to resolve a full cardiac cycle the PRF must be decreased or the data length increased.

Commented [AM28]: Typo fixed

Another optimisation process was the windowing function as applied in the time domain. There were a variety of functions to choose from depending on the desired application and for the purposes of this optimisation, 4 functions were tested. The functions tested and their specific profile and features are outlined in Table 5.1. To test the effect of the windowing functions on the Doppler spectra, 5 datasets were acquired using a Doppler string phantom with a set maximum velocity of 10 cm s^{-1} so as to ensure there would be no spread in velocity and for each dataset, each windowing function was applied. The effect of the windowing function was taken as the amplitude of the first side lobe relative to the main lobe.

Table 5.1: Windowing functions and their respective profiles and features

Function	Approximate shape	Features
Gaussian	Gaussian	Based on the Gaussian distribution. The signal is truncated based on its position relative to the target section filtered.
Hamming	Gaussian	Similar to the Gaussian window but the coefficients are specified to specifically target the nearest sidelobe preferentially.
Triangular	Triangular	The signal is truncated linearly based on its position relative to the target section filtered.
Bartlett	Triangular	Similar to the triangular window but with preferential discrimination of the first sidelobe.

Once this optimisation procedure was completed, the performance of the MFUDSA algorithm was assessed using research data. A flow phantom was connected to the pump system as described previously and data was acquired for flow velocities of 10, 20, 30, 40, and 50 cm s^{-1} using the optimised parameters. The IQ data was then analysed using 1D Fourier analysis, 1D Fourier analysis incorporating Welch's method, and 2D Fourier analysis with the MFUDSA algorithm. For each method, the SNR and the FWHM of the main peak were measured.

Finally, the MFUDSA algorithm was modified to produce a sonogram as its output. This was achieved by splitting the total signal in time into a number of segments, where each segment would be treated as a separate signal by the algorithm. The resulting velocity spectra would then form the time points of the sonogram.

The sonogram was tested first with simulated data. Two simulated datasets were generated, the first featured a linearly increasing Doppler frequency corresponding to a velocity range from -20 cm s^{-1} to 20 cm s^{-1}. The second set of simulated data had the Doppler shift varying as a cosine wave with peak Doppler shifts corresponding to velocities of -40 cm s^{-1} to 40 cm s^{-1} and was simulated to feature the reflections of a bandwidth of transmitted frequencies to test the multifrequency analysis of the algorithm.

The sonogram function was then tested using real data acquired from a Doppler string phantom (CIRS, USA). A string phantom was used to eliminate the velocity gradient associated with a fluid flowing in a finite vessel so the sonogram could be tested in a simple environment prior to phantom testing. The string phantom was set with a pre-generated pulsatile waveform corresponding to paediatric umbilical blood flow. This waveform was selected as it had a peak velocity of 45 cm s^{-1} which closely resembles the renal artery peak velocity of 50 cm s^{-1}. The string phantom data was acquired in research mode with a transmit frequency of 5 MHz, a pulse length of 4 half cycles, a PRF of 4 KHz, and a data length of 2000.

Commented [AM29]: Added based on Kumar's comment

5.3. Results

5.3.1. Transmission parameters

The results for the investigation into the effect of transmit frequency are presented as boxplots in Figure 5.13, so that the range of velocity output can be visualised. As the transmit frequency increased, there was a slight increase in SNR which peaked at 5.6 MHz, followed by a steep decline in the frequencies above this level. The effect of PRF on the MFUDSA algorithm was also investigated and found to have no effect on the velocity output, other than affecting the scale of the Doppler frequency axis. A greater PRF resulted in the Doppler frequency axis lengthening corresponding to an increase in

the maximum detectable velocity according to the Nyquist criterion. The data length of the pulse did not have a detectable effect on the velocity output.

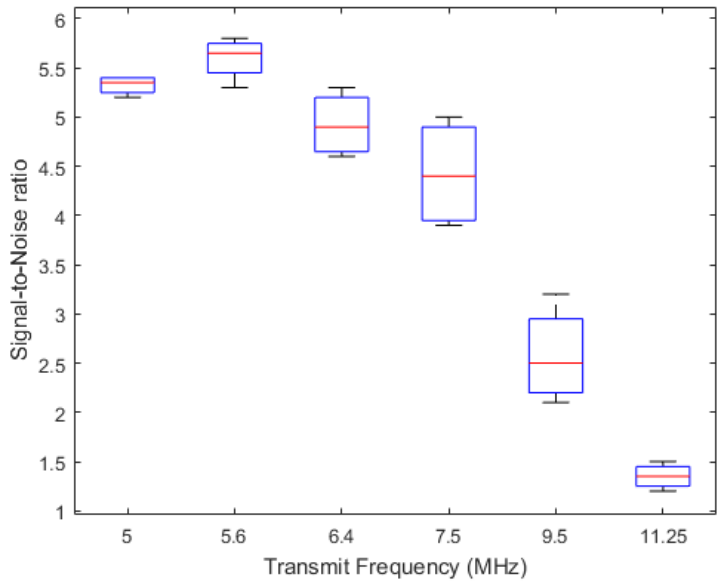

Figure 5.13: MFUDSA algorithm SNR with respect to transmit frequency

5.3.2. Windowing functions

The windows used for this analysis are presented in Figure 5.14. Each window was tested to determine its effect on the Doppler spectra. The results are included in Table 5.2.

The results demonstrated that while there is a significant decrease in sidelobe amplitude as the windowing functions are applied, there was a trade-off with decreasing velocity resolution as more aggressive windowing functions were applied.

Table 5.2: Results of the analysis of windowing functions effect on sidelobes

Function	First side lobe amplitude (dB)	Main peak FWHM (cm s^{-1})
No Window	-15 ± 2	0.76 ± 0.04
Gaussian	-53 ± 7	2.18 ± 0.06
Hamming	-38 ± 4	1.57 ± 0.06
Triangular	-30 ± 3	1.27 ± 0.05
Bartlett	-26 ± 2	1.21 ± 0.03

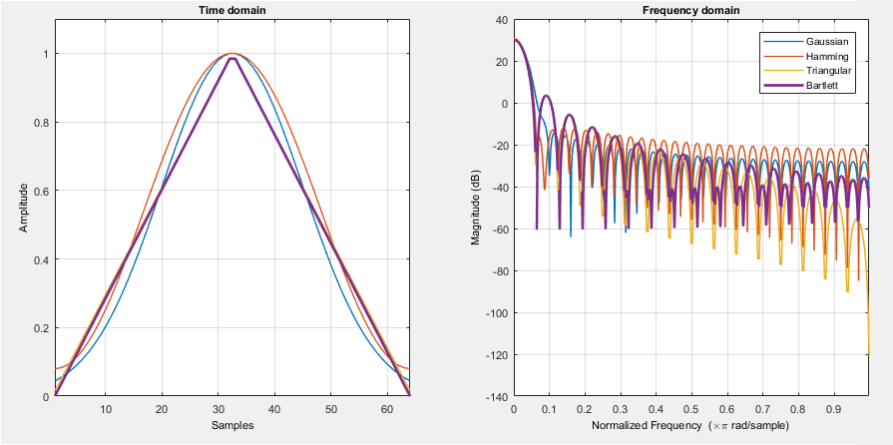

Figure 5.14: The windows used in this analysis

5.3.3. Performance of the optimised MFUDSA algorithm

Following the optimisation of the MFUDSA algorithm, the performance relative to other analysis methods was tested. An example of the typical output for this test is included in Figure 5.15. It was found that the overall improvement to SNR from the MFUDSA

algorithm compared to the 1D analysis approach was a factor of 6.21 ± 0.79 compared to the improvement from the Welch's method of a factor of 1.38 ± 0.65. It was also found that the overall reduction in the main peak FWHM (which was taken as a measure of the velocity resolution) was 1.26 ± 0.0014, compared to Welch's method which showed a typical reduction in velocity resolution by a factor of 1.04 ± 0.003 due to the spectral averaging it employs. The improvements in SNR and velocity resolution brought about by the MFUDSA algorithm were found to be independent of velocity and were tested for significance using a paired t-test ($p < 0.05$). The null hypothesis of the tests was that the improvement of the parameters was not significant and the alternative hypothesis was that the improvements were significant. For the improvement in SNR and velocity resolution, it was found that these results were statistically significant ($p = 0.0217$ and $p = 0.028$ respectively).

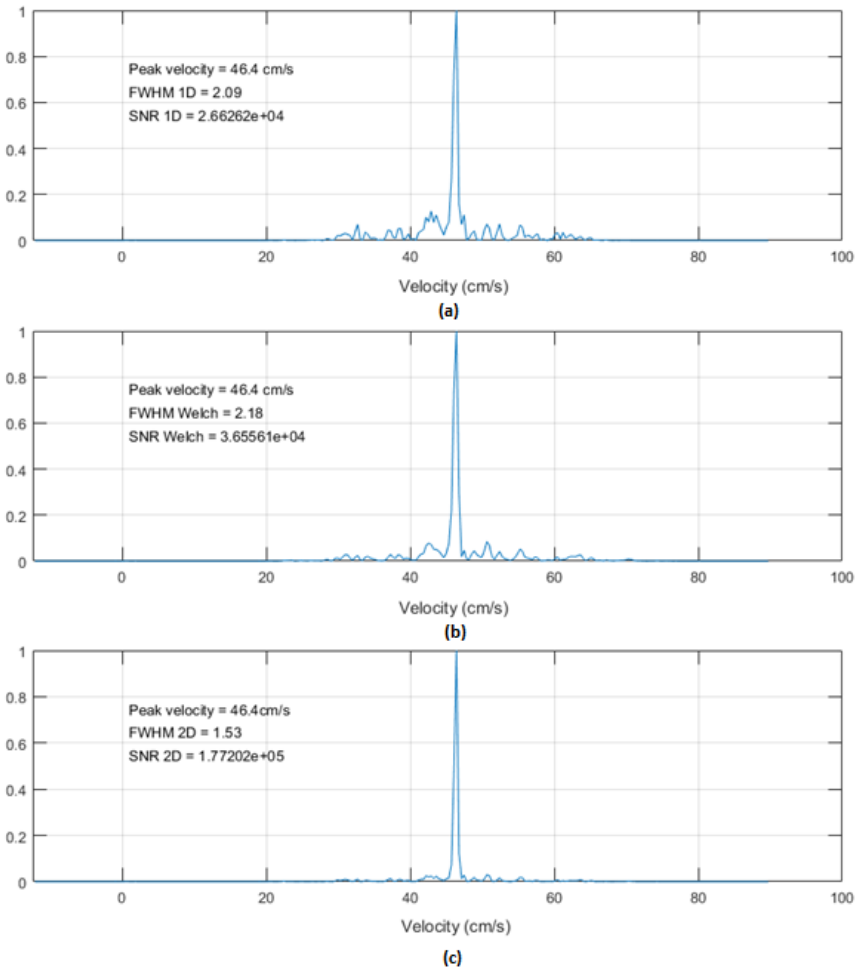

Figure 5.15: An example comparison between 1D Fourier analysis (a), 1D Fourier analysis using Welch's method (b), and MFUDSA analysis (c).

5.3.4. Generation of Doppler sonogram from velocity outputs of the MFUDSA algorithm

The simulated data was utilised to construct sonograms to test the algorithms ability to detect temporally varying velocity. The sonogram outputs for the linearly varying velocity and the cosine varying velocity data are presented in Figures 5.16 and Figure 5.17. Additionally, a sonogram was produced using the research data acquired from a Doppler string phantom with a paediatric umbilical waveform with peak velocity of 45 cm s^{-1}. The resulting sonogram is presented in Figure 5.18.

Figures 5.16 and Figure 5.17 show well produced Doppler spectra and clearly illustrated the time varying nature of the simulated data. Conversely, Figure 5.18 does not represent a coherent Doppler spectrum, likely due to the extreme limitation in data length imposed by the Aixplorer scanner. While the simulated data could have extremely long data lengths, the research mode data was limited to 2000 points which had to be budgeted between the Fourier transforms and the sonogram. By comparison, the sonogram in Figure 5.17 had a data length over 10 times greater than the maximum limit imposed by the Aixplorer. To verify this was the cause, another sonogram was made from simulated data with the data length limited to 2000 points. This sonogram is displayed in Figure 5.19. The sonogram displayed a similar level of incoherence as was seen in Figure 5.18. It can be more clearly seen in Figure 5.19 that at shorter data lengths, the Doppler spectra suffered from considerable aliasing and loss of velocity information. This seemed to confirm that when the data length is too small, a coherent sonogram cannot be generated.

Commented [AM30]: Fixed typo

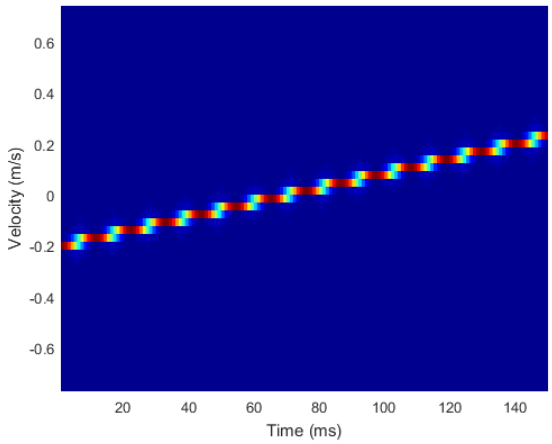

Figure 5.16: Sonogram made using linearly varying simulated Doppler data. The data length was 15000 and the PRF was 5 kHz.

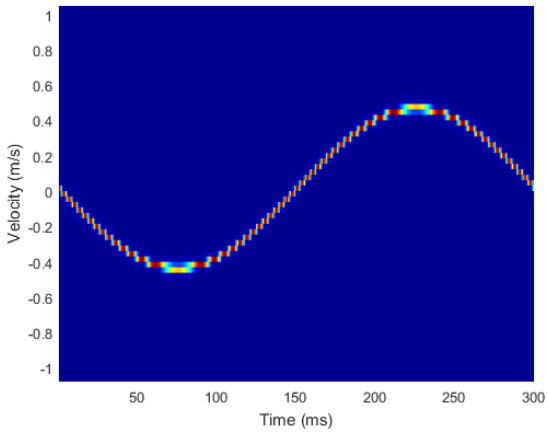

Figure 5.17: Sonogram made using cosine varying simulated Doppler data analysed with the MFUDSA algorithm. The data length was 21000 and the PRF was 7 kHz.

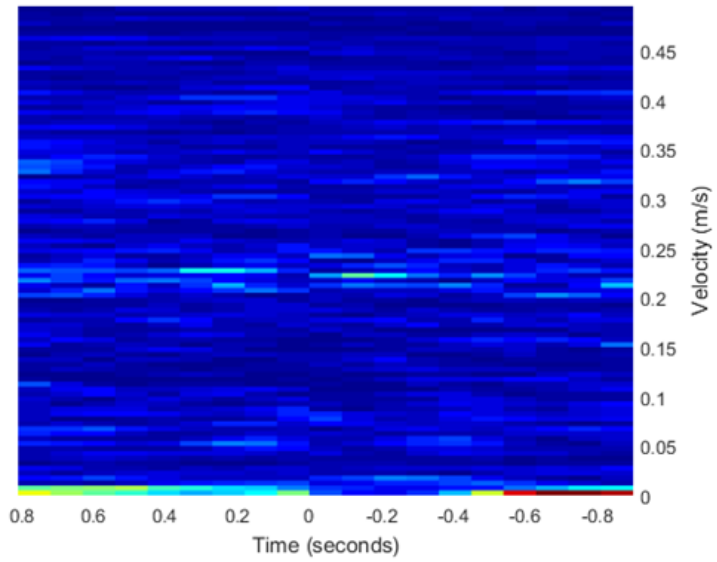

Figure 5.18: Sonogram made using research mode data. The data length was 2000 and the PRF was 4 kHz.

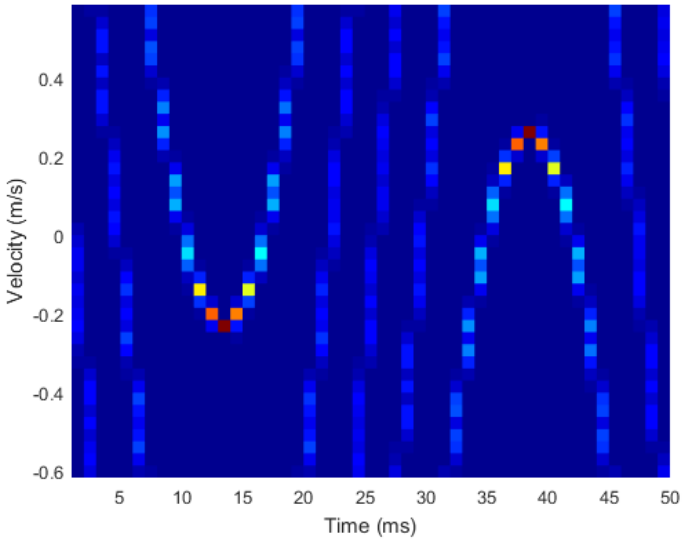

Figure 5.19: Sonogram made using cosine varying simulated Doppler data analysed with the MFUDSA algorithm. The data length was 2000 and the PRF was 4 kHz.

Commented [AM31]: Fixed typo.

5.4. Discussion

It was found that as the transmission frequency increased, the SNR of the MFUDSA algorithm outputs reached a peak at 5.6 MHz before rapidly falling off. As the frequency increased, so did the level of velocity interrogation. Furthermore, the pulse was increasingly attenuated by the phantom material to the point where the resulting spectrum was not separable from the background noise. Additionally, the higher transmit frequencies have been observed to feature broader frequency bandwidths leading to more Doppler spectra, which can be combined using the MFUDSA algorithm leading to a reduction in the spectral variance. This would indicate that the ideal frequency setting is one which is high enough to produce the gain in SNR associated with both additional velocity interrogation and greater application of the MFUDSA algorithm while not being

so high as to suffer from attenuation. This is similar to what was found by Loupas & Gill [7]. In their work on multifrequency Doppler, they propose a quality factor for the analysis, Q, defined as in Equation 5.5.

$$Q = \frac{f_c}{BW\sqrt{\ln(2)}} \tag{5.5}$$

Where f_c is the central transmitted frequency, and BW is the pulse bandwidth. It was found by Loupas & Gill that for a 1D Fourier analysis, the SNR of the output spectrum was independent of Q factor, while the 2D Fourier analysis exhibited an inverse relationship between the SNR and the Q factor. Based on these results, it would be more accurate to state that the ideal transmission frequency for use in the MFUDSA algorithm should be sufficiently low while providing the broadest possible bandwidth for analysis. Based on the results of this study, this value was taken to be 5.6 MHz.

The PRF and the data length of the pulse at first appeared not to be significant in the generation of Doppler spectra (provided the PRF was sufficient to avoid signal aliasing). However, it was found that they played an important role in the generation of sonograms. The sonogram could be thought of as a 2D matrix, where the rows corresponded to velocity data and the columns corresponded to different Fourier transforms representing different times. Therefore, the data length of a pulse was divided between these dimensions such that the product of the velocity spectrum length and the number of time points in the sonogram was less than the data length. In addition, the total time that the sonogram could cover was limited to the data length divided by the PRF. This meant that using the MFUDSA algorithm with the Aixplorer research mode to analyse pulsatile flow is effectively not possible with the current limitations imposed on the data length.

The windowing functions tested for use in the MFUDSA algorithm were selected on the basis of the least interference in the velocity resolution as possible. This was an important consideration because more aggressive suppression of sidelobes can result in spectral broadening. Of the windows tested, the Gaussian window had the largest effect on the reduction of sidelobes, it also had a correspondingly large effect on the velocity resolution. The Hamming, Triangular, and Bartlett windows had similar levels of sidelobe suppression. Of these, the Bartlett window had the smallest effect on the velocity resolution of the spectra. Based on these results, the Bartlett window was selected as the ideal windowing function due to its relatively large sidelobe suppression while maintaining as high a velocity resolution as possible. This was seen as an important quality as, ultimately, the WSS measurement would rely on a high degree of velocity resolution.

The performance of the MFUDSA algorithm was tested against the performance of a 1D Fourier analysis with and without applying Welch's method. It was found that the MFUDSA algorithm had an overall improvement relative to a standard 1D Fourier analysis of a factor of 6.21 ± 0.79 for SNR and an improvement of a factor of 1.04 ± 0.003 for the velocity resolution. Loupas & Gill found a relative improvement of between 70% and 360% for their multifrequency method relative to 1D Fourier analysis. A potential reason for the discrepancy in these results was the difference in bandwidth size. Loupas and Gill tested a series of pulse bandwidths for multifrequency analysis with the largest bandwidth being equal to half the corresponding transmit frequency. In this work, the bandwidth for the optimised transmission settings was equal to $0.72*f_t$. This means that for this analysis there was a larger range for integration in the frequency domain.

The code written for the generation of sonograms produced accurate time varying velocity representations when utilising simulated data, however, it was unable to generate a

coherent Doppler spectrum for the research data. This was determined to be due to a limitation of the Aixplorers research mode where the maximum data length of a single acquisition is 2000 points. This 2000 data point limit did not provide enough Doppler data to have both a coherent Doppler spectra for each time point in the sonogram and avoid aliasing of the velocity data. This is likely due to a hardware limitation where only a certain amount of data can be held in the buffer at once. As stated previously, despite not being long enough for a sonogram to be generated, a 2000 point raw IQ data file from the Aixplorer was very large (on the order of 1GB). In order to match the length of the simulated data, the maximum storage of the memory buffer on the Aixplorer would have to be an order of magnitude larger. A potential solution to this issue would be acquiring multiple acquisitions through the use of triggering. While it would not be possible to acquire each set of IQ data sequentially as the buffer needs to be emptied between acquisitions, it could be possible to acquire each dataset such that the acquisition time of each dataset is known and the trigger position is moved forward in the cardiac cycle by that time interval between acquisitions. However, if this procedure was implemented, it may still be difficult to concatenate the resulting data files as they are not in a standard text readable format. This means that it may be necessary to manually concatenate the data files or otherwise perform this step during analysis. This would put considerable strain on off-board processing hardware with at least 10GB of RAM required just to hold the data being concatenated. However, were this method built into the scanner itself, considerable memory savings could be made through the use of a similar object to the colour box used in colour flow imaging mode whereby the total area of the imaging region being processed could be limited to just the vessel and its immediate surroundings.

Other methods in the literature to achieve spectral improvements in Doppler measurements include the work carried out by Loupas et al. with 2-dimensional

Commented [AM32]: Rephrased based on Kumar's comment

autocorrelation [116,117]. This work followed on from the multifrequency Doppler work proposed in [7] which formed the basis of the MFUDSA algorithm, but unlike in the current study, which focuses on spectral Doppler, the further work by Loupas et al. focused on improvements in colour Doppler in the form of a 2D broadband autocorrelator.

The first study, [117], provided a comparison between the proposed 2D autocorrelator and two other established velocity estimators, namely; the conventional 1D autocorrelator and crosscorrelator. These techniques were taken as representative of the standard implementations of phase-domain velocity estimation techniques and time-domain velocity estimation techniques respectively. Loupas et al. describes the 1D autocorrelator as averaging the frequency estimates along the ensemble axis (i.e. slow time or the axis of the Fourier space associated with the PRF) while the 2D autocorrelator averages the frequency estimates along both the ensemble axis and the depth axis (i.e. fast time or the axis of the Fourier space associated with transmission frequency). Loupas et al. goes on to describe the crosscorrelator, which for some ideal cases (e.g. a single velocity component with a backscatter signal free of phase discontinuities) is mathematically equivalent to the 2D autocorrelator. However, the crosscorrelator differs from the autocorrelators in that it operates on successive RF returns and not the same signal line at a later time. The three techniques were compared using simulations to document differences caused by varying velocity spread, range gate length, ensemble length, noise level, and transmission bandwidth. The 1D autocorrelator had the poorest performance with extremely low precision and accuracy compared to the other techniques. While the 2D autocorrelator and the crosscorrelator behaved similarly under low-noise conditions, the 2D autocorrelator provided more precise results under high noise conditions.

The second study, [116], analysed the performance of the 2D autocorrelator relative to the 1D autocorrelator using experimentally derived data *in vitro*. However no comparison

was made to the crosscorrelator with these data as the procedure could not be implemented due to the system having an insufficient sampling rate to allow for time-domain RF processing. This study presented similar conclusions to the previous study, with the 2D autocorrelator provided increased accuracy and precision over the 1D autocorrelator. This was concluded to be due to the 2D autocorrelators ability to compensate for random fluctuations in the Doppler spectrum through spectral averaging.

5.5. Conclusion

This chapter focused on the optimisation of the various transmission parameters for the acquisitions in the Aixplorer research mode as well as their effect on the output of the MFUDSA algorithm. It was determined that the ideal transmission parameters are as follows: The transmit frequency had an optimal value of 5.6 MHz with a pulse length of 4 transducer half cycles, the optimal PRF was the minimum value possible without causing aliasing and the optimal data length was the maximum possible value.

Even when using these optimised settings, a time varying sonogram may not be possible to generate due to the extreme limitations in data length imposed by the Aixplorer. This was attributed to a hardware limitation and a potential solution was proposed through triggering, although this resolution was not without its own limitations. Despite this, the improvements made to the velocity output were considerable, with an improvement of a factor of 6.21 ± 0.79 for SNR and an improvement of a factor of 1.04 ± 0.003 for the velocity resolution. This indicated that the MFUDSA algorithm provided a significant reduction in spectral variance which resulted in higher precision for all velocity outputs.

The reason why the multifrequency Doppler approach was not adopted on a wide scale was mainly an issue of computational complexity. Loupas & Gill determined that for an N point fast Fourier transform, the time available for calculations to generate a real-time

display is N/PRF, this implies that each N point Fourier transform must be completed within 1/(2*PRF) seconds [7]. For small values of N this is reasonably achievable but rapidly becomes unreasonable on integrated circuits. When further developing this technique, Loupas et al. instead branched into autocorrelation methods to allow for real time display of a wide variety of Doppler conditions [116,117]. With new digital technology and the incredible processing speeds of cutting edge scanners, such as the Aixplorer, the computation of 2D Fourier analysis becomes trivial. Additionally, the advent of *UltraFast* scanning on the Aixplorer allows for full quantification of velocity in the entire imaging region instantaneously. This dramatically improves the potential of the MFUDSA algorithm for a wide variety of Doppler conditions but, in particular, it makes it an ideal candidate for the evaluation of WSS.

Chapter 6: Comprehensive flow experimentation

Some aspects of the methodology of this chapter have been accepted for publication in Physica Medica [119].

6.1. Introduction

This chapter describes the culmination of the previous chapters. The chapter will outline the use of the multifrequency *UltraFast* Doppler spectral analysis (MFUDSA) algorithm on a calibrated and optimised Aixplorer ultrasound scanner (Supersonic Imagine, France) for examining the wall shear stress (WSS) of a number of walled renal artery flow phantoms of varying vessel wall stiffness.

It has been previously discussed that using parabolic or Womersley profile assumptions to simplify the calculation of WSS can lead to errors due to the assumptions of axisymmetric and fully developed flow which is not necessarily the case for all vessels. In order to validate the proposed WSS calculation technique, it was tested in comparison to a standard pulsed wave (PW) Doppler approach and the parabolic estimation method outlined by Katritsis et al. [13]. Phantoms of three characteristic vessel stiffnesses were connected to a pump network containing blood mimicking fluid and examined using the three methods for measuring WSS.

Commented [AM33]: Fixed typo

Previous works in the literature have approached the problem of the validation of new diagnostic techniques in a number of ways. Methods which model the complex flow behaviour of blood in regions of irregular vessel geometry are common, typically utilising numerical predictions of scatterer behaviour through computational fluid dynamics [120]. Once established, the moving scatterers can be used to generate simulated backscattered ultrasound signals through software such as Field II [121,122]. Intuitively, the advantages of simulation are clear: the reduced time and financial costs over construction

of a complex experimental apparatus, the ease of alteration of test parameters, and the perfect reproducibility between experiments. A simulation cannot provide ground truths, however, as it limited by the assumptions and pre-existing experimental knowledge of the user. A comprehensive phantom study, while costly, can provide a level of certainty in its results which is absent in simulations. For this reason, when simulations are utilised, it is common to verify the results using experimental methods [123,124]. In the previous chapter, simulations were used to verify the effectiveness of the MFUDSA algorithm, however this chapter will explore the use of robust anatomically realistic flow phantoms to verify with certainty if the algorithm is capable of providing an improved measurement of WSS *in vitro*.

6.2. Methodology

6.2.1. Phantoms

The phantoms used for this work were produced using the methods outlined in Chapter 3. As stated previously, the most recent literature has estimated healthy arterial stiffness to be in the range of 34.9 – 83 kPa [65,67] and in the 116 – 751 kPa range for diseased vessels [66,67]. Three characteristic vessel stiffnesses were selected for the phantom production using the PVA-c freeze thaw cycling technique. These included: 60 kPa which corresponds to a healthy artery; 110 kPa which corresponds to an early disease state; and 320 kPa which corresponds to an intermediate diseased artery. A higher "late-stage" vessel stiffness was not selected as it was believed that the impact of the WSS technique largely lies in its potential as a screening tool prior to the formation of other disease indicators such as arterial stenoses.

Initially, 3 vessels were produced of each characteristic stiffness and embedded in TMM, yielding 9 phantoms. As the experiments progressed, the phantoms were found to burst

under extended use. As a result, a number of additional phantoms were produced to ensure a reserve was available in the case of phantom failure. In total, 5 additional phantoms were produced for the 110 kPa and 320 kPa stiffnesses and 3 additional phantoms were produced for the 60 kPa stiffness, bringing the total to 22 phantoms. The geometric accuracy was tested for each vessel produced. For each batch of PVA-c produced, in order to ensure the batch was within expectations, test samples were produced and set aside for acoustic and mechanical testing. The procedures for each of these tests are outlined in Chapter 3.

6.2.2. Pump network

The phantoms were connected to the pump network using PVC tubing and plastic couplers. The pump network was perfused with blood mimicking fluid and driven as described in Chapter 2. As described previously, the pump head was controlled using a custom programme written in LABVIEW (National Instruments, Austin, TX, USA). This code was modified to allow for custom waveforms to be inserted in place of a single constant voltage, allowing for a transition from steady flow to pulsatile flow. The waveform used in pulsatile flow experiments was recorded using Doppler ultrasound from a healthy volunteer and had a corresponding peak systolic centreline velocity of 48 cm s^{-1}. When used in steady flow mode, the pump was set to a constant voltage corresponding to a continuous centreline flow rate of 50 cm s^{-1}.

In order for fully developed laminar flow to be present, the flow must follow a straight path for a certain distance known as the inlet length, L, defined in Equation 5.3. As discussed previously, to ensure these conditions were met, the inlet length was set to 24 cm for all flow experiments. Data was acquired for steady state and pulsatile flow regimes, which was necessary as the MFUDSA algorithm was incapable of generating a sonogram with research data due to the data point length limit of the Aixplorer scanner,

as described in Chapter 4. This meant that the MFUDSA algorithm could be used to examine constant flow velocities but not time-varying flow.

6.2.3. Data collection

The data required to perform a comparative analysis between the three techniques to be tested was collected using the Aixplorer ultrasound scanner (Supersonic Imagine, France). For the steady flow regime, 3 forms of data were taken. Standard PW Doppler data was acquired using range gates to quantify the velocity profile, *UltraFast* data using on-board processing and research mode *UltraFast* data which could be used for the MFUDSA algorithm. For the pulsatile flow regime, the same data was taken with the exception of the research mode data which could not be used, as previously stated.

For each form of data acquisition, two regions of interest were examined, the so-called "linear" region and the "curvature" region, which are illustrated in Figure 6.1. These two regions were out of plane with each other and, thus, could not be imaged simultaneously, it was therefore necessary to reposition the transducer between acquisitions to record all the velocities in both regions. The replacement of the transducer was done only once per dataset, to reduce set up errors, carried out according to the procedure outlined in Chapter 2.

A total of 75 datasets were acquired, 25 acquired for each vessel stiffness, as outlined in Table 6.1. Each dataset was analysed individually.

Table 6.1: Number of flow datasets acquired for WSS analysis for each vessel

Data type	Steady flow	Pulsatile flow
PW Doppler	5	5
UltraFast Doppler (standard)	5	5
Ultrafast Doppler (research)	5	n/a*

* Analysis of *UltraFast* data in research mode was not possible due to the data length limit of the research mode buffer

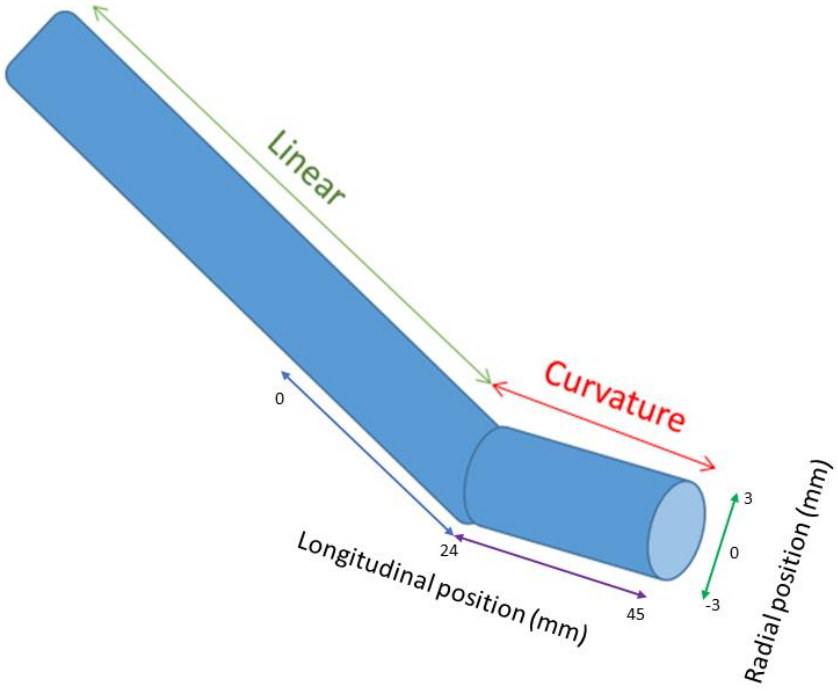

Figure 6.1: The "linear" and "curvature" regions of interest and the velocity measurement positions of the vessels

6.2.4. Analysis

The Aixplorer produces 2 different types of datasets for each acquisition. These include the standard imaging mode data and the research mode data. In this work, data analysis was carried out on each dataset with an additional post processing step required for the analysis of the research mode data. The research mode data required additional post processing to determine the velocities whereas the standard mode data was already in the form of blood velocities. For the research mode data, the MFUDSA algorithm was applied with a velocity spectrum produced for each point in the vessel. A flow chart of the typical data analysis procedure is given in Figure 6.2. Following this step, all data could be treated identically.

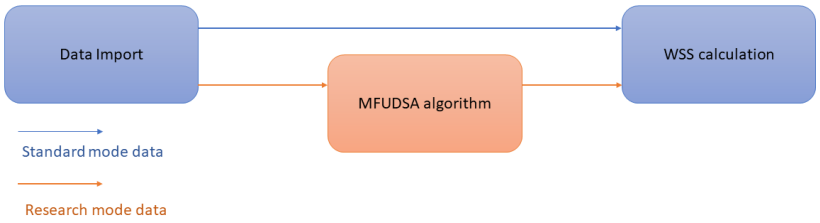

Figure 6.2: Flowchart of the data analysis procedure for standard and research mode Aixplorer data.

The velocity data were loaded into MATLAB (Mathworks, USA) as matrices where the columns were the radial co-ordinates of the vessel and the rows were the longitudinal co-ordinates. For the standard imaging mode data, the velocity at each matrix element was the average velocity recorded at the point for five points in the Doppler spectrum (in the case of pulsatile flow, these points were all peak systolic velocities), for the research mode data, the velocity displayed at each element was time averaged over the entire acquisition time by utilising the entire time interval in the Fourier analysis. These matrices could be

outputted in the form of velocity maps of the vessel for qualitative checks; however they did not provide direct quantitative data until further analysis was performed.

At this point, the parabolic WSS measurement could be made using the centreline velocities of the velocity map matrices according to Equation 2.4. The rows of the velocity map matrices were then analysed using the MATLAB in-built curve fitting tool with a 2^{nd} order polynomial fit. The output of this step was a series of equations corresponding to the velocity flow profile at each longitudinal position in the vessel. Each equation was differentiated using the symbolic differentiation function in MATLAB to get an expression for the gradient of the velocity profile. This gradient could be evaluated at each side of the vessel for two expressions of the wall shear rate, which was multiplied by the viscosity of the BMF to produce the WSS measurement. This meant that the parabolic WSS estimation method yielded one measurement for each longitudinal position while each other method yielded two measurements, one for each vessel wall.

The WSS were analysed for the linear and curvature regions of interest with the expectation that flow disturbances would change the behaviour of the WSS in and after the curvature region. An area of particular interest was a position approximately 10 mm distal to the curvature which has been noted as the region where 60% of renal artery stenoses form [125]. For each vessel stiffness value and WSS estimation technique a graph of WSS with respect to longitudinal vessel position was produced. A sample value was taken at the same vessel position for each dataset, at the position of stenosis formation 10 mm distal to the vessel curvature. The WSS values at this position was extracted from each dataset and collated. This allowed the WSS values to be averaged across all the datasets of each estimation technique. These WSS values were compared using a boxplot, which allowed for delineation between vessel stiffnesses for each WSS estimation technique. Finally, for each estimation technique the differences in WSS values between

the three vessel stiffness were analysed using a paired t-test. First a comparison between the low (60 kPa) and intermediate (110 kPa) vessel stiffnesses and then a comparison between the low (60 kPa) and high (320 kPa) vessel stiffnesses. For each test, the null hypothesis was that there was no significant difference in WSS values as the vessel stiffness increased and the alterative hypothesis was that there was a detectable difference in WSS values as the vessel stiffness increased.

The WSS values were analysed to calculate the sensitivity, specificity and accuracy of each technique using the following formulae:

$$Sens = \frac{a}{a+b} \tag{5.3}$$

$$Spec = \frac{d}{c+d} \tag{5.4}$$

$$Acc = \frac{a+d}{a+b+c+d} \tag{5.5}$$

where *Sens*, *Spec*, and *Acc* are the sensitivity, specificity, and accuracy respectively, a is the true positive rate, b is the false negative rate, c is the false positive rate, and d is the true negative rate. For the purposes of this analysis, the 60 kPa vessel was considered to be healthy, the 110kPa vessel was considered to be in a pre-disease state, and the 320 kPa vessel was considered to be in a diseased state. The cut off thresholds for the detection rates are given in Table 6.2. It was decided that the threshold of 0.4 Pa would be used for a fully diseased state, while a threshold of 1.0 Pa would indicate the presence of disease and 3.0 Pa would indicate its absence based on values recorded in the literature [27,33].

Table 6.2: Specifications of diagnostic detection rate thresholds

	WSS Value
True positive (320 kPa detected as diseased)	≤ 0.4 Pa
False negative (320 kPa not detected as disease)	≥ 0.4 Pa
False positive (110 kPa detected as diseased)	≤ 1.0 Pa
False positive (60 kPa detected as diseased)	≤ 3.0 Pa
True negative (110 kPa detected as not diseased)	≥ 1.0 Pa
True negative (60 kPa detected as not diseased)	≥ 3.0 Pa

6.3. Results

The results from the range of experiments completed are represented graphically in the proceeding section. Figure 6.3 shows an example velocity map matrix assembled from sequentially moving the Doppler range gate in PW mode to acquire a map of velocities. Conversely, Figure 6.4 shows an example velocity map assembled for the same data using a single *UltraFast* acquisition in research mode. Note that in Figure 6.4 there is an approximate factor of 5 increase in radial resolution. This increase is due to the IQ data used in the MFUDSA algorithm which has a finer degree of resolution than the Doppler range gate (0.1mm compared to 1mm).

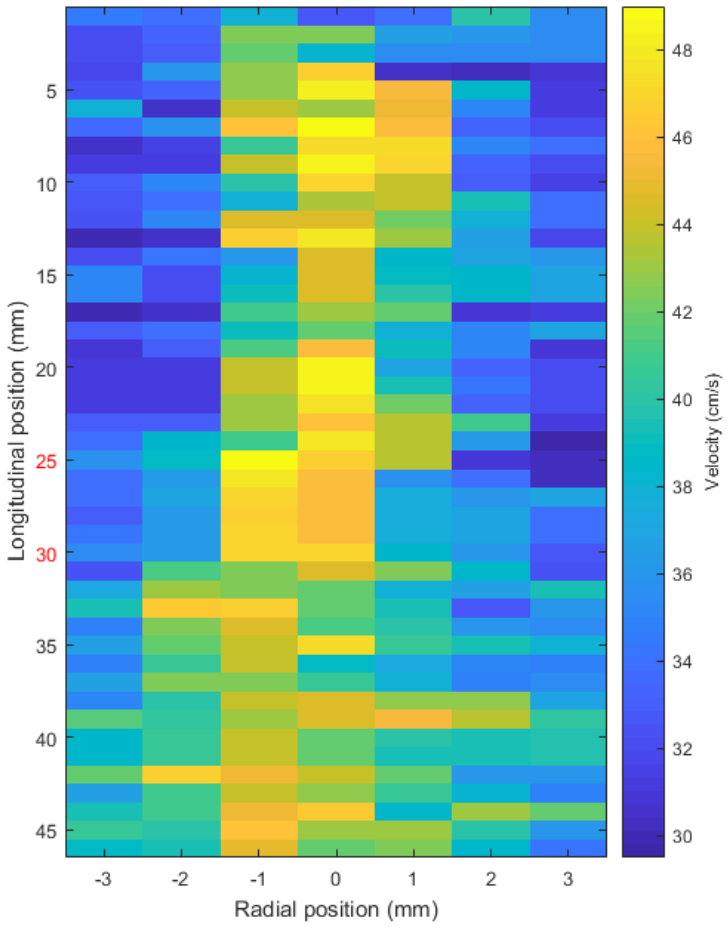

Figure 6.3: Example velocity map assembled using velocities recorded in PW mode by sequentially moving the Doppler range gate (± 0.3 cm s^{-1}). The vessel curvature extended from the longitudinal position 24 – 30 mm which is indicated in red on the y-axis.

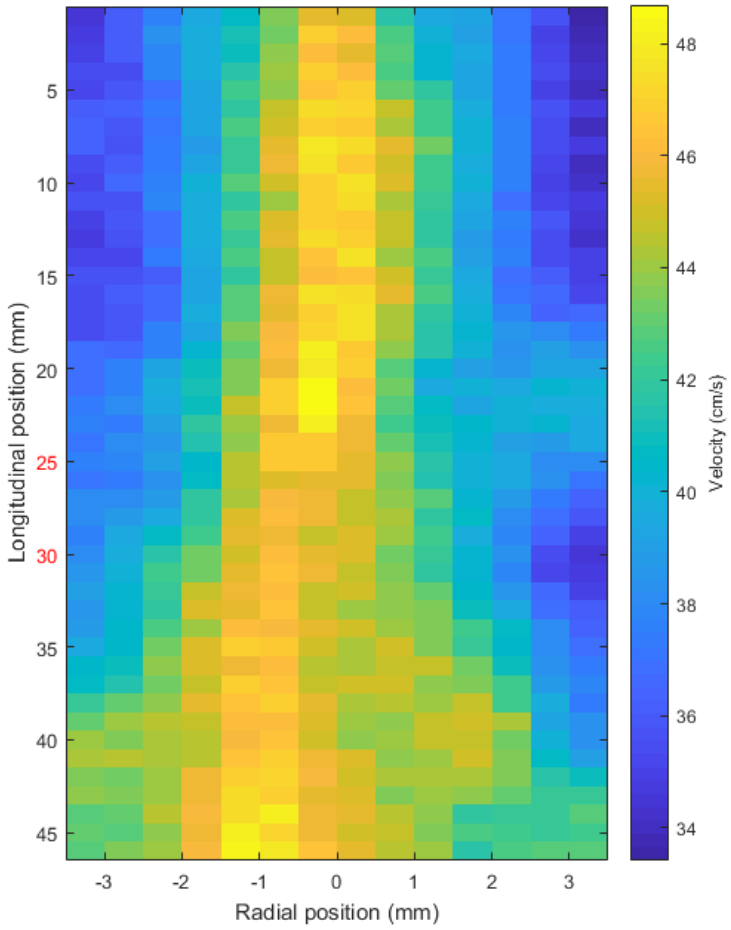

Figure 6.4: Example velocity map produced using exported IQ data in with the MFUDSA algorithm (± 0.14 cm s^{-1}). The vessel curvature extended from the longitudinal position 24 – 30 mm which is indicated in red on the y-axis.

Using these velocity matrices, a WSS value could be calculated at each longitudinal position in the vessel. Figures 6.5 – 6.8 show examples of the WSS calculated for a single

high stiffness dataset using the each of the techniques for the steady flow regime. The error bars in these figures represent 1 standard deviation of WSS variation between different data acquisitions for the same vessel stiffness. For each WSS curve, there is a section of relatively stable WSS corresponding to the linear region of the vessel, followed by a steep decline in WSS values at the curvature region. It is worth noting that while the curves all demonstrated a similar trend, the parabolic estimation technique consistently overestimated the WSS relative to the other techniques, by as much as a factor of 3.5.

The area of particular interest for examining WSS, as mentioned earlier, is the point approximately 10 mm distal to the vessel curvature as indicated by the magenta dashed lines in Figure 6.5 – 6.8. To evaluate this region completely, a sample of WSS values from a range of longitudinal positions (35 mm – 45 mm) were taken. These WSS values were saved for each dataset and values of equivalent vessel stiffness and WSS estimation technique were grouped together. Using these data, a series of boxplots were produced which showed the concentration of WSS at this location in the vessel with respect to vessel stiffness and estimation technique used. Figure 6.9 shows the boxplots for each of the techniques used in the steady flow regime and Figure 6.10 shows the boxplots for each of the techniques used in the pulsatile flow regimes.

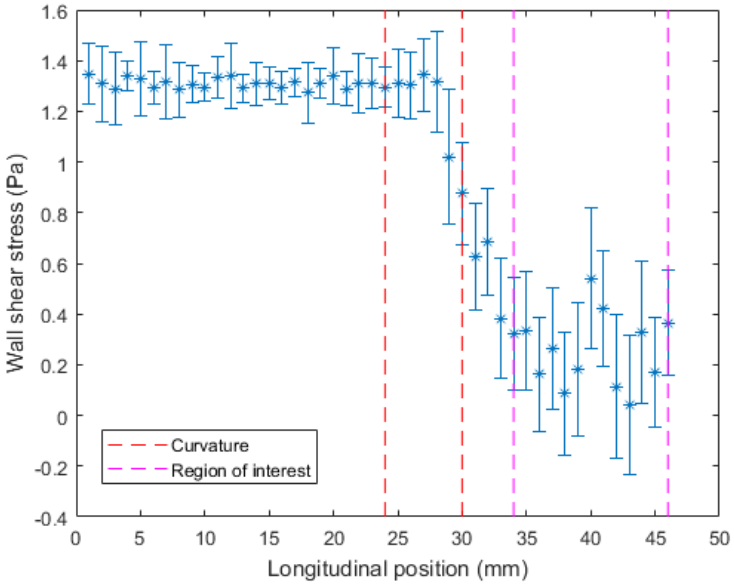

Figure 6.5: Example WSS curve using a PW velocity map

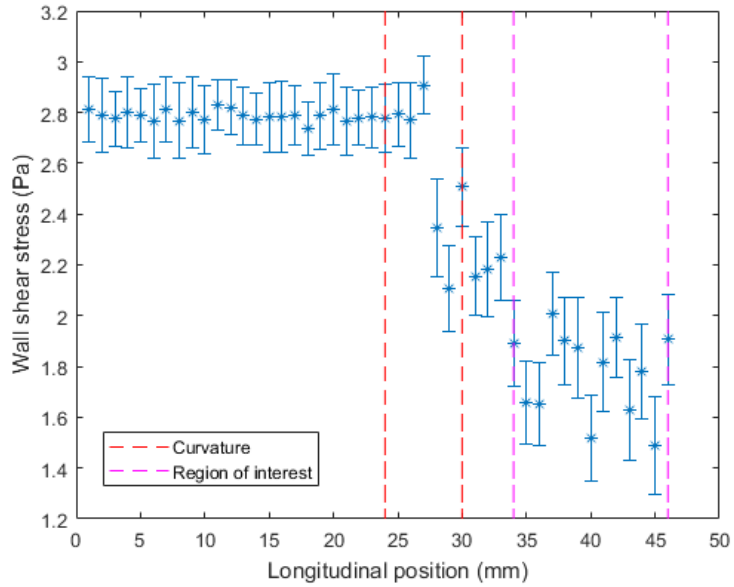

Figure 6.6: Example WSS curve using a parabolic velocity map

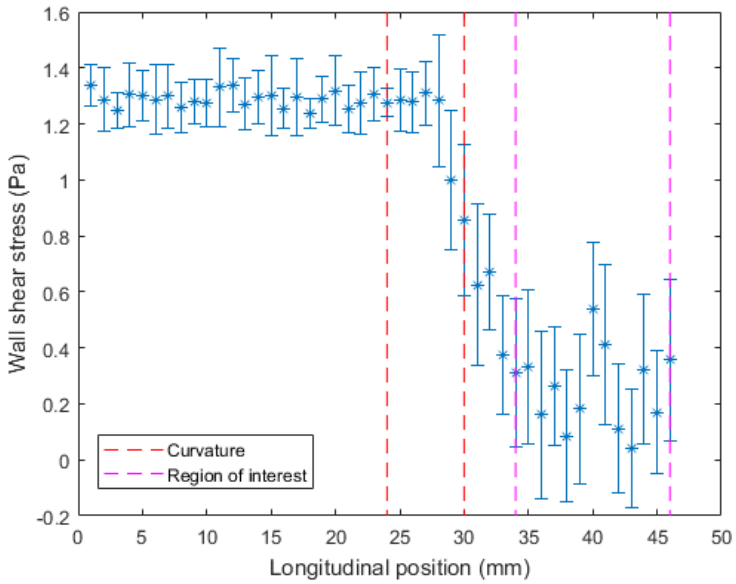

Figure 6.7: Example WSS curve using an* UltraFast *velocity map in diagnostic imaging mode

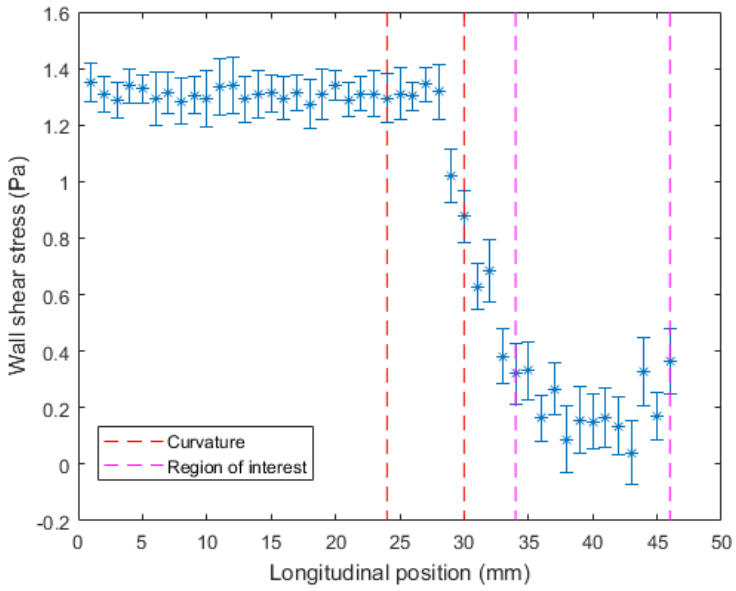

Figure 6.8: Example WSS curve using an MFUDSA velocity map in research imaging mode

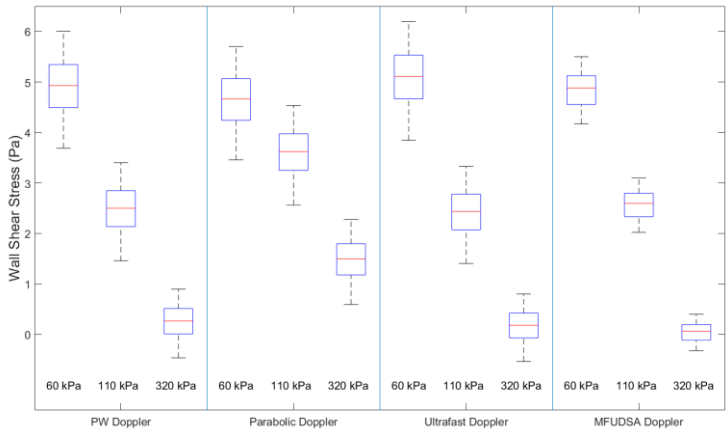

Figure 6.9: Boxplots of WSS values for a range of vessel stiffnesses in the steady flow regime grouped by estimation technique.

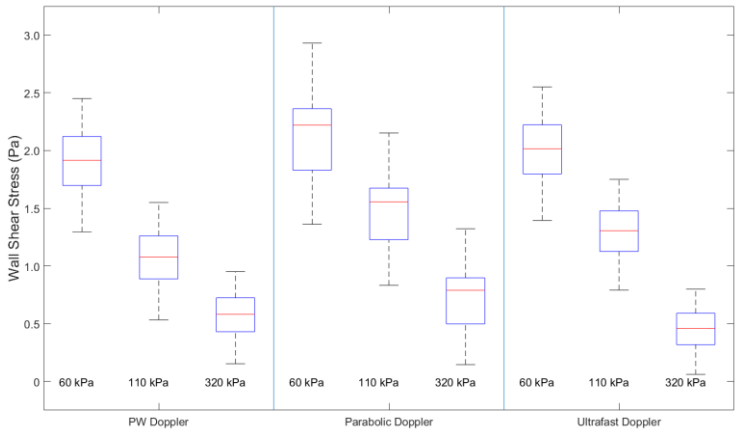

Figure 6.10: Boxplots of WSS values for a range of vessel stiffnesses in the pulsatile flow regime grouped by estimation technique.

Figure 6.9 shows that for each estimation technique there was a general trend of decreasing WSS with increasing vessel stiffness. The values were tested using a paired t-test to determine if the change in WSS was significant. The results of this test for each technique are presented in Table 6.3. The results indicated that for each technique investigated, there was a significant change in WSS values as the vessel stiffness increased with one exception, namely the parabolic estimation method for the comparison between low and medium stiffnesses. While the majority exhibited significant changes, the largest degree of separability was noted for the MFUDSA algorithm which showed strong performance at determining the precise changes in WSS which were detectable as the vessel stiffness increased which also resulted in reduced uncertainty in the measurement.

Table 6.3: Results of the paired t-tests into the significance of the change in WSS with respect to vessel stiffness for each estimation technique (steady flow)

Estimation technique	P-value	
	Low to medium stiffness	Low to high stiffness
PW Doppler	0.045	0.032
Parabolic Doppler	0.161	0.041
UltraFast Doppler (standard)	0.051	0.039
MFUDSA Doppler (research)	0.003	0.001

Figure 6.10 shows a similar trend across the estimation techniques for pulsatile flow as Figure 6.9 shows for steady flow, with a clear downward trend in WSS as the vessel stiffness increases. There are two important distinctions, however. Firstly, the maximum values of WSS for the lowest vessel stiffnesses in Figure 6.10 are less than half the observed maximum WSS values in Figure 6.9, likely indicating that the flow does not reach a fully parabolic profile for the pulsatile flow regime, resulting in a flatter velocity profile and a lower WSS value. The second feature of note in Figure 6.10 is that the WSS values seem qualitatively less separable than the values in Figure 6.9. To investigate this, these values were also subject to a series of paired t-tests to determine the significance of the decrease in WSS with increasing vessel stiffness. The results of these t-tests are presented in Table 6.4.

Table 6.4: Results of the paired t-tests into the significance of the change in WSS with respect to vessel stiffness for each estimation technique (pulsatile flow)

Estimation technique	P-value	
	Low to medium stiffness	Low to high stiffness
PW Doppler	0.084	0.041
Parabolic Doppler	0.201	0.062
UltraFast Doppler	0.097	0.032

These results show that, unlike Table 6.3, in the pulsatile flow regime, there was no significant difference detectable between the low and medium vessel stiffnesses. Although both PW Doppler and *UltraFast* Doppler were suggestive of significance with p-values only marginally above the 0.05 significance threshold. This change in significance between techniques was likely due to the flow regime itself, with a pulsatile flow producing a more fluctuating flow profile. Of the three techniques, again parabolic proved the weakest technique as it was unable to detect a significant difference in WSS values between the low and high stiffness vessels while the other two techniques could. This is to be expected because, as stated previously, if the flow was not fully developed and parabolic that would necessarily disqualify the assumptions underpinning the parabolic estimation technique.

The WSS results were then tested using equations 5.3, 5.4, 5.5 to determine the sensitivity, specificity, and accuracy of each assessment technique. The results are included in Table 6.5.

Table 6.5: Sensitivity, specificity, and accuracy for each estimation technique for steady and pulsatile flow

Technique	Sensitivity	Specificity	Accuracy
PW Doppler			
Steady	60%	100%	87%
Pulsatile	40%	30%	33%
Parabolic Doppler			
Steady	20%	100%	73%
Pulsatile	20%	40%	33%
***UltraFast* Doppler**			
Steady	60%	100%	87%
Pulsatile	60%	40%	47%
MFUDSA Doppler			
Steady	80%	100%	93%

6.4. Discussion

The results of this work indicated that there is a clear, measurable difference in WSS values for different vessel wall stiffnesses corresponding to different stages of CVD. The first noticeable improvement of the MFUDSA algorithm over PW Doppler analysis is the improvement in the resolution of the generated velocity maps. This improvement can be seen in Figure 6.3 and Figure 6.4 which show example velocity maps generated using PW and MFUDSA data. In Figure 6.4 there is an increase in radial resolution by a factor of 5 over Figure 6.3. In principle, this degree of radial resolution is theoretically achievable in PW Doppler as the Doppler gate can be reduced to as low as 0.1 mm,

however this would not be achievable in practice as it would dramatically increase the scan time and would allow for the introduction of significant errors *in vivo* due to the respiratory motion of the patient. This is not a problem for *UltraFast* acquisitions however, as the full velocity information can be acquired near instantaneously in a single acquisition. The MFUDSA algorithm provided an additional advantage as it was possible to automate the process and achieve the same data at a considerably faster rate.

The values recorded at the region of interest for the low wall stiffness value of 60 kPa, analogous to values seen in healthy arteries, varied in the range 3.4 – 6.2 Pa for steady flow and 1.3 – 2.9 Pa for pulsatile flow. These values fall within the range of what is considered to be normal artery WSS as determined by Malek et al. [27] who stated that low risk WSS values in arteries cover the range of 1 – 7 Pa while at risk WSS values are in the range of -0.4 – 0.4 Pa. The values calculated by Malek et al. for atherosclerosis prone flow conditions are also in line with the values calculated in this study with a range of -0.8 – 0.9 Pa for steady flow and 0.1 – 0.6 Pa for pulsatile flow. The MFUDSA algorithm had significantly improved performance over the other techniques and if it is considered alone, the values recorded for the high stiffness vessel of -0.2 – 0.3 Pa lie precisely within the region of at risk WSS values reported by Malek et al.

Chatzizisis et al. [33] reported similar values of WSS for regions at risk of developing atherosclerosis to Malek et al., with WSS values above 3 Pa considered to be high and WSS $\leq$ 1 Pa considered to be low and at risk. Using this metric, the MFUDSA algorithm again performs well, clearly delineating the three stiffness levels with the low stiffness not at risk, the medium stiffness potentially 'at risk', and the high stiffness estimated to be at risk. By combining the values of WSS risk from Chatzizsis et al. and Malek et al. a metric for sensitivity, specificity, and accuracy could be developed based on the "worst-case" scenarios of each range of WSS values [27,33]. The results of this analysis are

included in Table 6.5. The results indicated that for the parabolic and *UltraFast* techniques, there was no difference in sensitivity between steady and pulsatile flow regimes, while there was a reduction in sensitivity for PW Doppler. The analysis also showed that there was a significant decrease in specificity for all techniques between steady and pulsatile flow regimes. This was likely due to the pulsatile regimes not presenting fully developed flow, which would result in lower overall WSS values which would result in an increased risk of false positives over fully developed parabolic flow. Out of all the techniques, the MFUDSA algorithm performed the best with a calculated sensitivity and specificity of 80% and 100% respectively. It is likely that had it been possible to test the MFUDSA algorithm in a pulsatile flow regime, a drop in specificity would have been observed as with the other techniques. Despite this, the value of sensitivity recorded indicates a high likelihood of detecting the presence of at risk WSS values in arteries. This can be compared with techniques utilised later in the disease progression such as techniques used to detect arterial stenosis. PW Doppler has been widely utilised to determine the presence of arterial stenosis based on the presence of disturbed flow caused by the narrowing of the vessel lumen. This assessment technique has had reported sensitivity of between 67% to 97% and specificity between 54% to 92% while the former gold standard technique for detecting renal arterial stenosis, DSA, reportedly had a sensitivity between 94% to 100% and a specificity of 65% to 97% [18,19,126–128]. Based on these reported values, the MFUDSA algorithm was calculated to have a sensitivity on par with the current gold standard in the assessment of arterial stenosis and a slightly reduced sensitivity compared to the former gold standard. However, the MFUDSA algorithm can be applied significantly earlier in the development of the disease as it doesn't require the presence of a stenosis, indicating its power as a diagnostic tool.

Commented [AM34]: Updated based on Kumar's comment

Commented [AM35]: Clarified based on Kumar's comment

Blake et al. [9] utilised a Womersley based estimation technique for wall shear rate in a number of vessel phantoms and a healthy volunteer. WSS can be calculated from the wall shear rate by multiplying by the dynamic viscosity of the fluid. Blake et al. did not state the dynamic viscosity of the BMF used in this phantom study, but did mention the kinematic viscosity (3.3 $mm^2 s^{-1}$) and the density (1033 $kg m^{-3}$). These values can be used to calculate the dynamic viscosity as 3.4 x 10^{-3} Pa s. Using this value, the WSR results reported for the study can be converted to WSS values. Doing this, the average peak WSS value is given for each artery in Table 6.6.

Table 6.6: Average peak WSS values calculated from wall shear rates measured by Blake et al.[9] ***(units: Pa).***

Artery	Phantom	Human
Brachial	4.08	4.76
Carotid	2.89	4.08
Femoral	2.72	2.72

These results are in excellent agreement with the previously discussed literature and the results of the present work, indicating that healthy arteries seem to display characteristic WSS values within the 1 – 6 Pa range.

It can be seen in these results that the assumptions inherent in the parabolic estimation technique appear to break down for more complex flow regimes, Figure 6.6 shows that the parabolic method consistently overestimated WSS at all points in the vessel. While examining the region of interest 10 mm distal to the curvature, the parabolic method miscategorised high stiffness vessels as not being high risk for atherosclerosis formation and provided less clear information into the state of the disease to the other techniques

utilised. Parabolic methods may be useful in other WSS related assessments such as detected arterial stenosis which results in significantly increased WSS [119].

The MFUDSA algorithm consistently outperformed the other techniques assessed with the highest degree of significance detected and clearly delineating each of the vessel stiffnesses into the appropriate categories of disease progression. As discussed in Chapter 4, it was not possible to perform an assessment of the performance of the MFUDSA algorithm in the pulsatile flow regime due to limits on the Aixplorer scanner's research data buffer size. It is likely that a similar improvement to the PW measurements would be demonstrated in the pulsatile flow regime when using the MFUDSA algorithm as in the steady flow regime, allowing for a more precise measurement to be made while significantly decreasing the scan time and lessening the influence of user proficiency as the system can be made to be highly automated.

6.5. Conclusion

This purpose of this chapter was to assess each of the potential WSS estimation techniques under as ideal insonation conditions as possible to allow for a direct comparison in performance between the techniques. The results indicated, that the PW Doppler imaging mode, which would constitute the "traditional" method to determine WSS in ultrasound, performed within expectations and was able to successfully delineate the different vessel stiffnesses used.

The *UltraFast* Doppler mode behaved similarly to the PW Doppler mode, with no significant improvement in assessment accuracy or precision. However, the sensitivity and specificity of the *UltraFast* mode was increased over the PW Doppler mode for pulsatile flow. This was considered a significant improvement as the *UltraFast* mode can acquire the same velocity information as the PW Doppler mode in a fraction of the time

and with much less reliance of operator skill, as the transducer would not have to be held still for long periods of time and the relative short plane wave insonation would limit the effect that respiratory and abdominal movement would have on the results.

The main benefit to using the parabolic or Womersley assumptions is to decrease the scanning time over traditional PW Doppler methods; although this comes at the cost of accuracy. With the advent of *UltraFast* scanning technologies, this trade off may no longer be necessary as the *UltraFast* mode could complete an insonation faster than either estimation method could be performed when using PW Doppler. The *UltraFast* data would be used to calculate the WSS using a parabolic of Womersley method but as this data would need to be analysed off-line from the scanner the increased accuracy of utilising the full velocity profile may be worth the additional time this analysis would take.

Finally, the MFUDSA algorithm performed exceptionally well in the steady flow experiments, showing the greatest level of significance in the differences between WSS values detected at the stenosis formation region. The technique was also more precise, with the highest measured sensitivity and accuracy of any technique. This indicated that the MFUDSA algorithm provided the best method for the assessment of WSS among the techniques examined, although it could not be compared in terms of performance for the pulsatile flow regime as previously stated. This could potentially be rectified by moving the MFUDSA algorithm to an on-board post-processing procedure. This would allow the large amounts of unutilised IQ data to be discarded by only focusing on a user specified region of interest, similar to a colour box used in colour flow imaging. This means that significantly less space would need to be used on the data buffer and allow for a longer acquisition time and, potentially, the generation of a coherent sonogram necessary for determining time-varying WSS.

Despite the limitation of being unable to test the MFUDSA algorithm in pulsatile mode, it displayed a high level of diagnostic sensitivity, comparable to methods used in the assessment of CVD at a much later disease stage. This indicated that the MFUDSA algorithm could provide the same level of diagnostic power as methods currently utilised in CVD assessment while having the advantage that it could be applied much earlier, prior to any stenosis formation. This is of significant clinical benefit as it could provide dramatically safer treatment options for patients who would otherwise have to undergo surgery when the disease has progressed further.

Chapter 7: Conclusions and Suggestions for Future Work

A comprehensive Doppler ultrasound analysis procedure combined with an *UltraFast* acquisition modality was developed in the form of the novel MFUDSA algorithm. The aim of this thesis was to develop this algorithm and evaluate it using a robust, anatomically realistic phantom testbed with the novel capability of precisely mimicking different stages in the progression of CVD in the form of vessel stiffness.

This involved the following implementation steps: firstly, the Aixplorer scanner was characterised in terms of its transmission parameters and display capabilities. This was important to ensure that the information recorded from the scanner was accurate to a high degree of reproducibility, namely that the system was capable of reliably displaying the full range of Doppler echoes expected from the study as well as correcting the errors associated with intrinsic spectral broadening and misalignment of the transducer. Secondly, a geometrically reproducible, anatomically realistic phantom testbed was developed for use in the flow experiments. The phantom constituents were acoustically and mechanically characterised to a high degree of precision and the vessel design was shown to be highly geometrically consistent. Thirdly, the MFUDSA algorithm was

Commented [AM36]: Fixed typo

developed which combined the multifrequency analysis procedure with the raw *UltraFast* data acquired from the Aixplorer system. This required the development of custom code in MATLAB (Mathworks, USA) which could accept IQ data in the form exported from the Aixplorer scanner and perform the necessary analysis procedures to implement spectral averaging across the entire transmitted frequency bandwidth. Finally, a series of comprehensive flow experiments were carried out to test the effectiveness of the MFUDSA algorithm against other commonly used techniques.

7.1. General conclusions

Chapter 3 outlined the steps taken for calibration and characterisation of the Aixplorer system and the flow network. The most important conclusion from this work was based on the characterisation of the transmitted frequency bandwidth of the SL15-4 transducer which concluded that the optimal transducer half cycle for use with the MFUDSA algorithm was 4 half cycles. This allowed for the greatest improvement in velocity resolution while simultaneously providing a sufficient increase in SNR. Another important conclusion of this chapter was the finding that the ISB cancellation method proposed by Osmanski et al. [1] was highly effective when used in conjunction with the MFUDSA algorithm and provided a reduction in ISB by an approximate factor of 7. This meant that the cancellation method could be applied to all future MFUDSA velocity estimations, greatly improving the precision of the velocity profiles produced. The calibration and characterisation of ultrasound systems is an often overlooked and underreported aspect of quantitative ultrasound research, as evidenced by the dearth of literature on quantification of the Doppler dynamic range which was calculated to be 16.7 ± 0.28 dB for the Aixplorer system.

Commented [AM37]: Fixed typo

Chapter 4 outlined the protocol for the construction of the anatomically realistic flow phantoms. The chapter concluded that a consistent formulation of PVA-c that did not suffer from sedimentation was achievable with the utilisation of silicone emulsion as an attenuator and aluminium oxide particles of different sizes to act as scatterers. Further, an important conclusion of this chapter was that there was a measured correlation between the Young's modulus of the vessel sample geometry and the dumbbell testing sample geometry specified by ISO 37 [105]. While this may seem intuitive, the literature suggests that assuming this would not have been prudent as the elastic properties of PVA-c depend highly on the rate of thawing which in turn is proportional to its SA:V. The chapter discusses the potential implications of using the cylindrical samples specified by ISO 7743 [104] as well as directly comparing the SA:Vs of the cylindrical and dumbbell test samples to those of the vessel samples themselves.

Chapter 5 detailed the development and optimisation of the MFUDSA algorithm for use in conjunction with the flow network and the Aixplorer system. The most important conclusion of this chapter was that despite its potential usefulness as a diagnostic technique, the MFUDSA algorithm could not be applied to pulsatile flow data. This was due to the memory size limit on the Aixplorer buffer which limited the total number of data points which could be exported in a single insonation. The time covered by a certain acquisition was equal to the ratio of the data length to the PRF and acquisition time was then further subdivided into time points to generate the sonogram. This meant that, to generate a sonogram, the system required that the velocities were low enough to not be aliased by a low PRF and that the temporal resolution of the sonogram was low enough that coherent Doppler spectra could still be generated. These limitations proved insurmountable in the current research mode architecture of the Aixplorer and would require a significant hardware and/or software update to the system to remedy.

Commented [AM38]: Fixed typo

The purpose of Chapter 6 was to test the performance of the MFUDSA algorithm in comparison to a number of other techniques which can be utilised for WSS estimation. The primary conclusion of this chapter was that the MFUDSA algorithm had the strongest performance out of the techniques tested in steady flow, with the highest sensitivity out of each technique tested and the greatest significance in delineation between disease levels. The algorithm could not be applied to pulsatile flow, but the results indicated that the transition to pulsatile flow does not appear to affect the sensitivity of techniques significantly and only lowers their specificity. By comparing the PW Doppler and *UltraFast* techniques between the two flow regimes, a partial comparison between PW Doppler and the MFUDSA technique can be established. The PW Doppler and the *UltraFast* techniques had similar performances in steady flow but the performance of the *UltraFast* technique in pulsatile flow was greater in terms of both sensitivity and specificity. When taken into account with the result that the MFUDSA technique had the highest sensitivity in steady flow, this indicates that it likely would have also had the greatest performance in pulsatile flow. It was also concluded that the sensitivity of the MFUDSA algorithm in steady flow put it as being broadly equivalent with PW Doppler and DSA in the diagnosis of arterial stenoses the formation of which typically takes place much later in the development of CVD than vessel wall stiffening. This indicates, therefore, that should the MFUDSA algorithm be applied in pulsatile flow it would provide an equivalent standard of diagnostic power while also being applicable much earlier in the progression of CVD.

Commented [AM39]: Rephrased

7.2. Future work

The phantoms used in this work represented a novel approach in the mimicking of the progression of arterial disease as they accurately exhibited the stiffness values seen *in*

vivo to an unprecedented degree of certainty. However, a limitation of this work was that the phantoms were only produced for use with ultrasound. With minor alterations to the phantom production protocol, the phantoms could be produced to enable a multi-modality analysis approach. This could be achieved by replacing the deionised water with a 10% solution of manganese chloride in deionised water. Manganese is a widely used contrast agent in MRI imaging [129] and the use of manganese chloride will increase the MR response of the phantom. The phantom production could further be adapted for use in CT imaging by varying the phantom attenuation coefficient to be in line with the appropriate Hounsfield units for human tissue. The Hounsfield units of the formulation of the tissue and vessel mimicking materials in the current study were not measured and therefore it is unknown how much modification would be required. This would be particularly important for the vessel mimic as if the density of the material is varied significantly, for example, with the goal of changing the Hounsfield units, the Young's modulus of the material will also change, potentially limiting its ability to model stages in the progression of CVD.

The current study did not feature the use of microbubble contrast agents; however, calibration experiments were carried out for the use of contrast agents in further experiments. The first set of experiments investigated the pulse pressures exerted by the Aixplorer under a variety of transmission parameters. It was found that the largest pulse pressure exerted by the system was 806.59 kPa. De Jong et al. [74] established, in the case of the SonoVue contrast agents, the pulse pressure should not exceed 150 kPa to avoid the alteration of bubble characteristics and pressures above 300 kPa would lead to bubble destruction. With these results in mind, further experiments utilising microbubble contrast agents would have been carried out with an acoustic power setting of -8 dB in order to ensure the behavio+ur of the contrast agents was not altered. Further, the use of

Commented [AM40]: Fixed typo

contrast agents may cause saturation of the Doppler spectrum, as discussed previously, the Doppler dynamic range of the system was measured to be approximately 17 dB. This means that relatively small concentrations of contrast agents may lead to complete saturation of the spectrum with some contrast agent techniques providing up to 16 dB more contrast than standard imaging [130].

A significant limitation of this work was the inability to utilise the MFUDSA algorithm in pulsatile mode. As discussed previously, the product of the PRF, the Fourier data length, and the number of time points in the sonogram cannot exceed the total data point length of the acquisition. This means that even for low velocities, a coherent sonogram could not be produced without aliasing of the spectrum and vice versa. When the sonogram was generated for the simulated Doppler data, the coherent sonogram could be produced for data point lengths as low as 10,000 data points. This value is still 5 times greater than the maximum length possible in an acquisition from the Aixplorer research package. Two methods could be utilised to circumvent this problem. The first proposed solution is that triggering could be used to enable multiple acquisitions to begin at different points in the cardiac cycle and these acquisitions could be stitched together using post-processing. This is possible because the memory buffer on the Aixplorer research package only works to limit the file size of individual acquisitions and not the total size of an experimental data set. For example, if a user desired an acquisition of 5 seconds of a pulsatile flow, with a PRF of 4 kHz, and the maximum data length of 2000 was used for each acquisition, the total time of each acquisition would be 0.5 seconds meaning 10 total acquisitions would be required, and each acquisition would need to have a time delay of 0.5 seconds applied to its trigger. However, this would not provide coherent sonograms as there would not be enough data in each acquisition to form a coherent sonogram. This could be rectified by increasing the PRF, thus requiring more acquisitions and an

increasingly large exported file, especially considering that the resulting file would only lead to a single acquisition. The problems with this solution are further compounded by the fact that the distribution package of the research package used in the current study did not support input trigger signals for the *UltraFast* acquisition mode.

The second proposed solution to this problem would be to directly implement the MFUDSA algorithm to the scanner and do the processing in real time. This would reduce the file size dramatically as a region of interest could be set, such as with colour flow imaging, which would discard excess data from other parts of the field of view. While the file sizes would still be quite large, the processing speed could be improved dramatically and there would be less risk of the data buffer filling completely. This method would require the direct modification of the on-board processing of the Aixplorer which is currently inaccessible to the average researcher. This solution, therefore, is only suitable as a commercial development or on a similar scanner with *UltraFast* equivalent functionality yet to be released.

The final limitation of this work was that the WSS values analysed were only viewed as a 2-dimensional slice of the vessel. A more complete analysis of the WSS would require a 3D time varying mapping of the velocity flow profile. This is important as interest in WSS has recently begun to move towards analysing not just the linear flow based WSS but also WSS arising from the vorticity of the flow [131].

Appendix: Code excerpts

Simulated Doppler data code

In Section 5.2.2, the methodology described the simulation of Doppler data for testing of the MFUDSA algorithm. This code is included here. The script was designed so that

it could generate steady and pulsatile flow data and would output a matrix of IQ data which could be read by the MFUDSA algorithm. This was achieved as follows:

```
L = 21000;                          % Length of signal (datapoints)
f = 700.*M;                         % Doppler shift in Hz
W = 6.2832*f;                       % Doppler shift in radians (2*pi*f)
Amp = 0.5;                          % Normalised amplitude
Fs = 7000;

S1 = Amp*cos(W) + 1i*Amp*sin(W);
```

In this code f, the frequency in Hz, was specified as an integer (determined through the Doppler equation) multiplied by some vector. The integer represented the maximum Doppler frequency shift to be simulated and the vector, M, could be set to steady flow (equal to 1) or pulsatile mode (varying between -1 and 1). The simulated signal was then sampled according to the sampling frequency which was equivalent to the PRF in Hz. The resulting data would contain only a single Doppler shift frequency (which could vary in time) which is not suitable for Multifrequency analysis. In order to introduce the extra data associated with a bandwidth of frequencies two for loops were constructed which would calculate the appropriate Doppler shift frequency for a range of frequencies in the pulse bandwidth and then superimpose the signals onto one another. These data were generated as follows:

```
L = 21000;                          % Length of signal (datapoints)
freqs = zeros(L,1);
S = zeros(L,1);                     % Pre-allocate memory


BW = linspace(2.9e3,7.1e3,L);       % 4HC bandwidth for 5MHz was 2.1 MHz
Amp_left =linspace(0,1,L/2);
Amp_right = fliplr(Amp_left);
Amp = [Amp_left, Amp_right];        % Amplitude varying linearly across bandwidth

velocity = 0.2;                     % m/s
c0 = 1540;                          % m/s
thetaDeg = 60;                      % Insonation Angle
theta = thetaDeg*pi/180;            % Radians

for j = 1:L
      freqs(j,1) = (2*velocity*cos(theta)*BW(j))/c0;
end


for k = 1:L
      f = freqs(k,1).*M;             % Doppler shift in Hz
      W = 6.2832.*f;                 % Doppler shift in radians (2*pi*f)

      S = S + Amp(k)*cos(W(k)) + 1i*Amp(k)*sin(W(k));
end
```

Note that now S was generated as a superposition of L signals with Doppler frequencies corresponding to the whole bandwidth of transmitted frequencies. Despite its relatively short length, this code required a considerable amount of memory and time to run. As such, the resulting simulated signal was only generated for one velocity setting and saved to avoid running this code if possible. Similarly to the previous code, the vector M could be specified to set steady or pulsatile flow.

The code used to generate the segments is as follows:

```
Fs = 7000;                          % Sampling Frequency in Hz
Time = L/Fs;                        % Total time = data length / PRF
NSegment = Time/0.01;               % Number of segments = time / temporal
                                      resolution

LSegment = L/NSegment;

for k = 0:NSegment-1
    S2(1:LSegment,k+1) = S1(((k*LSegment)+1:(k+1)*LSegment));
end
```

Note that the temporal resolution of the sonogram can be specified in line 3 (in this case, it was set to 0.01 seconds).

MFUDSA Algorithm Outline

The first step was to import the IQ data from the Aixplorer (when using simulated data, this step was skipped and a manual importation method was used). The following code reads in a user specified address and opens the IQ data, which is currently a 1-dimensional variable which alternates between I and Q data. The next step in the code is to reshape this data. A matrix, I, is created with size Ni * Nj * Nt where Ni * Nj is the pixel resolution of the field of view and Nt is the number of insonations.

```
fid = fopen([pathname,'/',filename '.' dataextension]);
data = fread(fid,Ni * Nj * Nt * NbSamples ,TypeData);

    I = reshape(data(1:2:(Ni*Nj*Nt*2)),[Ni,Nj,Nt]);
    Q = reshape(data(2:2:(Ni*Nj*Nt*2)),[Ni,Nj,Nt]);
    IQ = I + sqrt(-1) * Q;
```

The next step was to segment the data into the appropriate form. This was done inside two nested for loops and reiterated across the width and length of the vessel which was specified by the user.

```
IQSeg = IQ(Ry1:Ry2,Rx,:);
```

Ry1 and Ry2 were axial co-ordinates which define the range gate. These values were controlled by a for loop and moved the range gate radially across the vessel. Rx is the longitudinal vessel position; this was controlled by a for loop and iterated to move the range gate longitudinally when all radial velocity values were recorded for the current position. For each radial and longitudinal combination, a matrix called IQSeg was produced which was windowed in the time domain using a Hamming window:

```
w = hamming(length(IQSeg), 'periodic');
w_IQSeg = w'.*IQSeg;
```

The windowed signal then underwent a 2D Fourier transform to convert the IQ data to the frequency space:

```
fun = fft2(w_IQSeg);
fun1 = fftshift(fun);

fun2 = fun1.^(Scaling_factor_matrix);
P1 = abs(fun2./Comp_env');

Periodogram = trapz(Bandwidth,P1,1);
```

The function fftshift here is used to centre the zero-frequency component. The resulting periodogram is scaled and normalised using the functions Scaling_factor_matrix and Comp_env which refer to the spectral scaling process and the complex envelope described in Equation 5.2. Finally, the spectrum is integrated using the trapezoidal integration function with the frequency bandwidth acting as the limits of integration.

The resulting periodogram can be displayed but usually it was not as it slowed down the processing of the full vessel. Instead the maximum value was selected and saved as the Doppler frequency shift at that position in the vessel. The shift was converted into a velocity using the Fourier space limits and the Doppler equation.

```
fshift = (-Nt/2:Nt/2-1)*(Fs/Nt);
Vel = (fshift.*c0)./(2*f0*10e6*cos(theta))*10e-2;
```

The first line of this code specifies the frequency axis of the periodogram using the number of data points and the sampling frequency (the PRF). The second line is the Doppler equation with the addition of a scaling factor to produce the velocity output in cm s^{-1}.

Bibliography

[1] Osmanski B-F, Bercoff J, Montaldo G, Loupas T, Fink M, Tanter M. Cancellation of Doppler intrinsic spectral broadening using ultrafast Doppler imaging. IEEE Trans Ultrason Ferroelectr Freq Control 2014;61:1396–408.

doi:10.1109/TUFFC.2014.3049.

[2] Ramnarine K V, Nassiri DK, Hoskins PR, Lubbers J. Validation of a New Blood-Mimicking Fluid for Use in Doppler Flow Test Objects. Ultrasound Med Biol 1998;24:451–9. doi:10.1016/S0301-5629(97)00277-9.

[3] Hoskins PR, Thrush A, Martin K, Whittingham TA. Diagnostic Ultrasound: Physics and Equipment. 1st ed. London: Greenwich Medical Media Ltd; 2003.

[4] Duck FA. Chapter 4 – Acoustic Properties of Tissue at Ultrasonic Frequencies. Phys. Prop. Tissues, 1990, p. 73–135. doi:10.1016/B978-0-12-222800-1.50008-5.

[5] Evans DH, McDicken WN. Doppler ultrasound: Physics, Instrumentation and Signal Processing (Second Edition). 2000.

[6] Torp H, Kristoffersen K. Velocity matched spectrum analysis: A new method for suppressing velocity ambiguity in pulsed-wave Doppler. Ultrasound Med Biol 1995;21:937–44. doi:10.1016/0301-5629(95)00039-T.

[7] Loupas T, Gill RW. Multifrequency Doppler : Improving the Quality of Spectral Estimation by Making Full Use of the Information Present in the Backscattered RF Echoes 1994;41:522–31.

[8] BMUS. Guidelines for the safe use of diagnostic ultrasound equipment. 2009.

[9] Blake JR, Meagher S, Fraser KH, Easson WJ, Hoskins PR. A Method to Estimate Wall Shear Rate with a Clinical Ultrasound Scanner. Ultrasound Med Biol 2008;34:760–74. doi:10.1016/j.ultrasmedbio.2007.11.003.

[10] Santulli G. Epidemiology of Cardiovascular Disease in the 21st Century: Updated Numbers and Updated Facts. J Cardiovasc Dis 2013;1:1–2.

[11] World Health Organisation. Cardiovascular diseases (CVDs) 2017. https://www.who.int/en/news-room/fact-sheets/detail/cardiovascular-diseases-(cvds) (accessed May 16, 2019).

[12] Palombo C, Kozakova M. Arterial stiffness, atherosclerosis and cardiovascular risk: Pathophysiologic mechanisms and emerging clinical indications. Vascul Pharmacol 2016;77:1–7. doi:10.1016/j.vph.2015.11.083.

[13] Katritsis D, Kaiktsis L, Chaniotis A, Pantos J, Efstathopoulos EP, Marmarelis V. Wall Shear Stress: Theoretical Considerations and Methods of Measurement. Prog Cardiovasc Dis 2007;49:307–29. doi:10.1016/j.pcad.2006.11.001.

[14] Jemal A, Ward E, Hao Y, Thun M. Trends in the Leading Causes of Death in the United States, 1970-2002. JAMA 2005;294:1255. doi:10.1001/jama.294.10.1255.

[15] Ganz P, Hsue PY. Endothelial dysfunction in coronary heart disease is more than a systemic process. Eur Heart J 2013;34:2025–7. doi:10.1093/eurheartj/eht199.

[16] Aboyans V, Ricco J-B, Bartelink M-LEL, Björck M, Brodmann M, Cohnert T, et al. 2017 ESC Guidelines on the Diagnosis and Treatment of Peripheral Arterial Diseases, in collaboration with the European Society for Vascular Surgery (ESVS). Eur J Vasc Endovasc Surg 2017;39:763–816. doi:10.1016/J.EJVS.2017.07.018.

[17] Herzig R, Burval S, Krupka B, Vlachova I, Urbanek K, Mares J. Comparison of ultrasonography, CT angiography, and digital subtraction angiography in severe carotid stenoses. Eur J Neurol 2004;11:774–81. doi:10.1111/j.1468-1331.2004.00878.x.

[18] Eklöf H, Ahlström H, Magnusson A, Andersson L-G, Andrén B, Hägg A, et al. A

prospective comparison of duplex ultrasonography, captopril renography, MRA, and CTA in assessing renal artery stenosis. Acta Radiol 2006;47:764–74. doi:10.1080/02841850600849092.

[19] King DM, Moran CM, Browne JE. Comparative review of imaging methods used for diagnosing renal artery stenosis. Ultrasound 2012;20:135–41. doi:10.1258/ult.2012.011037.

[20] Merten GJ, Burgess WP, Rittase RA, Kennedy TP. Prevention of Contrast-Induced Nephropathy With Sodium Bicarbonate. Crit Pathways Cardiol A J Evidence-Based Med 2004;3:138–43. doi:10.1097/01.hpc.0000137152.52554.76.

[21] O'Sullivan S, Healy DA, Moloney MC, Grace PA, Walsh SR. The Role of N--Acetylcysteine in the Prevention of Contrast-Induced Nephropathy in Patients Undergoing Peripheral Angiography. Angiology 2013;64:576–82. doi:10.1177/0003319712467223.

[22] Hartung MP, Grist TM, François CJ. Magnetic resonance angiography: current status and future directions. J Cardiovasc Magn Reson 2011;13:19. doi:10.1186/1532-429X-13-19.

[23] Chien S, Li S, Shyy JY-J. Effects of Mechanical Forces on Signal Transduction and Gene Expression in Endothelial Cells. Hypertension 1998;31.

[24] Gnasso A, Carallo C, Irace C, De Franceschi MS, Mattioli PL, Motti C, et al. Association between wall shear stress and flow-mediated vasodilation in healthy men. Atherosclerosis 2001;156:171–6. doi:10.1016/S0021-9150(00)00617-1.

[25] Gnasso A, Carallo C, Irace C, Spagnuolo V, De Novara G, Mattioli PL, et al. Association Between Intima-Media Thickness and Wall Shear Stress in Common

Carotid Arteries in Healthy Male Subjects. Circulation 1996;94:3257–62. doi:10.1161/01.CIR.94.12.3257.

[26] Gnasso A, Irace C, Carallo C, De Franceschi MS, Motti C, Mattioli PL, et al. In Vivo Association Between Low Wall Shear Stress and Plaque in Subjects With Asymmetrical Carotid Atherosclerosis. Stroke 1997;28:993–8. doi:10.1161/01.STR.28.5.993.

[27] Malek AM, Alper SL, Izumo S. Hemodynamic Shear Stress and Its Role in Atherosclerosis. JAMA 1999;282:2035–42. doi:10.1001/jama.282.21.2035.

[28] Caro CG, FitzGerald JM, Schroter RC. Atheroma and arterial wall shear - Observation, correlation and proposal of a shear dependent mass transfer mechanism for atherogenesis. Proc R Soc London Ser B Biol Sci 1971;177:109–33. doi:10.1098/rspb.1971.0019.

[29] Bharadvaj BK, Mabon RF, Giddens DP. Steady flow in a model of the human carotid bifurcation. Part I—Flow visualization. J Biomech 1982;15:349–62. doi:10.1016/0021-9290(82)90057-4.

[30] Zarins CK, Giddens DP, Bharadvaj BK, Sottiurai VS, Mabon RF, Glagov S. Carotid bifurcation atherosclerosis. Quantitative correlation of plaque localization with flow velocity profiles and wall shear stress. Circ Res 1983;53:502–14. doi:10.1161/01.RES.53.4.502.

[31] Motomiya M, Karino T. Flow patterns in the human carotid artery bifurcation. Stroke 1984;15:50–6. doi:10.1161/01.STR.15.1.50.

[32] Asakura T, Karino T. Flow patterns and spatial distribution of atherosclerotic lesions in human coronary arteries. Circ Res 1990;66:1045–66.

doi:10.1161/01.RES.66.4.1045.

[33] Chatzizisis YS, Coskun AU, Jonas M, Edelman ER, Feldman CL, Stone PH. Role of Endothelial Shear Stress in the Natural History of Coronary Atherosclerosis and Vascular Remodeling. J Am Coll Cardiol 2007;49.

[34] Wentzel JJ, Chatzizisis YS, Gijsen FJH, Giannoglou GD, Feldman CL, Stone PH. Endothelial shear stress in the evolution of coronary atherosclerotic plaque and vascular remodelling: current understanding and remaining questions. Cardiovasc Res 2012;96:234–43. doi:10.1093/cvr/cvs217.

[35] Shaaban a M, Duerinckx a J. Wall shear stress and early atherosclerosis: a review. AJR Am J Roentgenol 2000;174:1657–65. doi:10.2214/ajr.174.6.1741657.

[36] Osinnski J, Ku D, Mukundan S. Determination of wall shear stress in the aorta with the use of MR phase velocity mapping. J Magn 1995.

[37] Reneman R, Arts T, Hoeks A. Wall shear stress–an important determinant of endothelial cell function and structure–in the arterial system in vivo. J Vasc Res 2006.

[38] Potters W V., Van Ooij P, Marquering H, VanBavel E, Nederveen AJ. Volumetric arterial wall shear stress calculation based on cine phase contrast MRI. J Magn Reson Imaging 2015;41:505–16. doi:10.1002/jmri.24560.

[39] Peng S-L, Wang F-N, Yang T-C, Hsu J-C, Wu Y-C, Peng H-H. Phase-contrast magnetic resonance imaging for the evaluation of wall shear stress in the common carotid artery of a spontaneously hypertensive rat model at 7T: Location-specific change, regional distribution along the vascular circumference,

and reproduci. Magn Reson Imaging 2015;34:624–31. doi:10.1016/j.mri.2015.12.026.

[40] Hochareon P, Manning KB, Fontaine AA, Tarbell JM, Deutsch S. Wall Shear-Rate Estimation Within the 50cc Penn State Artificial Heart Using Particle Image Velocimetry. J Biomech Eng 2004;126:430. doi:10.1115/1.1784477.

[41] Natarajan S, Mokhtarzadeh-Dehghan M. A numerical and experimental study of periodic flow in a model of a corrugated vessel with application to stented arteries. Med Eng Phys 2000;22:555–66. doi:10.1016/S1350-4533(00)00072-2.

[42] Vennemann P, Kiger KT, Lindken R, Groenendijk BCW, Stekelenburg-De Vos S, Ten Hagen TLM, et al. In vivo micro particle image velocimetry measurements of blood - plasma in the embryonic avian heart. J Biomech 2006;39:1191–200. doi:10.1016/j.jbiomech.2005.03.015.

[43] Anastasiou AD, Spyrogianni AS, Koskinas KC, Giannoglou GD, Paras S V. Experimental investigation of the flow of a blood analogue fluid in a replica of a bifurcated small artery. Med Eng Phys 2012;34:211–8. doi:10.1016/j.medengphy.2011.07.012.

[44] WOMERSLEY JR. Method for the calculation of velocity, rate of flow and viscous drag in arteries when the pressure gradient is known. J Physiol 1955;127:553–63.

[45] Zhou X, Xia C, Khan F, Corner GA, Huang Z, Hoskins PR. Investigation of Ultrasound-Measured Flow Rate and Wall Shear Rate in Wrist Arteries Using Flow Phantoms. Ultrasound Med Biol 2016;42:815–23. doi:10.1016/j.ultrasmedbio.2015.10.016.

[46] Ford MD, Xie YJ, Wasserman BA, Steinman DA. Is flow in the common carotid artery fully developed? Physiol Meas 2008;29:1335–49. doi:10.1088/0967-3334/29/11/008.

[47] Mynard JP, Wasserman BA, Steinman DA. Errors in the estimation of wall shear stress by maximum Doppler velocity. Atherosclerosis 2013;227:259–66. doi:10.1016/J.ATHEROSCLEROSIS.2013.01.026.

[48] Bercoff J. Ultrafast Ultrasound Imaging. Ultrasound Imaging - Med. Appl., InTech; 2011. doi:10.5772/19729.

[49] Couture O, Bannouf S, Montaldo G, Aubry JF, Fink M, Tanter M. Ultrafast Imaging of Ultrasound Contrast Agents. Ultrasound Med Biol 2009;35:1908–16. doi:10.1016/j.ultrasmedbio.2009.05.020.

[50] Vaitkus PJ, Cobbold RSC, Johnston KW. A comparative study and assessment of doppler ultrasound spectral estimation techniques part II: Methods and results. Ultrasound Med Biol 1988;14:673–88. doi:10.1016/0301-5629(88)90024-5.

[51] Law YF, Johnston KW, Routh HF, Cobbold RSC. On the design and evaluation of a steady flow model for Doppler ultrasound studies. Ultrasound Med Biol 1989;15:505–16. doi:10.1016/0301-5629(89)90103-8.

[52] Culjat MO, Goldenberg D, Tewari P, Singh RS. A Review of Tissue Substitutes for Ultrasound Imaging. Ultrasound Med Biol 2010;36:861–73. doi:10.1016/j.ultrasmedbio.2010.02.012.

[53] Dabrowski W, Dunmore-Buyze J, Rankin RN, Holdsworth DW, Fenster A. A real vessel phantom for imaging experimentation. Med Phys 1997;24:687–93. doi:10.1118/1.597991.

[54] Dabrowski W, Dunmore-Buyze J, Cardinal HN, Fenster A. A real vessel phantom for flow imaging: 3-D Doppler ultrasound of steady flow. Ultrasound Med Biol 2001;27:135–41. doi:10.1016/S0301-5629(00)00277-5.

[55] Wilhjelm JE, Vogt K, Jespersen SK, Sillesen H. Influence of tissue preservation methods on arterial geometry and echogenicity. Ultrasound Med Biol 1997;23:1071–82. doi:10.1016/S0301-5629(97)00034-3.

[56] King DM, Moran CM, McNamara JD, Fagan AJ, Browne JE. Development of a Vessel-Mimicking Material for use in Anatomically Realistic Doppler Flow Phantoms. Ultrasound Med Biol 2011;37:813–26. doi:10.1016/j.ultrasmedbio.2011.02.012.

[57] Cournane S, Cannon L, Browne JE, Fagan AJ. Assessment of the accuracy of an ultrasound elastography liver scanning system using a PVA-cryogel phantom with optimal acoustic and mechanical properties. Phys Med Biol 2010;55:5965–83. doi:10.1088/0031-9155/55/19/022.

[58] Ramnarine K V., Garrard JW, Dexter K, Nduwayo S, Panerai RB, Robinson TG. Shear wave elastography assessment of carotid plaque stiffness: Invitro reproducibility study. Ultrasound Med Biol 2014;40:200–9. doi:10.1016/j.ultrasmedbio.2013.09.014.

[59] Widman E, Maksuti E, Larsson D, Urban MW, Bjällmark A, Larsson M. Shear wave elastography plaque characterization with mechanical testing validation: a phantom study. Phys Med Biol 2015;60:3151–74. doi:10.1088/0031-9155/60/8/3151.

[60] Chatelin S, Bernal M, Papadacci C, Gennisson JL, Tanter M, Pernot M. Anisotropic polyvinyl alcohol hydrogel phantom for shear wave elastography in

fibrous biological soft tissue. IEEE Int Ultrason Symp IUS 2014;59:1857–60. doi:10.1109/ULTSYM.2014.0461.

[61] McKee CT, Last JA, Russell P, Murphy CJ. Indentation versus tensile measurements of Young's modulus for soft biological tissues. Tissue Eng Part B Rev 2011;17:155–64. doi:10.1089/ten.TEB.2010.0520.

[62] Jacot JG, Dianis S, Schnall J, Wong JY. A simple microindentation technique for mapping the microscale compliance of soft hydrated materials and tissues. J Biomed Mater Res Part A 2006;79A:485–94. doi:10.1002/jbm.a.30812.

[63] Engler AJ, Richert L, Wong JY, Picart C, Discher DE. Surface probe measurements of the elasticity of sectioned tissue, thin gels and polyelectrolyte multilayer films: Correlations between substrate stiffness and cell adhesion. Surf Sci 2004;570:142–54. doi:10.1016/J.SUSC.2004.06.179.

[64] Lundkvist A, Lilleodden E, Siekhaus W, Kinney J, Pruitt L, Balooch M. Viscoelastic Properties of Healthy Human Artery Measured in Saline Solution by AFM-Based Indentation Technique. MRS Proc 1996;436:353. doi:10.1557/PROC-436-353.

[65] Rezvani-Sharif A, Tafazzoli-Shadpour M, Avolio A. Progressive changes of elastic moduli of arterial wall and atherosclerotic plaque components during plaque development in human coronary arteries. Med Biol Eng Comput 2019;57:731–40. doi:10.1007/s11517-018-1910-4.

[66] Poree J, Chayer B, Soulez G, Ohayon J, Cloutier G. Noninvasive Vascular Modulography Method for Imaging the Local Elasticity of Atherosclerotic Plaques: Simulation and In Vitro Vessel Phantom Study. IEEE Trans Ultrason Ferroelectr Freq Control 2017;64:1805–17. doi:10.1109/TUFFC.2017.2757763.

[67] Boesen ME, Singh D, Menon BK, Frayne R. A systematic literature review of the effect of carotid atherosclerosis on local vessel stiffness and elasticity. Atherosclerosis 2015. doi:10.1016/j.atherosclerosis.2015.09.008.

[68] Dymling SO, Persson HW, Hertz TG, Lindström K. A new ultrasonic method for fluid property measurements. Ultrasound Med Biol 1991;17:497–500. doi:10.1016/0301-5629(91)90186-Z.

[69] Ophir J, Céspedes I, Ponnekanti H, Yazdi Y, Li X. Elastography: A quantitative method for imaging the elasticity of biological tissues. Ultrason Imaging 1991;13:111–34. doi:10.1016/0161-7346(91)90079-W.

[70] Nightingale K, Soo MS, Nightingale R, Trahey G. Acoustic radiation force impulse imaging: in vivo demonstration of clinical feasibility. Ultrasound Med Biol 2002;28:227–35. doi:10.1016/S0301-5629(01)00499-9.

[71] Haar G Ter. The new British Medical Ultrasound Society Guidelines for the safe use of diagnostic ultrasound equipment 2010. doi:10.1258/ult.2010.100007.

[72] Barnett SB. Routine ultrasound scanning in first trimester: What are the risks? Semin Ultrasound, CT MRI 2002;23:387–91. doi:10.1016/S0887-2171(02)90009-0.

[73] Apfel RE, Holland CK. Gauging the likelihood of cavitation from short-pulse, low-duty cycle diagnostic ultrasound. Ultrasound Med Biol 1991;17:179–85. doi:10.1016/0301-5629(91)90125-G.

[74] de Jong N, Emmer M, van Wamel A, Versluis M. Ultrasonic characterization of ultrasound contrast agents. Med Biol Eng Comput 2009;47:861–73. doi:10.1007/s11517-009-0497-1.

[75] Goertz DE, Yu JL, Kerbel RS, Burns PN, Foster FS. High-Frequency Doppler Ultrasound Monitors the Effects of Antivascular Therapy on Tumor Blood Flow 1. Cancer Res 2002;62:6371–5.

[76] Angelsen B. Ultrasound imaging: waves, signals, and signal processing. 2. Propagation and scattering in heterogeneous, nonlinear tissue with contrast agent imaging 2000.

[77] Meunier J, Bertrand M. Ultrasonic texture motion analysis: theory and simulation. IEEE Trans Med Imaging 1995;14:293–300. doi:10.1109/42.387711.

[78] Bercoff J, Tanter M, Fink M. Supersonic shear imaging: a new technique for soft tissue elasticity mapping. IEEE Trans Ultrason Ferroelectr Freq Control 2004;51:396–409. doi:10.1109/TUFFC.2004.1295425.

[79] Bercoff J, Montaldo G, Loupas T, Savery D, Mézière F, Fink M. Ultrafast Compound Doppler Imaging: Providing Full Blood Flow Characterization. IEEE Trans Ultrason Ferroelectr Freq Control 2011;58:134–47.

[80] Newhouse VL, Varner LW, Bendick PJ. Communications: Geometrical Spectrum Broadening in Ultrasonic Doppler Systems. IEEE Trans Biomed Eng 1977;BME-24:478–80. doi:10.1109/TBME.1977.326194.

[81] Newhouse VL, Bendick PJ, Varner LW. Analysis of Transit Time Effects on Doppler Flow Measurement. IEEE Trans Biomed Eng 1976;BME-23:381–7. doi:10.1109/TBME.1976.324648.

[82] Newhouse VL, Furgason ES, Johnson GF, Wolf DA. The Dependence of Ultrasound Doppler Bandwidth on Beam Geometry. IEEE Trans Sonics Ultrason 1980;27:50–9. doi:10.1109/T-SU.1980.31147.

[83] Winkler AJ, Wu J. Correction of intrinsic spectral broadening errors in doppler peak velocity measurements made with phased sector and linear array transducers. Ultrasound Med Biol 1995;21:1029–35. doi:10.1016/0301-5629(95)00047-U.

[84] Guidi G, Licciardello C, Falteri S. Intrinsic spectral broadening (ISB) in ultrasound Doppler as a combination of transit time and local geometrical broadening. Ultrasound Med Biol 2000;26:853–62. doi:10.1016/S0301-5629(00)00218-0.

[85] Hoskins PR. Accuracy of maximum velocity estimates made using Doppler ultrasound systems. Br J Radiol 1996;69:172–7. doi:10.1259/0007-1285-69-818-172.

[86] Hoskins PR. Estimation of blood velocity, volumetric flow and wall shear rate using Doppler ultrasound. Ultrasound 2011;19:120–9. doi:10.1258/ult.2011.011015.

[87] Browne JE. A review of Doppler ultrasound quality assurance protocols and test devices. Phys Medica 2014;30:742–51.

[88] Hurrell A. Voltage to pressure conversion: are you getting `phased' by the problem? J Phys Conf Ser 2004;1:57–62. doi:10.1088/1742-6596/1/1/014.

[89] Ivory A. Development of an optimised subharmonic dynamic contrast-enhanced ultrasound imaging technique for liver cancer 2018.

[90] Cowling MG, Price JF. Bandwidth Versus Time Concentration: The Heisenberg–Pauli–Weyl Inequality. SIAM J Math Anal 1984;15:151–65. doi:10.1137/0515012.

[91] Hoskins PR, Li SF, McDicken WN. Velocity estimation using duplex scanners. Ultrasound Med Biol 1991;17:195–9. doi:10.1016/0301-5629(91)90127-I.

[92] Daigle R, Stavros A, Lee R. Overestimation of velocity and frequency values by multielement linear array Dopplers. J Vasc Technol 1990;14:13.

[93] Thrush AJ, Evans DH. Intrinsic spectral broadening: a potential cause of misdiagnosis of carotid artery disease. J Vasc Invest 1995;1:187–92.

[94] Walker A, Olsson E, Wranne B, Ringqvist I, Ask P. Accuracy of spectral Doppler flow and tissue velocity measurements in ultrasound systems. Ultrasound Med Biol 2004;30:127–32. doi:10.1016/J.ULTRASMEDBIO.2003.08.020.

[95] Steinman AH, Tavakkoli J, Myers JG, Cobbold RS., Johnston KW. Sources of error in maximum velocity estimation using linear phased-array Doppler systems with steady flow. Ultrasound Med Biol 2001;27:655–64. doi:10.1016/S0301-5629(01)00352-0.

[96] Hoskins PR, Fish PJ, Pye SD, Anderson T. Finite beam-width ray model for geometric spectral broadening. Ultrasound Med Biol 1999;25:391–404. doi:10.1016/S0301-5629(98)00180-X.

[97] Browne JE, King D, Fagan AJ, Chari D, Moran CM. An investigation of the detection capability of pulsed wave duplex Doppler of low grade stenosis using ultrasound contrast agent microbubbles – An in-vitro study. Ultrasonics 2019;96:48–54. doi:10.1016/j.ultras.2019.04.003.

[98] Chu KC, Rutt BK. Polyvinyl alcohol cryogel: An ideal phantom material for MR studies of arterial flow and elasticity. Magn Reson Med 1997;37:314–9.

doi:10.1002/mrm.1910370230.

[99] Brusseau E, Fromageau J, Finet G, Delachartre P, Vray D. Axial strain imaging of intravascular data: results on polyvinyl alcohol cryogel phantoms and carotid artery. Ultrasound Med Biol 2001;27:1631–42. doi:10.1016/S0301-5629(01)00451-3.

[100] Surry KJM, Austin HJB, Fenster A, Peters TM. Poly(vinyl alcohol) cryogel phantoms for use in ultrasound and MR imaging. Phys Med Biol 2004;49:5529–46. doi:10.1088/0031-9155/49/24/009.

[101] Pazos V, Mongrain R, Tardif JC. Polyvinyl alcohol cryogel: Optimizing the parameters of cryogenic treatment using hyperelastic models. J Mech Behav Biomed Mater 2009;2:542–9. doi:10.1016/J.JMBBM.2009.01.003.

[102] Baker MI, Walsh SP, Schwartz Z, Boyan BD. A review of polyvinyl alcohol and its uses in cartilage and orthopedic applications. J Biomed Mater Res Part B Appl Biomater 2012;100B:1451–7. doi:10.1002/jbm.b.32694.

[103] Duboeuf F, Liebgott H, Basarab A, Brusseau E, Delachartre P, Vray D. Static mechanical assessment of elastic Young's modulus of tissue mimicking materials used for medical imaging. 2007 29th Annu. Int. Conf. IEEE Eng. Med. Biol. Soc., IEEE; 2007, p. 3450–3. doi:10.1109/IEMBS.2007.4353073.

[104] International Organization for Standardisation. ISO 7743:2011 Rubber, vulcanized or thermoplastic -- Determination of compression stress-strain properties. 2011.

[105] International Organization for Standardisation. ISO 37:2017 Rubber , vulcanized or thermoplastic — Determination of tensile stress-strain properties 2017.

[106] Teirlinck CJPM, Bezemer RA, Kollmann C, Lubbers J, Hoskins PR, Fish P, et al. Development of an example flow test object and comparison of five of these test objects, constructed in various laboratories. Ultrasonics 1998;36:653–60. doi:10.1016/S0041-624X(97)00150-9.

[107] International Electrotechnical Commission. Ultrasonics – Flow measurement systems – Flow test object 2001.

[108] King D. Development of Renal Phantoms for the Evaluation of Current and Emerging Ultrasound Technology. Dublin Institute of Technology, 2009. doi:10.21427/D7VP4C.

[109] King DM, Ring M, Moran CM, Browne JE. Development of a range of anatomically realistic renal artery flow phantoms. Ultrasound Med Biol 2010;36:1135–44. doi:10.1016/j.ultrasmedbio.2010.04.017.

[110] Ostrowski ST, Tothill P. Kidney depth measurements using a double isotope technique. Br J Radiol 1975;48:291–4. doi:10.1259/0007-1285-48-568-291.

[111] Qian M, Niu L, Wong KKL, Abbott D, Zhou Q, Zheng H. Pulsatile Flow Characterization in a Vessel Phantom With Elastic Wall Using Ultrasonic Particle Image Velocimetry Technique: The Impact of Vessel Stiffness on Flow Dynamics. IEEE Trans Biomed Eng 2014;61:2444–50. doi:10.1109/TBME.2014.2320443.

[112] Saijo Y, Filho E, Sasaki H, Yambe T, Tanaka M, Hozumi N, et al. Ultrasonic Tissue Characterization of Atherosclerosis by a Speed-of-Sound Microscanning System. IEEE Trans Ultrason Ferroelectr Freq Control 2007;54:1571–7. doi:10.1109/TUFFC.2007.427.

[113] Kawasaki T, Sasayama S, Yagi S-I, Asakawa T, Hirai T. Non-invasive assessment of the age related changes in stiffness of major branches of the human arteries. Cardiovasc Res 1987;21:678–87. doi:10.1093/cvr/21.9.678.

[114] Hoskins PR, Loupas T, McDicken WN. A comparison of three different filters for speckle reduction of doppler spectra. Ultrasound Med Biol 1990;16:375–89. doi:10.1016/0301-5629(90)90067-M.

[115] Wilson LS. Description of Broad-Band Pulsed Doppler Ultrasound Processing Using the Two-Dimensional Fourier Transform. Ultrason Imaging 1991;13:301–15. doi:10.1177/016173469101300401.

[116] Loupas T, Peterson RB, Gill RW. Experimental Evaluation of Velocity and Power Estimation for Ultrasound Blood Flow Imaging , by Means of a Two-Dimensional Autocorrelation Approach 1995;42:689–99.

[117] Loupas T, Powers JT, Gill RW. An Axial Velocity Estimator for Ultrasound Blood Flow Imaging , Based on a Full Evaluation of the Doppler Equation by Means of a Two-Dimensional Autocorrelation Approach 1995;42.

[118] Wells PNT. Instrumentation including color flow mapping. Clin. Appl. Doppler ultrasound, 1987, p. 26–45.

[119] Malone A, Chari D, Cournane S, Naydenova I, Fagan AJ, Browne JE. Investigation of the assessment of low degree renal artery stenosis based on velocity flow profile analysis using Doppler ultrasound: An in-vitro study). Phys Medica 2019;65:209–18.

[120] Finol EA, Amon CH. Blood Flow in Abdominal Aortic Aneurysms: Pulsatile Flow Hemodynamics. J Biomech Eng 2001;123:474–84. doi:10.1115/1.1395573.

[121] Swillens A, Lovstakken L, Kips J, Torp H, Segers P. Ultrasound simulation of complex flow velocity fields based on computational fluid dynamics. IEEE Trans Ultrason Ferroelectr Freq Control 2009;56:546–56. doi:10.1109/TUFFC.2009.1071.

[122] Jensen JA. Simulation of advanced ultrasound systems using Field II. 2004 2nd IEEE Int. Symp. Biomed. Imaging Macro to Nano (IEEE Cat No. 04EX821), vol. 2, IEEE; 2004, p. 636–9. doi:10.1109/ISBI.2004.1398618.

[123] Steinman DA, Poepping TL, Tambasco M, Rankin RN, Holdsworth DW. Flow Patterns at the Stenosed Carotid Bifurcation: Effect of Concentric versus Eccentric Stenosis. Ann Biomed Eng 2000;28:415–23. doi:10.1114/1.279.

[124] Pan X, Gao J, Tao S, Liu K, Bai J, Luo J. A two-step optical flow method for strain estimation in elastography: Simulation and phantom study. Ultrasonics 2014;54:990–6. doi:10.1016/J.ULTRAS.2013.11.010.

[125] Beattie D, Golledge J, Greenhalgh R, Davies A. Duplex imaging and renal artery stenosis. J Vasc Investig 1997;3:52–60.

[126] Soares GM, Murphy TP, Singha MS, Parada A, Jaff M. Renal Artery Duplex Ultrasonography as a Screening and Surveillance Tool to Detect Renal Artery Stenosis. J Ultrasound Med 2006;25:293–8. doi:10.7863/jum.2006.25.3.293.

[127] Williams GJ, Macaskill P, Chan SF, Karplus TE, Yung W, Hodson EM, et al. Comparative Accuracy of Renal Duplex Sonographic Parameters in the Diagnosis of Renal Artery Stenosis: Paired and Unpaired Analysis. Am J Roentgenol 2007;188:798–811. doi:10.2214/AJR.06.0355.

[128] Browne JE, Watson AJ, Hoskins PR, Elliott AT. Validation of a sensitivity

performance index test protocol and evaluation of colour Doppler sensitivity for a range of ultrasound scanners. Ultrasound Med Biol 2004;30:1475–83. doi:10.1016/j.ultrasmedbio.2004.09.005.

[129] Malheiros JM, Paiva FF, Longo BM, Hamani C, Covolan L. Manganese-Enhanced MRI: Biological Applications in Neuroscience. Front Neurol 2015;6:161. doi:10.3389/fneur.2015.00161.

[130] Simpson DH, Chien Ting Chin, Burns PN. Pulse inversion Doppler: a new method for detecting nonlinear echoes from microbubble contrast agents. IEEE Trans Ultrason Ferroelectr Freq Control 1999;46:372–82. doi:10.1109/58.753026.

[131] Itatani K, Okada T, Uejima T, Tanaka T, Ono M, Miyaji K, et al. Intraventricular Flow Velocity Vector Visualization Based on the Continuity Equation and Measurements of Vorticity and Wall Shear Stress. Jpn J Appl Phys 2013;52:07HF16. doi:10.7567/JJAP.52.07HF16.

List of Publications

Physica Medica 2019: *Investigation of the assessment of low degree (<50%) renal artery stenosis based on velocity flow profile analysis using Doppler ultrasound: An in-vitro study*

Physica Medica 2019: *Polyvinyl alcohol cryogel based vessel mimicking material for modelling the progression of atherosclerosis: a validation study for Doppler ultrasound* (under peer review)

List of Employability Skills and Discipline Specific Skills Training

Course code	Course title	ECTS credits awarded
GRSO 1001	Research Methods	5
ENEH 1010	Medical Imaging	5
GRSO 1010	Introduction to Pedagogy	5
LTTC 9134	Academic Writing and Publishing	10
GRSO 1002 (RPL)	Research Ethics	5
External module	CEUS course	5
External module	Signal processing with MATLAB	3
External module	Introduction to Python	2